Active Change of Permeable Material Properties for Low-Noise Trailing Edge Applications

J.H. Mayer

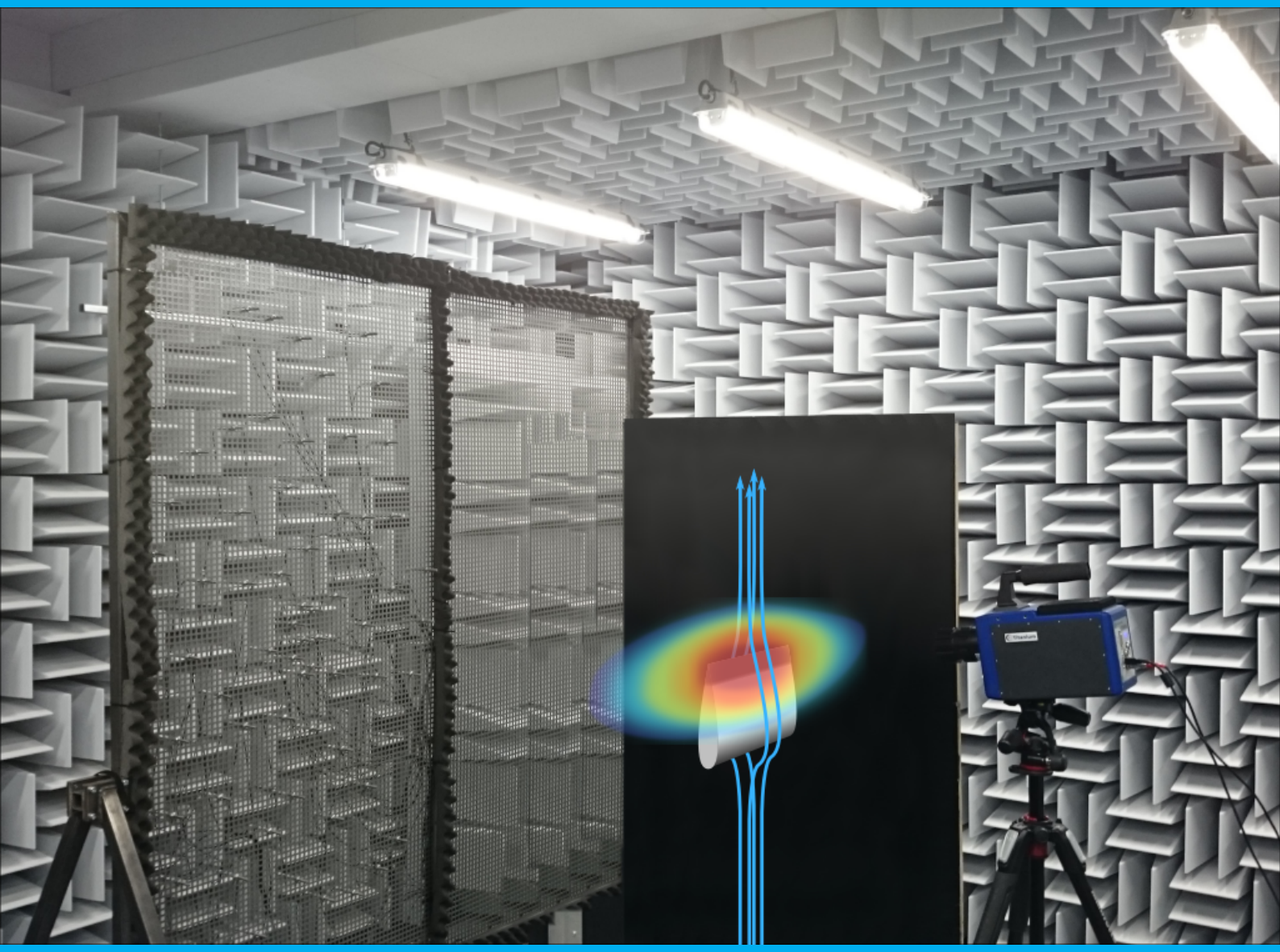

TU Delft

M.Sc. Thesis

Active Change of Permeable Material Properties for Low-Noise Trailing Edge Applications

by

J.H. Mayer

to obtain the degree of Master of Science in Aerospace Engineering
at the Delft University of Technology,
to be defended publicly on Friday February 22, 2019 at 11:00 AM.

Student number:	4621433	
Project duration:	May 1, 2018 – February 22, 2019	
Thesis committee:	Prof. dr. ir. S. van der Zwaag,	TU Delft, NovAM, Chair of committee
	Dr. D. Ragni,	TU Delft, Aeroacoustics, Responsible thesis supervisor
	Dr. M. Kotsonis,	TU Delft, Aerodynamics, External committee member
	A. Rubio Carpio, MSc,	TU Delft, Aeroacoustics, Supervisor

An electronic version of this thesis is available at `http://repository.tudelft.nl/`.

TU Delft

Preface

Aeroacoustics is a fascinating and truly multidisciplinary field of research which combines fundamentals of aerodynamics and acoustics. Introductory courses during my Master's program at TU Delft arouse my curiosity and led to the decision to pursue a research project in the aeroacoustics group. To add yet another degree of freedom, I opted for experimental work in the field of porous materials for airfoil self-noise reduction purposes. During the nine-month thesis project, I got the chance to explore new aspects of innovative permeable materials for noise mitigation purposes. Beside the unique research environment provided by TU Delft, the multidisciplinary project would not have been feasible without the support from several people from different research groups.

Special thanks go to the aeroacoustics group, specifically to the promoter and daily supervisor of this project, Daniele Ragni. Planning and conducting the experiments in the acoustic wind tunnel would not have been possible without your unbureaucratic way of approaching problems. I am grateful for the constructive cooperation with the NovAM group and the possibility to profit from their experience in the field of innovative materials. In particular, I want to thank Reza Hedayati for your practical help and advice in the field of porous materials. Furthermore, I would like to express my gratitude to Prof. Dr. Sybrand van der Zwaag for your willingness to chair the graduation committee.

I appreciated the opportunity to work closely together with PhD students from different research groups and with fellow students on the fifth floor. It was great working with you and I likewise enjoyed the time we spent off-campus. Thank you, Alejandro Rubio Carpio for your support concerning theoretical aspects of the project as well as your active help during the experimental campaigns. You were willing to help me out whenever possible, even if it meant carrying liquid nitrogen across the campus. For many insights into acoustic measurements and your help in making noise visible, I want to thank Salil Luesutthiviboon from the ANCE department.

The success of this work essentially depended on the various experimental setups in the chemical, physics and low-speed lab. I greatly appreciated the help and advice I got from Stefan Bernardy and Emiel Langedijk in the wind tunnel lab. Likewise, I want to thank Leon Roessen and Frans Oostrum for your support during the design phase and during testing in the structures and materials lab.

Last but not least, many thanks go to family and friends who supported me during the thesis project and throughout the entire Master's program. I truly value your visits here in Delft and I am excited to explore what the professional life has in store for me.

J.H. Mayer
Delft, January 2019

Summary

Mitigation of aerodynamically generated noise has become an important aspect of modern aircraft and wind turbine design. For many aerospace applications, the dominant airfoil self-noise source is turbulent boundary layer trailing edge (TBL-TE) noise. The replacement of solid airfoil trailing edges with permeable materials proved to be an adequate noise reduction mean in previous studies. While communication between the pressure and suction side is beneficial for aeroacoustics, it can negatively affect the aerodynamic performance of an airfoil. The objective of this work was to determine the feasibility of actively changing porous material properties on a pore-scale level. The proposed activation mechanism consisted of heating up a polymerically coated metallic foam.

From a literature study it was deduced that the method of activation potentially influences far-field noise levels due to changing fluid temperatures in the vicinity of the trailing edge and because of pore geometry changes. Furthermore, it was argued that interactions between wall pressure fluctuations and the soft coating are weak.

The effects of trailing edge heating on pressure communication across the porous material were analyzed experimentally. Characteristic material parameters, namely flow resistivity, permeability and form coefficient were measured for varying flow temperatures and it was shown that for low seepage velocities, the communication is negatively affected upon heating. Experimental data were in agreement with results from simple physical models of flow and material properties. A weak temperature dependence of *geometric* porous material parameters was observed and related to measurement uncertainties.

Temperature increase caused an expansion of the coating layer and led to decreasing pore diameters, as expected from theory. Microscopic images of the coated metallic foam with nominal pore diameters around 800 µm indicated relatively low changes of the pore size in the order of $< 20\,\mu m$. The coating material *Plasti Dip* was chosen due to its favorable physical properties such as a relatively long curing time. A thermomechanical analysis confirmed that the liquid rubber spray was suitable for temperature activation, even though both, positive and negative thermal expansion occurred in the temperature range of interest. Given typical thermal expansion coefficients of appropriate coating polymers, the main limitation of actively changing porous material properties on a pore-scale level was the restriction of the coating layer thickness.

Aeroacoustic measurements of radiated noise from a NACA0018 airfoil with various trailing edge inserts were conducted in the anechoic wind tunnel (A-Tunnel) of TU Delft. The feasibility of actively changing far-field noise characteristics was demonstrated based on the results from microphone array measurements. An assessment of the beamforming results showed that 1/3-octave band levels in the range between 630 Hz and 3.15 kHz accurately represented TBL-TE noise. Fluid temperature effects primarily contributed to the activation mechanism since similar changes of spectral noise levels were measured for coated and uncoated porous trailing edges. An average trailing edge surface temperature of 50 °C above ambient conditions caused a far-field noise increase of up to 2.5 dB at a flow speed of $15\,m\,s^{-1}$. The wall pressure spectrum remained unaltered upon trailing edge heating and local resistivity changes inside the porous material were identified as the main contribution to the activation mechanism.

From the experimental work it was concluded that the expansion of polymeric coating was not sufficient to alter the noise mitigation behavior of porous TEs. However, it was shown that temperature control of the porous material offers a possibility to actively influence flow resistivity without modifying the pore structure.

Contents

List of Figures

List of Tables

Nomenclature

List of Abbreviations

ANCE	Aircraft noise and climate effects
A-Tunnel	Anechoic wind tunnel
CAD	Computer-aided design
CSM	Cross spectral matrix
DMA	Dynamic mechanical analysis
DNS	Direct numerical simulation
EDM	Electrical discharge machining
FS	Full scale
IPER-MAN	Innovative permeable materials for airfoil noise reduction
IR	Infrared
NovAM	Novel aerospace materials
NTE	Negative thermal expansion
P800	Metal foam with nominal pore size of 800µm
P1200	Metal foam with nominal pore size of 1200µm
PBL	Pressure band level
PVDF	Polyvinylidene difluoride
RHS	Right-hand side
SNR	Signal-to-noise-ratio
SPI	Source power integration
TBL-TE noise	Turbulent boundary layer trailing edge noise
TE	Trailing edge
TMA	Thermomechanical analysis
WPS	Wall pressure spectrum

List of Symbols

A	Sample cross sectional area	m^2
A_j	Source autopower	$\mathrm{Pa}^2\,\mathrm{m}^2$
A_p	Pipe cross sectional area	m^2
b	Wing span	m
C	Form coefficient	m^{-1}
C_0	Reference form coefficient	m^{-1}
C_a	Linear curve fitting parameter	-
C_b	Quadratic curve fitting parameter	-
C_t	Shear wave propagation velocity	$\mathrm{m\,s}^{-1}$
c	Airfoil chord length	m
c_0	Speed of sound	$\mathrm{m\,s}^{-1}$
c_f	Friction coefficient	-
c_j	Panel length	m
D	Microphone array diameter	m
$d_{p,0}$	Nominal pore diameter of metal foam	m
$d_{p,a}$	Pore diameter of ambient coated foam	m
$d_{p,h}$	Pore diameter of heated coated foam	m
E	Elastic modulus	Pa
$E_{d,c}$	Energy dissipated in coating	J
$E_{d,v}$	Viscous dissipation	J

F_f	Form forces	N
F_{visc}	Viscous forces	N
f	Frequency	Hz
f_0	Resonance frequency	Hz
f_c	Center frequency	Hz
f_l	Lower frequency limit	Hz
f_u	Upper frequency limit	Hz
$\vec{g}$	Steering vector	-
h	Permeability distribution	-
I	Electric current	A
K	Flow permeability	m^2
K_0	Reference flow permeability	m^2
K'	Apparent permeability	m^2
k	Wavenumber	m^{-1}
L	Characteristic length	m
l	Distance between microphone array and scan plane	m
M	Mach number	-
M	Magnification factor	-
M_i	Measurement value	-
$M_{x,eff}$	Effective streamwise Mach number	-
$\dot{m}$	Mass flow rate	kgs^{-1}
N	Number of data points	-
N	Number of airfoil panels	-
n	Band number	-
n	Viscosity power law exponent	-
P_{exp},P_{sim}	Experimental/simulated integrated source power	W
P	Wavenumber frequency spectrum	$N^2\,s$
P_{diss}	Dissipated heating power	W
P_{el}	Electric power	W
p	Pressure	Pa
p_0	Reference pressure	Pa
p_∞	Ambient pressure	Pa
p_e	Effective sound pressure	Pa
p_{rms}	Root-mean-square of pressure fluctuations	Pa
p_s	Surface pressure	Pa
$\dot{Q}$	Volumetric flow rate	$m^3\,s^{-1}$
q	Dynamics pressure	Pa
R	Electric resistance	Ω
R	Flow resistivity	Ns/m^4
R_0	Reference flow resistivity	Ns/m^4
R^2	Coefficient of determination	-
R_{air}	Specific gas constant of air	$J\,kg^{-1}\,K^{-1}$
R_s	Specific electrical resistance	$\Omega\,m^{-1}$
R_T	Time scale ratio	-
Re	Reynolds number	-
r	Distance between sound source and observer	m
$\vec{r}_{j,n}$	Vector from scan grid point j to microphone n	Ns/m^4
S	Sutherland temperature	K
St	Chord based Strouhal number	-
SPL	Sound pressure level	dB
$SPL_{1/3}$	Sound pressure level of 1/3-octave band	dB
$SPL_{1/3,scaled}$	Scaled sound pressure level of 1/3-octave band	dB
t	Coating thickness	m
t	Porous material thickness	m
t	Time	s
T_g	Glass transition temperature	K

T_w	Wall temperature	K
T_0	Reference temperature	K
T_∞	Free stream temperature	K
U	Flow speed	$\mathrm{m\,s^{-1}}$
U_c	Convection velocity	$\mathrm{m\,s^{-1}}$
U_e	Boundary layer edge velocity	$\mathrm{m\,s^{-1}}$
u	Local streamwise velocity	$\mathrm{m\,s^{-1}}$
u	Measurement uncertainty	-
u_τ	Friction velocity	$\mathrm{m\,s^{-1}}$
V	Voltage	V
V	Volume	$\mathrm{m^3}$
V_0	Initial volume	$\mathrm{m^3}$
V_0	Propagation velocity of surface waves	$\mathrm{m\,s^{-1}}$
$V_{coat,a}$	Coating volume	$\mathrm{m^3}$
v_i	Induced velocity	$\mathrm{m\,s^{-1}}$
v_s	Seepage velocity	$\mathrm{m\,s^{-1}}$
x	Streamwise coordinate	m
y	Wall-normal coordinate	m
z	Spanwise coordinate	m
α	Angle of attack	deg
α_l, α_v	Linear/volumetric thermal expansion coefficient	$\mathrm{K^{-1}}$
Γ	Circulation	$\mathrm{m^2\,s^{-1}}$
γ	Circulation distribution	$\mathrm{m\,s^{-1}}$
γ	Ratio of specific heats	-
Δd_p	Pore size change	m
Δp	Pressure difference	Pa
ΔSPL	Sound pressure level difference	dB
ΔT	Temperature change	K
Δt	Signal time delay	s
Δt	Time step	s
ΔV	Volume change	$\mathrm{m^3}$
Δx	Smallest resolvable length scale	m
δ	Characteristic flow length	m
δ_0	Boundary layer thickness	m
δ^*	Displacement thickness	m
δ_t	Thermal boundary layer thickness	m
Θ	Momentum thickness	m
θ	Directivity angle	deg
κ	Permeability parameter	$\mathrm{m^3\,N^{-1}\,s^{-1}}$
λ	Mean free path	m
λ_0	Material resonance wavelength	m
μ	Dynamic viscosity	$\mathrm{N\,s\,m^{-2}}$
μ_0	Reference viscosity	$\mathrm{N\,s\,m^{-2}}$
μ_l	Loss tangent	-
ν	Kinematic viscosity	$\mathrm{m^2\,s^{-1}}$
ρ	Density	$\mathrm{kg\,m^{-3}}$
σ	Standard deviation	-
σ	Poisson's ratio	-
τ_w	Wall shear stress	Pa
Φ_{pp}	Pressure auto-spectral density	$\mathrm{Pa^2\,s}$
Φ^*	Pressure spectrum scaling factor	$\mathrm{Pa^2\,s}$
φ	Porosity	-
ω	Angular frequency	$\mathrm{s^{-1}}$
ω_0	Material resonance frequency	$\mathrm{s^{-1}}$
ω^*	Frequency scaling factor	$\mathrm{s^{-1}}$

1 Introduction

We are living in a noisy world. Every part of our daily life is accompanied by varieties of sounds - from the pleasant tones of music to annoying and harmful disturbances due to traffic. Physically speaking, sound is generated by introducing small pressure disturbances in an otherwise quiescent medium. The resulting motion of fluid particles spreads in form of longitudinal waves and can be received from an observer who is located a certain distance away from the source. The nature of source, wave propagation and receiver determines if the acoustic waves are perceived as pleasant or disturbing. In general, the term “noise” is used for unwanted sound and great efforts are undertaken in different fields of engineering in order to reduce noise to a minimum.

Sources of noise can be manifold. The concept of sound generation through vibrating structures - such as the membrane of a speaker - is familiar to us and therefore it is easy to grasp. Another mechanism is aerodynamically generated noise which originates from turbulent fluid motions. The intensity of this kind of noise strongly depends on the fluid speed. Therefore, it is reasonable that noise mitigation efforts mostly concentrate on high-speed applications. In the field of aerospace engineering, aerodynamically generated noise becomes an increasingly important consideration. With the introduction of more silent high-bypass turbofan engines, airframe noise, i.e. the noise generated from airflow over structures, is set into the focus of current research [1]. The landing approach is the flight phase in which airframe noise is most critical since landing gear and high-lift devices are deployed while engine power settings are low [2, 3]. The close proximity to urban, inhabited regions during the final approach underlines the importance of tackling airframe noise. Strict noise regulations can have an economic impact on airport and aircraft operators due to operational restrictions such as a ban on night flights. Additionally, airport operators face costs due to required noise protection measures for private buildings in zones of high noise pollution [4].

Another field where attention to aerodynamically generated noise is required is energy production through wind turbines. The noise emitted by wind turbine rotors is perceived as particularly annoying compared to similar levels of other noise sources [5]. Noise intensity scales with the rotational speed of the blades. Especially for onshore applications, strict regulations can limit the profit from wind turbines if the rotational speed has to be reduced in order to comply with noise regulations [6, 7].

The previous examples show the necessity of research efforts in the field of aerodynamically generated noise. The discipline which is concerned with this noise mechanism is referred to as *aeroacoustics* [8]. Research in this field can be inspired by nature, where highly advanced aeroacoustic designs exist. An example is the impressive capability of owls to fly almost silently [9]. More and more attention is paid to aeroacoustics due to the steady increase in air traffic and the rising number of large wind turbines. The main goal of aeroacoustic research is to ensure that aerodynamically generated noise does not pose operating limits to technical designs. At the same time, possible penalties resulting from noise mitigation measures should be reduced to a minimum. There is a certain irony in the fact that advances in aeroacoustic research will be indicated by the lack of public interest in this topic.

1.1. Airfoil Self-Noise

Aeroacoustic noise, generated by lifting surfaces, has been subject to increasing research efforts during the last years. Lifting devices are generally made of structures with large surface areas which are exposed to high

flow speeds and strong aerodynamic forces. The low-turbulence inflow is disturbed when a rigid surface is encountered and a turbulent boundary layer can develop close to the surface. Turbulent flow is characterized by unsteady fluid motion and different scales of eddies which are convected with the mean flow. It has to be stressed that the *aeroacoustic* noise, generated by turbulent flow, does not result from a vibrating surface. Instead, the fluctuating fluid motions are accompanied by pressure fluctuations which are partly scattered in form of acoustic waves. This noise generation mechanism holds true for turbulent flow in free air; however, the presence of rigid walls leads to much higher levels of radiated noise [11]. In the following, different airfoil self-noise generation mechanisms are outlined. Brooks et al. [10] characterized five different noise sources based on the assumption of low-turbulence inflow. Summaries of airfoil self-noise sources can also be found in [12, 13]. Here, only airfoil self-noise generated by lifting surfaces in undisturbed inflow, as illustrated in Figure 1.1, are addressed. The generation of noise from airfoils which encounter turbulent inflow is not discussed.

- **Laminar boundary layer instability noise**
  If the flow over the airfoil's surface stays laminar, downstream convected instabilities in form of Tollmien-Schlichting waves develop close to the surface. The resulting surface pressure fluctuations are scattered into far-field noise upon encountering the trailing edge (TE). A feedback loop between the scattered acoustic waves and the generation of upstream flow instabilities magnifies this mechanism. The resulting airfoil self-noise has a quasi-tonal spectrum.

- **Turbulent boundary layer trailing edge noise (TBL-TE noise)**
  Turbulent boundary layers are characterized by unsteady fluid motions and pressure fluctuations caused by turbulent structures with varying sizes and lifetimes. The pressure fluctuations close to the wall are convected downstream and the sudden jump in boundary conditions at the TE leads to scattering into far-field noise. Contrary to laminar boundary layer noise and as a result of the varying sizes of turbulent structures, the scattered TBL-TE noise spectrum is broadband.

- **Trailing edge bluntness noise**
  So far, lifting surfaces with sharp TEs were considered. Blunt TEs are present if the edge thickness is in the order of the boundary layer thickness or higher. In this case, the dominant self-noise source originates from vortex shedding at the thick TE. Periodic vortex shedding can result in tonal noise whose frequency depends on the TE thickness and boundary layer thickness.

- **Separation and stall noise**
  For high angles of attack, flow separation from the surface sets in and a large recirculation region of unsteady flow is formed above the airfoil. For further increasing angles of attack, complete stall occurs. The resulting broadband noise level exceeds other sources considerably. Fink and Bailey [14] measured broadband noise increase of up to 10 dB with respect to TBL-TE noise for separated flow conditions. Separation noise is especially important in wind turbine applications where thick airfoil sections close to the root are prone to flow separation [13].

- **Tip vortex noise**
  Due to the pressure difference on suction and pressure side of a finite, lift-generating wing, a tip vortex develops. The vortex core consists of viscous, turbulent flow. The convected pressure fluctuations past the wing tip are source of airfoil self-noise, similar to the mechanism of TBL-TE noise. In the case of unsteady tip vortices, the vortex shedding itself can generate aeroacoustic noise.

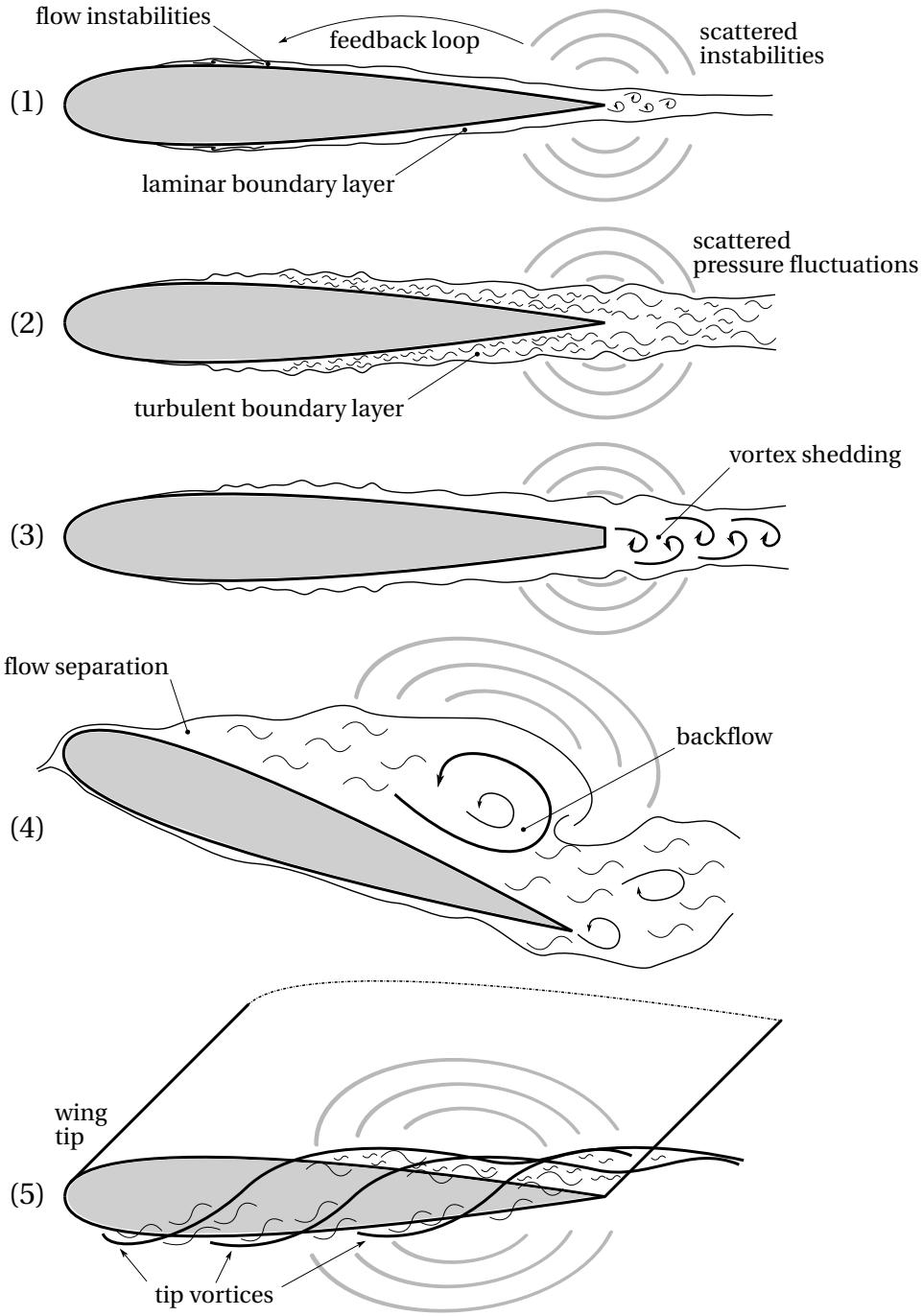

Figure 1.1: Illustration of airfoil self-noise generation mechanisms according to [10]. The following mechanisms are depicted: (1) Laminar boundary layer instability noise, (2) Turbulent boundary layer trailing edge noise, (3) Trailing edge bluntness noise, (4) Stall noise, (5) Tip vortex noise.

1.2. Turbulent Boundary Layer Trailing Edge Noise

The overview of different airfoil self-noise mechanisms shows that the task of designing quiet airfoils strongly depends on operating conditions and airfoil geometry. In the scope of this study, aerospace and wind energy applications are the main focus and hence, it is assumed that Reynolds numbers are sufficiently high for turbulent transition along the airfoil. The problem of separation and stall noise can be tackled by ensuring that the airfoil does not encounter angles of attack above a certain limit. Airfoil self-noise in the form of blunt TE noise and tip vortex noise directly results from the geometric design of the airfoil. The use of sharp TEs and a sharp wing tip are effective measures to mitigate these noise sources. This leaves TBL-TE noise the main mechanism and current research in the field of airfoil self-noise focuses on means of reducing this source. Experimental studies on noise source locations support the focus on TBL-TE noise mitigation research. Oerlemans et al. [15] concluded from acoustic field measurements that broadband TBL-TE noise is the dominant noise source of large wind turbines. Chow et al. [3] discussed the main airframe noise sources of an aircraft in landing configuration. Beside landing gear noise, the high lift devices were identified as major noise contributors. In particular, the TEs of slats and flaps, as well as their side edges, contributed to measured airframe noise.

Noise generated from turbulent flows has first been addressed by Lighthill [11, 16] in 1952. He derived a relation between radiated sound intensity and aeroacoustic noise sources, known as Lighthill analogy. While Lighthill's analysis was restricted to free turbulence (jet noise), Curle [17] derived a scaling law for noise generated from turbulent flow close to solid boundaries. The specific problem of turbulent flow past a solid edge was examined by Ffowcs Williams and Hall [18] in 1969. Based on Lighthill's acoustic analogy, they found that the edge noise intensity of a semi-infinite plate scales according to

$$p_e^2 \propto \rho U^3 M^2 \frac{\delta b}{r^2} \sin^2\left(\frac{\theta}{2}\right), \tag{1.1}$$

where p_e is the effective sound pressure, U is the inflow velocity, M is the free stream Mach number and δ is a characteristic flow length scale. Furthermore, TBL-TE noise levels scale with the wing span b and the observer distance r. The noise is not homogeneously radiated in all directions; however, the intensity is proportional to $\sin^2(\theta/2)$ where θ denotes the directivity angle with respect to the horizontal plane. Figure 1.2 depicts the directivity pattern and illustrates that the highest intensity is directed upstream of the TE. From Eq. 1.1 it follows that the noise levels scale with U^5. Regarding the Mach-number scaling, TBL-TE noise is a much more effective noise mechanism in the subsonic regime compared to jet-noise for which Lighthill [16] derived a M^5 Mach number dependency. An in-depth analysis of the physics behind TBL-TE noise generation is provided in Sec. 2.2.

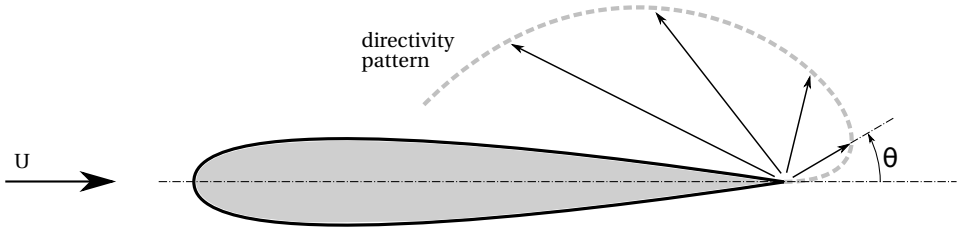

Figure 1.2: Directivity pattern of TBL-TE noise. The highest noise intensity occurs in upstream direction.

1.2.1. Recent Efforts in TBL-TE Noise Reduction

The demand for silent airfoil solutions explains the recent efforts in finding ways to mitigate TBL-TE noise. Based on the noise generation mechanism, two different research approaches can be identified.

First, the reduction of pressure fluctuations in the turbulent boundary layer leads to decreasing noise levels when scattered at the TE. The magnitude of wall pressure fluctuations scales with the free stream velocity and hence, the most obvious TBL-TE noise mitigation mean is the reduction of flow velocity. From the underlying scaling with the fifth power of flow velocity, it becomes obvious that decreasing flow speed has a large impact on noise intensity. However, for applications in the aerospace industry, certain speeds, such as a minimum landing speed, are required for safe operation. Reducing the tip speed of wind turbines results in noise reduction; however, it is accompanied by a loss in efficiency [6]. Therefore, noise mitigation through reduced air speed remains an operational issue. Careful design of the airfoil shape represents another method

to beneficially influence the turbulent boundary layer. Aeroacoustically optimized profiles have been found which do not compromise performance [19].

The second group of noise reduction techniques affects the scattering of convected surface pressure fluctuations at the TE. A variety of TE modifications has been investigated, ranging from modified edge geometries to flexible extensions. A systematic overview of different TE layouts is listed below.

- **Trailing edge serrations**
  The underlying idea of a non-straight TE is to modify the inclination of the sharp transition between airfoil surface and free air. It was shown that scattered noise is reduced if the convected pressure fluctuations perceive a non-straight TE [20]. Recently, a variety of non-straight TE geometries were investigated analytically [21]. Tested shapes included sawtooth, sinusoidal and slitted TEs as well as combinations of these geometries, such as slitted-sawtooth serrations. Arce León et al. [13] experimentally showed that a variation of the slitted-sawtooth geometry performed best in terms of far-field noise mitigation. They concluded that the dominant noise reduction mechanism for serrations is the mitigation of the surface discontinuity at the TE. The exact physical mechanism is still subject to research and current studies of the near-wall flow structures aim at closing the gap between analytical models and experiments [22].

- **Trailing edge brushes**
  The use of TE extensions in form of *soft* brushes proved to be an effective way for TBL-TE noise mitigation. Brushes were used in experiments by Herr and Dobrzynski [23] with the intention to reduce the effect of surface discontinuity at the TE. They concluded that the main mechanism of measured noise reduction is viscous damping of pressure fluctuations in the vicinity of the brushes. Both, TE serrations and brushes, are means to alleviate the jump between the rigid airfoil surface and free air. If the spacing of TE slits is reduced, a comb-type geometry results. The use of flexible combs allows for interactions between the material and the flow and is therefore similar to soft brushes. Herr [24] compared rigid and flexible combs experimentally and inferred that flexibility is beneficial; however, also rigid combs showed broadband noise mitigation.

- **Limp trailing edges**
  Instead of adding soft, structurally weak TE devices like brushes, fluid-structure interaction can also be achieved by means of elastic TEs. Howe [25] derived that for high fluid loadings (i.e. for underwater applications), flexible TEs can lead to TBL-TE noise reduction and directivity changes. Experiments with limp TE extensions in the form of thin rubber foils were carried out by Kamps et al. [26]. Broadband noise reduction was not observed; however, tonal noise mitigation was reported. In agreement with the results from Herr [24], it can be concluded that flexibility of TE devices does not play a key role in TBL-TE noise mitigation.

- **Porous trailing edges**
  From a theoretical consideration, the sudden change of boundary conditions at the TE should be avoided in order to reduce TBL-TE noise scattering. This concept of "variable impedance" TEs was first investigated experimentally and theoretically in the 1970s [27, 28]. A possible way to reduce the impedance discontinuity at the TE is the use of porous materials. These materials combine multiple characteristics of the above mentioned means of TBL-TE noise mitigation. Complicated and delicate geometrical changes of the TE, such as slitted-sawtooth serrations, can be avoided. Porous structures have positive effects on noise scattering while being structurally rigid.

1.2.2. Noise Reduction through Porous Trailing Edges

Recent numerical and experimental studies on porous TEs showed promising results in TBL-TE noise mitigation. Jaworski and Peake [29] analytically investigated the effects of poroelastic TE extensions. They concluded that the isolated effect of porosity leads to scattered noise scaling with the sixth power of velocity instead of the well-known fifth power scaling of rigid TEs. A similar analytical problem setup, based on a semi-infinite flat plate with porous extension, was studied by Kisil and Ayton [30]. Rossian et al. [31] carried out a numerical CAA study of an airfoil with different porous TEs. For homogeneous porous materials, they reported noise reduction in the order of 3.5 dB, while the use of non-uniform porous materials resulted in further noise mitigation.

A variety of experimental studies with the goal of TBL-TE noise mitigation through porous materials has been conducted in the last years. Herr et al. [32] reported a maximum noise reduction in the order of 2-6 dB.

From experiments with entirely porous airfoils, Geyer et al. [33] concluded that a maximum noise reduction of around 8 dB is achievable. At the same time, the rough airfoil surface was expected to contribute to high-frequency excess noise. Later, Geyer and Sarradj [34] compared the noise characteristics of different porous TE lengths. The fully porous airfoil showed maximum noise reduction of up to 10 dB and for decreasing porous extents, lower noise reduction and increasing aerodynamic performance was noted. Rubio Carpio et al. [35] measured far-field noise radiated from a NACA0018 airfoil with a porous TE extension of 20 % chord length. The maximum observed noise mitigation amounted to 11 dB with respect to the solid TE reference case.

TBL-TE noise mitigation by means of porous TEs can be regarded as a proven concept; however, the optimum porous geometry or the performance under changing flow conditions are still open research questions. While some studies on the effects of changing angles of attack exist [32, 36], no consistent explanation for their strong effects on noise mitigation has been provided, yet. Even for zero angle of attack, aerodynamic performance of an airfoil equipped with a porous TE decreases due to increased surface roughness and pressure balance between suction and pressure side. Recent investigations conclude that the choice of porous material and the length of the porous insert play a major role for aerodynamic performance. Interestingly, it was found that configurations with optimum noise reduction do not necessarily result in the worst aerodynamic performance and vice versa [32, 34]. For partly porous SD7003 airfoils operating at angles of attacks between $-12°$ and 24°, Geyer and Sarradj [37] performed balance measurements of lift and drag in addition to acoustic measurements. They identified the flow resistivity as characterizing parameter for aerodynamic performance and observed a shift of the drag polar with increasing length of the permeable surface towards higher drag and reduced lift. These results leave room for improving porous inserts with the goal to maximize noise mitigation while minimizing the aerodynamic penalty. Current research mainly focuses on porous geometries which promise best acoustic performance.

Several studies on TBL-TE noise mitigation through porous materials concluded that the most influential parameter is the air flow resistivity [32–34, 38]. In particular, it was found by Herr et al. [32] that using a porous TE with a sealed suction or pressure side completely cancels the noise reduction effect. The thin, non-permeable layer applied to one side of the TE did not influence the porosity of the TE; however, the permeability was reduced to zero. The effects of permeability on TE noise reduction were recently examined by Rubio Carpio et al. [35]. They experimentally investigated the noise mitigation effects of a porous TE equipped with a non-permeable membrane in the symmetry plane. While the permeable TE showed noise reduction up to 11 dB, the porous, impermeable version did not perform better than the solid reference case. Rubio Carpio et al. [35] concluded that pressure communication between the two sides of the TE is essential for noise mitigation.

The porosity of a permeable TE plays a role for additional roughness noise production. Increasing porosity demands larger pores and hence increases the surface roughness. A contribution of roughness noise in the high-frequency domain (>10 kHz) was observed by Geyer et al. [33] for flows over porous airfoils. Herr et al. [32] found that pore structures smaller than 160 µm do not result in additional surface roughness noise. Rubio Carpio et al. [35] observed the same excess noise characteristics for permeable and impermeable porous TEs. They observed surface roughness noise contribution for a chord-based Strouhal number above $St = 15$.

The optimum distribution of permeability and porosity along the porous TE is still subject to research. A promising optimization approach is the use of non-homogeneous, porous materials [30, 39, 40]. It is motivated by generating a smooth impedance transition between the solid airfoil and the discontinuity at the TE.

The outline of research topics in the field of porous TEs shows the necessity of focusing on the physical mechanisms that lead to TBL-TE noise reduction. In literature, the use of porous TEs is expected to have multiple effects on the convected pressure field and on pressure scattering.

- **Reduced impedance jump**
  Generating a smooth impedance transition is a major motivation for using porous TEs [25, 27, 28]. Above the porous material, pressure fluctuations are not blocked by a rigid surface but can penetrate the surface. The idea of variable impedance is to reduce the strong scattering of pressure waves at the TE of a solid airfoil where the boundary conditions suddenly change.

- **Acoustic absorption**
  Porous materials have been widely used for applications where absorption of acoustic waves is required [41]. Reflection of sound waves on a porous surface is reduced since the fluid motion, induced by sound waves, is damped within the pores. Some studies link the mechanism of acoustic absorption to TBL-

TE noise reduction [24, 42]. However, experiments with porous but non-permeable extensions did not show any broadband noise reduction [32, 35]. A large influence of the porous material on acoustic waves is therefore not likely.

- **Hydrodynamic absorption**
  Fluid motion through the pores, resulting from the turbulent flow field at the porous surface, is damped through enhanced viscous dissipation. Especially for brushed TE extensions, this is considered to influence TBL-TE noise reduction [23, 24, 42]. In a recent study, the hydrodynamic field at the TE, resulting from vortex shedding, was shown to be damped in the porous TE region [38].

- **Pressure mismatch balance**
  The communication of upper and lower side of the TE can balance the turbulent boundary layer pressure fluctuations on both sides [42]. Experiments with porous, non-permeable TEs indicate that the correspondence between the two sides is essential for noise reduction [32, 35]. The effect on TBL-TE noise results from a balance of the blocked surface pressure *fluctuations* rather than from static pressure differences at suction and pressure side of a lifting surface.

The list of possible noise mitigation influence factors indicates that up to now there is no consensus in terms of the underlying physical mechanisms. First steps towards understanding the basic phenomena observed so far were taken by examining the turbulence properties [35] and by measuring wall pressure statistics in close proximity to the porous surface [38]. From turbulent intensities in the boundary layer and changing wall pressure magnitude and coherence, a profound analysis of the dominant noise mitigation mechanism can be carried out.

1.2.3. Motivation for Activated Porous Trailing Edges

The use of porous TEs is a promising concept for TBL-TE noise reduction which has been proven in several studies. Noise mitigation critically depends on the properties of the porous material such as the pore size, permeability and surface roughness. In previous experiments, some of these parameters were varied systematically with the goal to find the optimum porous properties for noise reduction. The present research project is part of the "Innovative PERmeable Materials for Airfoil Noise reduction" (IPER-MAN) project. Instead of using a variety of different TE materials, the focus of this thesis project lies on actively changing the properties of the porous material. A smooth transition between different configurations potentially provides insight into the optimum geometry for noise mitigation.

Apart from research benefits, possible engineering applications could make use of actively controlled TE properties. For aerospace applications, the requirement for silent flight is only given for certain flight conditions, such as during the final landing approach. Furthermore, it is expected that the geometrical structure which offers best mitigation capabilities depends on fluid dynamics and hence is a function of the inflow velocity. Adapting the noise mitigation characteristics of a porous TE to the current flight phase would be an opportunity for optimum noise reduction without aerodynamic penalties. Similarly, for wind energy, the noise mitigation characteristics could actively be changed depending on inflow conditions or on the time of day. It is stressed that the focus of the present project lies on a proof of concept rather than on applicability for specific engineering tasks.

The proposed mechanism of activation consists of heating up a polymerically coated, porous TE. Thermal expansion of the coating material is expected to modify the geometry of the porous TE and thus affect its noise mitigation characteristics. The temperature of the TE can be controlled relatively easily without the necessity of installing moving parts inside the airfoil. From an engineering point of view, activation via temperature is appealing due to the occurrence of natural temperature gradients in the atmosphere. This could allow for tuning aircraft noise characteristics according to specific flight altitudes. In addition to geometrical effects, surface temperature changes might influence noise mitigation mechanisms of porous materials positively by affecting the flow structures and by influencing potential interactions with the coating material.

1.3. Research Goals and Research Questions

In the context of the main research goal, namely change of TBL-TE noise characteristics by means of activated porous materials, two research objectives are defined.

1 The first research objective is to experimentally demonstrate the feasibility of *actively* changing the noise mitigation characteristics of airfoils with porous TEs. In the first step, microscopy imaging will

be used to quantify the changes in pore size of the coated material upon heating. The combined impact of the two proposed influence factors, namely geometrical changes and temperature changes, will be evaluated by means of far-field noise measurements in the anechoic wind tunnel. A comparison between the far-field noise of non-activated (cold) and activated (warm) porous materials will be performed.

2 The second research objective is to determine the isolated effects of changing TE wall temperature on the far-field noise spectrum. Far-field noise measurements of heated, uncoated TEs will be performed in the anechoic wind tunnel. The achievable noise reduction for specific temperatures will be compared to the results from # 1 and it will be determined if geometrical changes or fluid heating are the dominant activation mechanisms. The capabilities of the heating setup in terms of achievable wall temperature and its distribution along the surface will be evaluated by using thermography. Changing porous material characteristics due to the installation of heating wires will be quantified by comparison to far-field noise spectra of a porous TE without wires. Special attention will be paid to the change of porous material resistivity due to heated air flow and an experimental characterization of material parameters will be performed, using a heated resistivity rig.

Having stated the objectives of the research project, the required knowledge, which contributes to achieving the objectives, is defined in the form of two research questions and several sub-questions.

I. Is the proposed activation mechanism of heating up a coated porous TE effective in changing far-field noise characteristics?

   a) Are compliant material effects between surface pressure fluctuations and the heated coating material beneficial for noise mitigation?

   b) What is the achievable pore diameter change of the coated metal foam upon heating?

   c) Is there an observable change in far-field noise levels of porous TEs upon activation of the coating material?

II. To which extent are far-field noise levels affected by changing temperatures of porous TEs and what are the dominant influence factors?

   a) What is the functional relation between the resistivity of the permeable metal foam and flow temperature?

   b) How large is the change in broadband far-field noise levels upon heating of a solid/porous TE and do the results indicate the development of a thermal boundary layer?

   c) Does the installation of heating wires affect far-field noise characteristics of the porous TE and how sensitive are aeroacoustics with respect to changing wire temperature and placement inside the foam?

   d) Are microphone array measurements suitable for detecting small changes of far-field noise levels upon activation?

1.4. Structure of the Thesis Project

The research questions stated above are tackled by deriving theoretical relations between flow and material properties and examining their influences on far-field noise radiation. Experiments are designed in order to determine the validity of simplified theoretical considerations. In Chapter 2, the generation of TBL-TE noise is theoretically examined with a focus on turbulent boundary layer properties and the effects of temperature changes on the wall pressure spectrum.

A crucial factor for TBL-TE noise reduction through porous materials is the communication between suction and pressure side. Chapter 3 addresses important material parameters and equations used to describe the interaction between fluid flows and permeable materials. An experimental characterization of metal foam samples is performed including the effects of varying fluid temperature. The accuracy of the results is analyzed through uncertainty quantification and major error sources of the permeability rig are pointed out.

Beside the effects of fluid temperature, the proposed activation mechanism relies on changing geometrical properties upon heating of polymerically coated TEs. A theoretical study of possible coating effects on

far-field noise is addressed in Chapter 4. The change of pore size due to thermal expansion as well as compliance effects between pressure fluctuations and soft polymers are treated. The physical coating material properties are measured and achievable pore size changes are quantified experimentally.

The aeroacoustic performance of various activated and non-activated TE inserts is subject of Chapter 5. The experimental setup in the anechoic wind tunnel of TU Delft is described with a focus on the acoustic measurement technique and the quality of measured noise spectra. Far-field noise spectra of heated/non-heated solid and porous TEs are compared and conclusions regarding the dominant temperature effects are drawn.

The conclusions of the thesis project are summarized in Chapter 6. Answers to the research questions are outlined and recommendations for future research in the field of TBL-TE noise mitigation through porous materials are stated.

In the appendix, a somewhat different approach of relating changes in the airfoil resistivity to far-field noise levels is outlined. An existing numerical model, which is based on potential flow theory and vortex sound, is implemented and its applicability to the case of porous TEs is briefly discussed.

2

Pressure Fluctuations in Turbulent Boundary Layers

TBL-TE noise originates from wall pressure fluctuations which are convected past the TE. The structure and magnitude of these fluctuations is essential for understanding the TBL-TE noise generation mechanism. In the following chapter, the pressure characteristics in turbulent boundary layers, bounded by rigid as well as porous surfaces, are described. The coordinate convention used in this chapter is given in Figure 2.1.

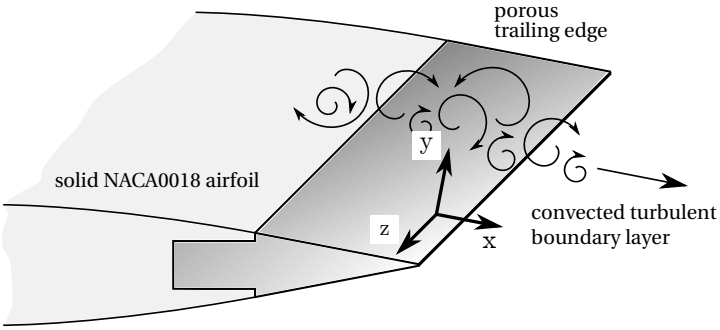

Figure 2.1: Airfoil geometry with porous TE insert as it was used in the experimental campaign. The description of turbulent boundary layer parameters is based on a surface-aligned coordinate system, i.e. the y-axis denotes the wall-normal direction.

2.1. Turbulent Boundary Layer Properties

Turbulent, wall bounded flows are subject to an extensive field of research. In this section, an overview of the most important properties of turbulent boundary layers is provided. According to White [43], fluid motions in turbulent flows are characterized by several properties:

- Velocity, pressure and temperature in turbulent boundary layers are *fluctuating* quantities around a certain mean value.

- A wide range of differently sized turbulent structures (eddies) form the unsteady velocity field within the turbulent boundary layer.

- Different fluid properties show a characteristic energy spectrum ranging from large, energy containing scales to small eddies. The fluctuations occur randomly but not in the form of white noise.

- Wall bounded turbulence is self-sustaining, i.e. turbulence energy is produced and dissipated.

- Strong mixing in the boundary layer leads to increased friction and influences the shape of the boundary layer velocity and temperature profile.

A detailed description of turbulent flow, including the turbulent energy cascade and the relation between velocity and pressure fluctuations, is given in [44].

The shape and size of the velocity profile in turbulent boundary layers serves as input for pressure spectrum models and is required for establishing scaling laws. The boundary layer thickness δ_0 is defined as the wall distance for which the mean velocity reaches 99 % of the free stream velocity. Further measures for the thickness are the displacement thickness δ^* and the momentum thickness Θ which are defined as:

$$\delta^* = \int_0^{y\to\infty} \left(1 - \frac{u(y)}{U_e}\right) \mathrm{d}y \quad \text{and} \tag{2.1}$$

$$\Theta = \int_0^{y\to\infty} \frac{u(y)}{U_e}\left(1 - \frac{u(y)}{U_e}\right) \mathrm{d}y. \tag{2.2}$$

Here, y denotes the wall normal coordinate, u is the local, streamwise mean velocity and U_e is the edge velocity above the boundary layer. The slope of the velocity profile directly at the wall determines the wall shear stress τ_w which is approximated by

$$\tau_w = \mu \left(\frac{\partial u}{\partial y}\right)_{y=0}, \tag{2.3}$$

where μ is the dynamic viscosity which is related to the kinematic viscosity ν through the density ρ of the fluid $\mu = \nu\rho$. The friction velocity u_τ is directly related to the wall shear stress in the form of $u_\tau = \sqrt{\tau_w/\rho}$. The wall shear stress can be normalized by the free stream dynamic pressure in order to obtain the friction coefficient $c_f = \tau_w/(1/2\rho U^2)$ with U denoting a characteristic speed, such as the inflow velocity. An approximate power-law expression can be used to calculated the boundary layer thickness and friction coefficient as a function of the local Reynolds number Re_L, assuming turbulent flow over a flat plate. For flow with a certain speed U, kinematic viscosity ν and a characteristic length L downstream of the leading edge, the local Reynolds number is defined as $Re_L = UL/\nu$.

2.2. Wall Pressure Spectrum

The pressure field within a turbulent, wall bounded flow can be subdivided into the *convective* and *acoustic* domain [25]. While the propagation velocity of the convective pressure fluctuations U_c is in the order of the flow speed U, fluctuations belonging to the acoustic regime propagate with roughly the speed of sound c_0. Radiation to the far-field is only effective in the acoustic regime i.e. only a certain part of the blocked surface pressure propagates as a sound wave to the observer.

2.2.1. Convection Velocity

In general, the convection velocity U_c of the pressure fluctuations within the boundary layer is not constant but varies with the shape and size of the wide range of turbulent scales. Brooks and Hodgson [45] argued that the center of larger structures is located further away from the wall and hence, their convection velocity is larger. In addition, the lifetime of a convected eddy has to be taken into account when measuring the convection velocity of an eddy between two points. Since the lifetime is proportional to the eddy size, Brooks and Hodgson [45] found that the convection velocity is mainly influenced by the scale of the eddy rather than by its frequency.

A wide variety of methods to determine the convection velocity with different levels of refinement exists and an extensive overview can be found in [46]. Choi and Moin [47] provided an expression for the convection velocity in turbulent boundary layers based on wall pressure spectra obtained from a channel flow DNS database. Their results for the convection velocity as a function of the streamwise spatial separation indicated values of $U_c \approx 0.8U$ for the large scales (i.e. large spatial separation) and $U_c \approx 0.6U$ for the small turbulent scales. In agreement with [25, 45], only a weak dependency on the pressure fluctuation frequency was observed. Brooks [45] conducted experimental surface pressure measurements close to the TE of a NACA0012 airfoil and determined the influence of streamwise sensor spacing on the convection velocity. The results showed a slightly wider variation in the range of $U_c \approx 0.4U$ to $U_c \approx 0.9U$ for small and large eddy scales, respectively.

The analysis of a turbulent pressure field is simplified if Taylor's hypothesis is applied. It assumes that the turbulent structures are spatially unaltered while being convected downstream with a constant convection

velocity U_c [48]. The constant value for the whole range of turbulence scales is approximately between $U_c = 0.6U$ and $U_c = 0.8U$ [25] which agrees well with the scale-dependent convection velocity ranges stated above.

2.2.2. Convective and Acoustic Domain

In the following, the composition of the turbulent boundary layer pressure field is described in the frequency domain in terms of the wavenumber vector $\vec{k} = (k_1, k_2, k_3)^T$ and the angular frequency ω. The relation between ordinary frequency f and angular frequency is given by $\omega = 2\pi f$. The components of the wavenumber vector are aligned with the coordinate axes (x, y, z), where x represents the streamwise direction, y is the offset from the wall and z denotes the spanwise coordinate. Directly at the wall, the vertical wavevector k_2 is zero. The energy distribution in different wall pressure regimes is obtained from the wavenumber-frequency spectrum $P(\vec{k}, \omega)$. Figure 2.2 depicts a schematic wavenumber-frequency spectrum for the flow aligned wavenumber k_1 and for a fixed frequency. The energy content of the pressure fluctuations is concentrated in the convective regime for wavenumbers around $k_c = \omega/U_c$ which represent small turbulent structures convected with velocity U_c. The larger structures, which form the acoustic domain, propagate with the speed of sound c_0 and only contribute little to the overall energy content of the wavenumber-frequency spectrum. For TBL-TE noise mitigation, the high-energy convective domain is of major importance since it can be scattered into acoustic waves upon encountering surface discontinuities such as roughness elements or trailing edges [25].

In the presence of a rigid wall, pressure fluctuations within a turbulent boundary layer are referred to as *blocked pressure*. The magnitude of the pressure fluctuation associated with a convected eddy is twice as large in the presence of a blocking wall compared to the same turbulent structure in the unbounded wake. A jump in the boundary conditions, as it occurs at the TE, therefore leads to pressure scattering [45].

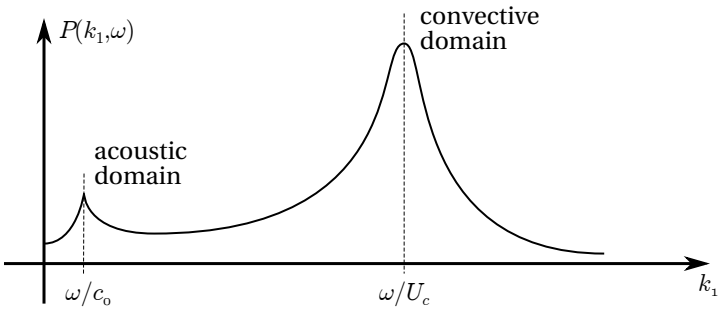

Figure 2.2: Shape of wall pressure wavenumber-frequency spectrum $P(k_1, \omega)$ as a function of the streamwise wavenumber k_1 for a fixed frequency ω [25].

2.2.3. Statistical Analysis of Fluctuating Pressure

Analyzing time series of the fluctuating surface pressure p_s involves several operations and definitions in the time and frequency domain which are addressed in the following. The wavenumber-frequency spectrum of the surface pressure in the frequency domain $P(\vec{k}, \omega)$ is obtained from the Fourier transform of the wall pressure cross-correlation. The latter is obtained from signal shifts in space and time, whereas the wall normal coordinate y is not considered since only the pressure spectrum at the surface of the wall is of interest. The cross-spectral density of the unsteady wall pressure fluctuations $\Phi_{pp}(\Delta x, \Delta z, \omega)$ depends on the frequency, the streamwise separation Δx and the spanwise separation Δz. For $\Delta x = 0$ and $\Delta z = 0$, the auto-spectral density of the surface pressure fluctuations $\Phi_{pp}(\omega)$ is obtained. It can be related to the wavenumber-frequency spectrum by

$$\Phi_{pp}(\omega) = \int_{-\infty}^{\infty} \int_{-\infty}^{\infty} P(k_1, k_3, \omega)\, \mathrm{d}k_1\, \mathrm{d}k_3 \,. \tag{2.4}$$

Integrating the pressure spectrum over the range of frequencies results in the mean square of the unsteady pressure fluctuations measured at a single point. The root-mean-square of the pressure fluctuations is abbreviated with p_{rms} in the following and it can be expressed as

$$p_{rms}^2 = \langle p_s^2 \rangle = \int_{-\infty}^{\infty} \Phi_{pp}(\omega)\, \mathrm{d}\omega \,. \tag{2.5}$$

The property p_{rms} depends on the free stream dynamic pressure $q = 1/2\rho U^2$. For turbulent boundary layers, it was found that p_{rms} equals to approximately 1 % of the dynamic pressure [49]. For compressible boundary layers, modifications of this value were suggested due to changes of wall shear stress τ_w, Mach number M and wall temperature T_w [50]. The modified analysis implies that even for low Mach numbers a changing wall temperature influences the relation between p_{rms} and q. Howe [25] used the following expression for the modified relation in the compressible case

$$p_{rms} = \frac{0.01\frac{1}{2}\rho U^2}{\frac{1}{2}\left(1+\frac{T_w}{T_\infty}\right)+0.1(\gamma-1)M^2} \,. \tag{2.6}$$

Here, T_w and T_∞ refer to the wall temperature and the ambient temperature, respectively and γ is the ratio of specific heats. The factor 0.01 represents the ratio of p_{rms}/q in the incompressible case.

2.2.4. Modeling Wall Pressure Fluctuations

A variety of semi-empirical wall pressure spectrum (WPS) models exist for different flow cases. An extensive overview is given in [51]. Among others, Goody [52] developed a model for the WPS in zero pressure gradient boundary layers. The main focus of several semi-empirical models is to provide a Reynolds number scaling of the pressure spectrum $\Phi_{pp}(\omega)$.

A general expression for semi-empirical wall pressure spectrum models can be given in the form of [51]

$$\frac{\Phi_{pp}}{\Phi^*} = \frac{a(\omega/\omega^*)^b}{\left(i(\omega/\omega^*)^c+d\right)^e+\left(fR_T^g\omega/\omega^*\right)^h} \,. \tag{2.7}$$

The constants a to i differ for different WPS models and tuning their values allows to describe the different scaling regions of the wall pressure spectrum for a certain flow case. R_T represents the ratio between outer-layer time scales and inner-layer time scales. The scaling factors Φ^* and ω^* are applied to the wall point pressure frequency spectrum Φ_{pp} and the frequency ω, respectively. These factors contain several boundary layer parameters which vary for different models.

Goody's empirical wall pressure spectrum model aims at providing a self-similar solution for a wide range of Reynolds numbers. The model constants were tuned to represent the pressure spectrum characteristics of a two-dimensional boundary layer with zero pressure gradient. The values of the model constants a to i are listed in Table 2.1. The time scale ratio is defined as $R_T = (\delta_0/U)/(\nu/u_\tau^2)$. In order to express the spectral density and the frequency non-dimensional, the scaling factors $\Phi^* = \tau_w^2\delta_0/U$ and $\omega^* = \delta_0/U$ are used, respectively.

a	b	c	d	e	f	g	h	i
3	2	0.75	0.5	3.7	1.1	-0.57	7	1

Table 2.1: Constants of Goody's empirical wall pressure spectrum model

The model is based on experimental pressure spectra from several different research groups and it provides accurate results for a large Reynolds number range. In order to scale surface pressure measurements from zero pressure gradient flows according to the model, the following boundary layer properties are required: boundary layer thickness δ_0, wall shear stress τ_w, velocity U, kinematic viscosity ν and density ρ.

2.2.5. Scaling of Wall Pressure Spectrum

According to Goody [52], a general scaling law of the WPS for the whole frequency range does not exist; however, such laws exist for certain frequency ranges. The high-frequency range can be scaled with *inner* boundary layer characteristics i.e. the pressure is normalized with the wall shear stress τ_w and timescales are divided by ν/u_τ^2. If inner scaling is applied to the spectral density $\Phi_{pp}(\omega)$ and the frequency ω, the high-frequency spectrum scales with ω^{-5}. In the low-frequency range, the pressure is commonly scaled with τ_w or the dynamic pressure of the free stream q, while time scales with δ^*/U_e. In this region, a general scaling with ω^2 was observed. Goody [52] compared results from various wall pressure studies and concluded that in the overlap region between low- and high-frequency spectra, the spectral density scaling is in the order of $\omega^{-0.7}$ to $\omega^{-0.8}$. The characteristic scaling regions of the wall pressure spectrum according to Goody [52] are depicted in Figure 2.3.

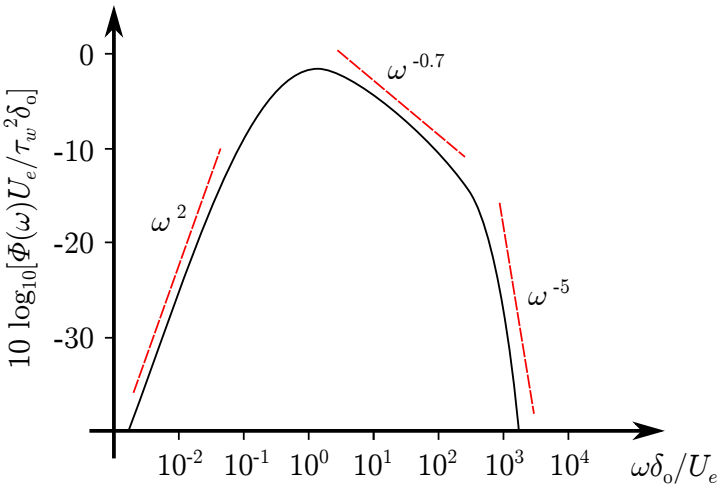

Figure 2.3: Typical shape of wall pressure spectrum according to [52]. Non-dimensional spectral density and frequency are plotted logarithmically and general scaling regions are indicated in red.

Surface pressure fluctuations above rough, non-permeable surfaces have been subject to a number of studies. Meyers et al. [53] experimentally investigated the wall pressure spectrum for a variety of different surface roughness seizes and geometries. They used different non-dimensional variables for presenting their results with the goal of finding general scaling laws for the pressure spectrum of rough surfaces. A common feature of most scaling approaches is the use of roughness height as an additional length scale.

If the effect of porosity is included in the wall pressure analysis, general scaling laws for smooth, rigid surfaces are expected to deviate from measured pressure spectra. Showkat Ali et al. [38] measured the surface pressure above porous TEs. Their results showed that the power spectral density deviated from the prediction of Goody's empirical model. However, for porous surface cases where roughness is the dominant effect, scaling laws based on the roughness height might be applicable.

2.3. Boundary Layers over Permeable and Rough Surfaces

Calculations in the previous sections are restricted to zero pressure gradient flows over smooth, solid surfaces. The use of porous TEs for noise mitigation requires to consider the special case of rough, permeable walls. For permeable surfaces, the fluid is able to penetrate the material and the streamwise flow component at the wall does not vanish. Beavers and Joseph [54] proposed that the slip velocity on the surface is different from the flow velocity inside the porous material. The flow within the porous material can be characterized by Darcy's law (Sec. 3.1) which relates the seepage velocity v_s to permeable material properties. Figure 2.4 illustrates the relation between the slip velocity and v_s and qualitatively shows the boundary layer behavior across the interface of the porous material and the free fluid. With changing turbulent boundary layer properties over

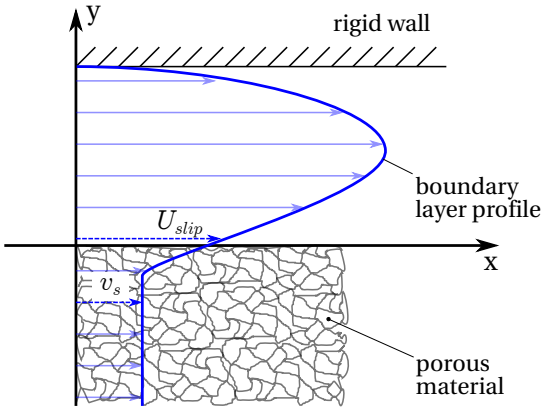

Figure 2.4: Boundary layer profile of flow over a porous material according to [54]. The channel flow is bounded by a solid top wall and permeable material at the bottom.

rough, permeable walls, the wall pressure spectrum is consequently influenced as well. The magnitude of the wall pressure spectral density $\Phi_{pp}(\omega)$ increases together with boundary layer thickness and enhanced turbulence intensity above rough walls occurs. The roughness height k and type of roughness influences the quantitative change of the pressure fluctuation magnitude [53].

The mechanism of TBL-TE noise generation relies on the scattering of pressure fluctuations in the convective domain into the acoustic domain. This process can be triggered by surface roughness elements [25] and therefore, TE noise from airfoils with porous TEs differs from smooth surfaces. Glegg and Devenport [55] distinguished three effects of surface roughness, namely the increase of turbulence in the boundary layer, higher skin friction drag and additional scattering of convected pressure fluctuations at the roughness elements. The connection between rough surfaces and radiated noise was investigated analytically and experimentally by Liu et al. [56]. The spectral peak of roughness noise varied with roughness height and distribution. Considering a full-size aircraft wing, it was found that roughness noise peaks at higher frequencies than TBL-TE noise and is the dominant noise source in this region.

2.4. Thermal Effects on Pressure Fluctuations

Active change of porous TE noise mitigation characteristics is achieved through TE heating. The impact of surface heating on the wall pressure spectrum is evaluated in the following in order to predict possible far-field noise effects and interpret experimental results.

Wall heating with the intention of reducing skin friction drag has been investigated in studies such as from Kramer et al. [57]. For flow over a heated surface, a temperature boundary layer develops analogous to the velocity boundary layer. Directly above the wall, the flow temperature equals to the wall temperature T_w while far away from the wall, the free stream temperature T_∞ is present. The fully developed temperature boundary layer thickness and shape depends on the Prandtl number which is a function of the fluid only [43]. The temperature close to the wall influences the fluid properties, namely density and viscosity. Since the skin friction drag is a function of the air density and viscosity, it can be shown that the drag ratio of a heated and non-heated wall is proportional to the temperature ratio $(T_w/T_\infty)^{-2/3}$ [57].

Like skin friction reduction through wall heating, the influence of a temperature change on the wall pressure spectrum can be analyzed based on changing fluid properties. In Sec. 2.2.5, the scalability of wall pressure spectra was discussed. The power spectral density of the surface pressure fluctuations can be scaled with the wall shear stress τ_w in the low- and high-frequency regime. Expressing the wall shear stress in terms of the friction coefficient and applying the approximation for flat plate boundary layers, the dependency on flow properties becomes apparent from

$$\tau_w = \frac{1}{2}\rho U^2 \frac{0.027}{Re^{1/7}} = \frac{1}{2}\rho U^2 \frac{0.027}{(UL/\nu)^{1/7}} \,. \tag{2.8}$$

It can be inferred that the wall pressure scaling is proportional to the density and kinematic viscosity in the form $\tau_w \propto \rho\nu^{1/7}$. The ideal gas law provides an expression for air density ρ as a function of temperature

$$\rho = \frac{p_\infty}{R_{air}\,T} \,. \tag{2.9}$$

Here, p_∞ denotes the pressure and $R_{air} = 287\,\mathrm{J\,kg^{-1}\,K^{-1}}$ is the specific gas constant of air [43]. In the following calculations, it is assumed that the pressure is constant and equal to the international standard atmospheric pressure at sea level $p = 1.01325 \times 10^5\,\mathrm{Pa}$. An approximate relation between the dynamic viscosity μ and temperature T is given by Sutherland's law [43]

$$\mu = \mu_0 \left(\frac{T}{T_0}\right)^{3/2} \frac{T_0 + S}{T + S} \,. \tag{2.10}$$

For air, the constants are $T_0 = 273\,\mathrm{K}$, $\mu_0 = 1.716 \times 10^{-5}\,\mathrm{N\,s\,m^{-2}}$ and $S = 111\,\mathrm{K}$.

The expected wall pressure spectrum of heated flow can be estimated from Goody's model by using a flat plate approximation of the boundary layer thickness δ_0 and the wall shear stress τ_w. This results in the temperature dependent scaling factors

$$\Phi^* = \left(\frac{1}{2}\rho(T)U_e^2 \frac{0.027}{(U_e L/\nu(T))^{1/7}}\right)^2 \frac{0.16\,L}{(U_e L/\nu(T))^{1/7}} \frac{1}{U_e} \quad \text{and} \tag{2.11}$$

$$\omega^* = \frac{0.16\,L}{(U_e L/\nu(T))^{1/7}} \frac{1}{U_e} \,. \tag{2.12}$$

Figure 2.5 shows the wall pressure spectral density Φ_{pp} as a function of the frequency ω for two fluid temperatures $T_1 = 20\,°\text{C}$ and $T_2 = 100\,°\text{C}$. The spectrum is plotted according to Eq. 2.7 using the coefficients of Goody's law. Qualitatively, it can be seen that the spectral density of the wall pressure fluctuations decreases with increasing wall temperature and that higher frequencies are influenced stronger. In order to verify this prediction, the pressure spectral density was integrated over the whole frequency range according to Eq. 2.5. The resulting root-mean-square of the pressure fluctuations above the cold and the hot wall amounted to $p_{rms,1} = 11.28\,\text{Pa}$ and $p_{rms,2} = 8.65\,\text{Pa}$, respectively. A comparison with the modified expression for the pressure root-mean-square used by Howe [25] for compressible boundary layers indicates the same trend. Applying Eq. 2.6 results in $p_{rms,1} = 9.63\,\text{Pa}$ and $p_{rms,2} = 6.66\,\text{Pa}$ for the two wall temperatures, respectively.

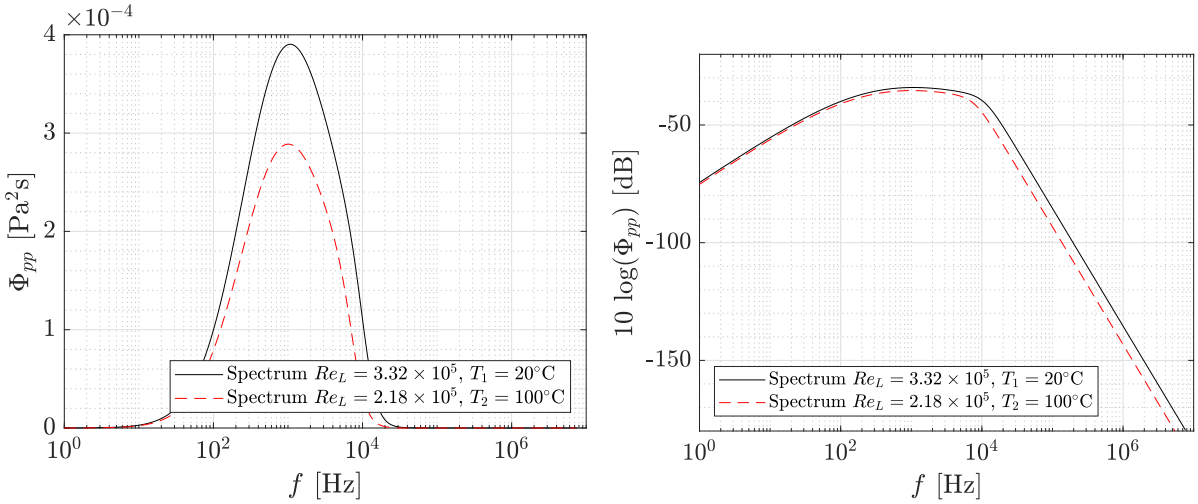

Figure 2.5: Wall pressure spectrum Φ_{pp} (left) and logarithmic spectrum $10\log(\Phi_{pp})$ (right) for two different fluid temperatures. The spectral shape is based on Goody's empirical model [52].

3

Flow Through Porous Materials

Communication between suction and pressure side is a key factor for TBL-TE noise mitigation through porous materials [32, 35]. If steady flow through porous media is regarded in a macroscopic way, the particular geometrical structures of the pores are not considered but rather the overall impact on properties of the mean flow. Empirical relations indicate that the flow resistance imposed by porous materials depends on geometrical constants as well as on fluid properties. Both factors can be actively modified with the goal of influencing the noise mitigation characteristics of porous TEs and this chapter discusses the effects of changing fluid temperature on flow resistivity. An existing resistivity measurement rig was modified in order to investigate thermal effects on flow resistivity of porous metal foams experimentally. Uncertainty quantification was carried out with the goal to assess the quality of the experimental data and to point out possible improvements to the experimental setup.

3.1. Characterization of Porous Materials

Geometrical characterization of porous materials can be performed based on properties such as the nominal pore size $d_{p,0}$ of the microscopic structures or the porosity φ. The latter is defined as the ratio of the fluid volume V_f inside the pores divided by the total volume V_t of the porous material

$$\varphi = \frac{V_f}{V_t} \,. \tag{3.1}$$

Interactions between porous materials and fluids depend on geometrical aspects as well as on flow properties. For flow speeds in the Stokes regime, a macroscopic relation between the seepage velocity v_s through the material and the accompanied pressure drop Δp along the thickness t of the material exists. The linear, empirical relation is given by the Hazen-Darcy equation [58] and can be written as

$$\frac{\Delta p}{t} = \frac{\mu}{K} v_s \,. \tag{3.2}$$

Here, μ denotes the dynamic viscosity of the fluid and the geometry dependent factor K is referred to as flow permeability. The seepage velocity $v_s = \dot{Q}/A$ is calculated from the volumetric flow rate $\dot{Q}$ passing through a sample with cross section A and since the porosity $\varphi < 1$, the actual flow speed through the sample is larger than the seepage velocity. Hazen-Darcy's relation accounts for viscous forces; however, form forces occurring at higher seepage velocities are neglected. These non-linear effects are captured by the Hazen-Dupuit-Darcy relation

$$\frac{\Delta p}{t} = \frac{\mu}{K} v_s + C\rho v_s^2 \tag{3.3}$$

with C being the form coefficient. The additional quadratic term is referred to as the inertia term and represents effects of fluid expansion/contraction and changes in flow direction within porous media. The necessity of using the Hazen-Dupuit-Darcy relation, i.e. including the second-order term, depends on flow and material properties. The two flow regimes are commonly separated by defining Reynolds number limits. In literature, a variety of Reynolds number definitions are used, mostly based on the flow speed, fluid viscosity and pore diameter of the porous material. Baloyo [59] provided an overview over Reynolds number limits

reported from different authors for liquid and gas flows. The nominal pore diameter does not directly relate to the material permeability and can be used if the porous material properties are not further specified. Lage [58] suggested to use the ratio between form and viscous forces

$$\frac{F_f}{F_{visc}} = \frac{\rho C K}{\mu} v_s \tag{3.4}$$

in order to evaluate if the second-order term needs to be considered. If an estimate of the material parameters C and K exists, this relation is preferred over a Reynolds number limit. Within the linear Darcy regime, the ratio μ/K is defined as the flow resistivity R which incorporates both, geometrical and fluid properties. A method to measure the resistivity is defined in standard ISO 9053 [60]. Furthermore, Darcy's empirical law is based on steady flow conditions and Philip [61] concluded that it is not valid for periodically changing pressure conditions. For oscillating flow, a dynamic permeability $K = K(f)$ can be specified. In general, the permeability of a porous material decreases with increasing flow frequency [62].

The permeable materials used in the experiments of this thesis consisted of open-cell, porous metal foams with homogeneously distributed pores. The NiCrAl metal foams were manufactured by the company Alantum and they are characterized by their nominal pore sizes in the following. A foam with a nominal pore size of 800 µm was used in the experimental investigation of thermal effects on flow resistivity. In a previous campaign [35], the physical properties of the metal foam, in the following referred to as P800, were specified as $\varphi = 91.65\,\%$, $R = 6728\,\mathrm{Nsm^{-4}}$, $K = 27.1 \times 10^{-10}\,\mathrm{m^2}$ and $C = 2612.54\,\mathrm{m^{-1}}$. Furthermore, a metallic foam with $d_{p,0} = 1200\,\mu\mathrm{m}$ was used as the basic material for polymeric coating. Figure 3.1 shows a microscopic image of the P800 and P1200 metal foam.

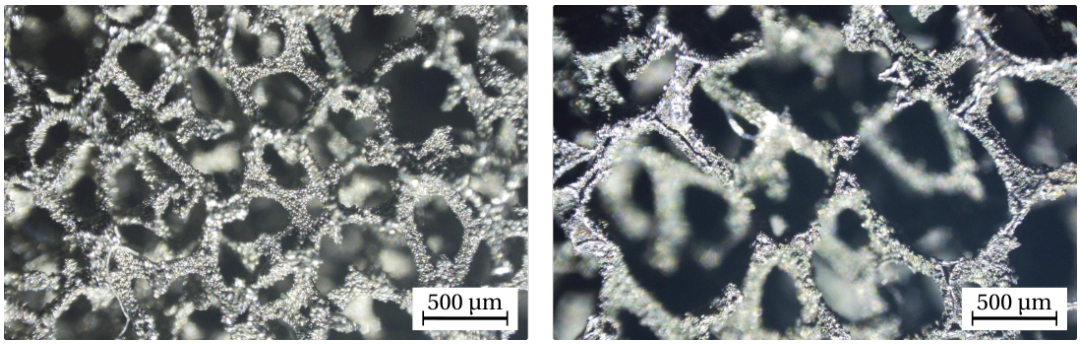

Figure 3.1: Microscopic images of the NiCrAl metal foams with nominal pore sizes of 800 µm (left) and 1200 µm (right)

3.2. Temperature Effects on Flow Through Porous Materials

From the definition of flow resistivity $R = \mu/K$ in the viscous flow regime, it follows that pressure communication can actively be influenced by changing either the material properties (represented by the permeability) or the fluid conditions.

The approximate relation between air temperature and viscosity (Eq. 2.10) can be simplified in the form of the power law

$$\frac{\mu}{\mu_0} = \left(\frac{T}{T_0}\right)^n , \tag{3.5}$$

where the exponent n depends on the fluid and reference temperature. For air, $n = 2/3$ is commonly chosen [43]. Incorporating the linear relation between viscosity and resistivity for porous materials, the relation

$$\frac{R}{R_0} = \left(\frac{T}{T_0}\right)^n \tag{3.6}$$

results. When non-linear effects are taken into account, the pressure drop Δp is additionally affected by the fluid density (Eq. 3.3) which can be related to the temperature via the ideal gas law (Eq. 2.9), according to which $\rho \propto 1/T$. Christie [63] experimentally studied the effects of temperature changes on the resistivity of fibrous materials. Up to a temperature of 400 °C, it was shown that a power law identical to Eq. 3.6 with an exponent of $n = 0.6$ agrees with experimental data. Measurements were restricted to the linear Darcy-flow regime.

Introduced as geometrical parameters, the permeability K and the form coefficient C are assumed independent from flow properties. However, for certain flow conditions, the effect of slip flow through the pores has to be taken into account. Pulkrabek and Ibele [64] investigated the effects of fluid temperature changes on the permeability of porous media. An apparent permeability $K' = K(1 + C_1\lambda)$ was defined where C_1 is a constant and λ is the mean free path of air molecules at atmospheric pressure. This correction becomes relevant when the mean free path of the fluid molecules lies in the order of the pore size, i.e. for dilute gas flows or small pore sizes. At atmospheric conditions, the mean free path is approximately 100 times lower than the pore diameter of the P800 material. Hence, temperature dependence of K and C due to slip effects is not expected.

An indirect relation between geometrical parameters and fluid temperature exists through thermal expansion of the porous material. A detailed analysis of thermal effects on the geometry of porous metal foams is addressed in Chapter 4. An increase in pore diameter for increasing temperature was not observed.

Viscous dissipation of turbulence kinetic energy within porous materials was mentioned as a potential noise mitigation mechanism by several authors [23, 24, 42]. Assuming that the linear Darcy relation holds, the work done by the pressure difference across the porous material has to be equal to the dissipated energy. The power which is dissipated into heat amounts to $\mu v_s^2/K$ and is identical to the power of the total drag force. For a heated fluid, the viscosity is increased and therefore also the dissipated energy. Nield [65] found that flow heating *caused* by viscous dissipation only becomes considerable for high flow speeds.

3.3. Experimental Setup

An experimental characterization of the porous metal foam properties for varying temperatures was performed by using the setup depicted in Figure 3.2. Pressurized air passed a diffusor and flowed through an electrical heating unit consisting of a coiled heating wire with an electrical resistance of 5.3 Ω. The heating unit was connected to an analog power supply with a maximum output of 500 W. The desired air temperature was controlled manually via adjusting the electric current supply of the heating system.

The heated air was forced through a porous metal foam sample and the static pressure drop along the sample was recorded by using a Mensor pressure gauge 2101 in differential mode with an accuracy of ±0.01 % of the full scale (FS) corresponding to 0.45 Pa [66]. The two pressure measurement points were located 5 cm upstream and downstream of the porous sample, respectively. Up to six cylindrical samples with a diameter of 5.5 cm and an individual height of 1 cm were stacked in order to capture the effects of sample thickness. The samples were tightly inserted into an aluminum tube which was clamped between two steel pipes with an inner diameter of 5 cm.

A Bronkhorst F-202AV mass flow controller was used to ensure constant air supply at a prescribed mass flow rate $\dot{m}$. The accuracy of the flow meter specified by the manufacturer is ±0.5 percent of the measurement value in addition to ±0.1 percent FS [67]. The full-scale contribution to the inaccuracy amounts to $\pm 5.6 \times 10^{-6}\,\mathrm{m^3\,s^{-1}}$ for the given air properties. The air temperature, required to calculate the volumetric flow rate $\dot{Q}$, was measured 1 cm downstream of the porous sample by using a type-K thermocouple. The seepage velocity through the porous sample followed from dividing the volumetric flow rate by the pipe cross-section $v_s = \dot{Q}/A_p$. Assuming ideal gas behavior, the seepage velocity can be expressed in terms of the mass flow rate through

$$v_s = \frac{\dot{m} R_{air} T_\infty}{A_p p_\infty} \,. \tag{3.7}$$

For multiple sample thicknesses and air temperatures, the mass flow rate set-point was varied in a range between $1.5 \times 10^{-4}\,\mathrm{kg\,s^{-1}}$ and $4.5 \times 10^{-3}\,\mathrm{kg\,s^{-1}}$ while the pressure drop was recorded. Quadratic least-square curve fitting in the form $\Delta p = C_a v_s + C_b v_s^2$ was applied to the measurement points in order to retrieve the linear and quadratic coefficients C_a and C_b which were related to the material parameters in Eq. 3.3.

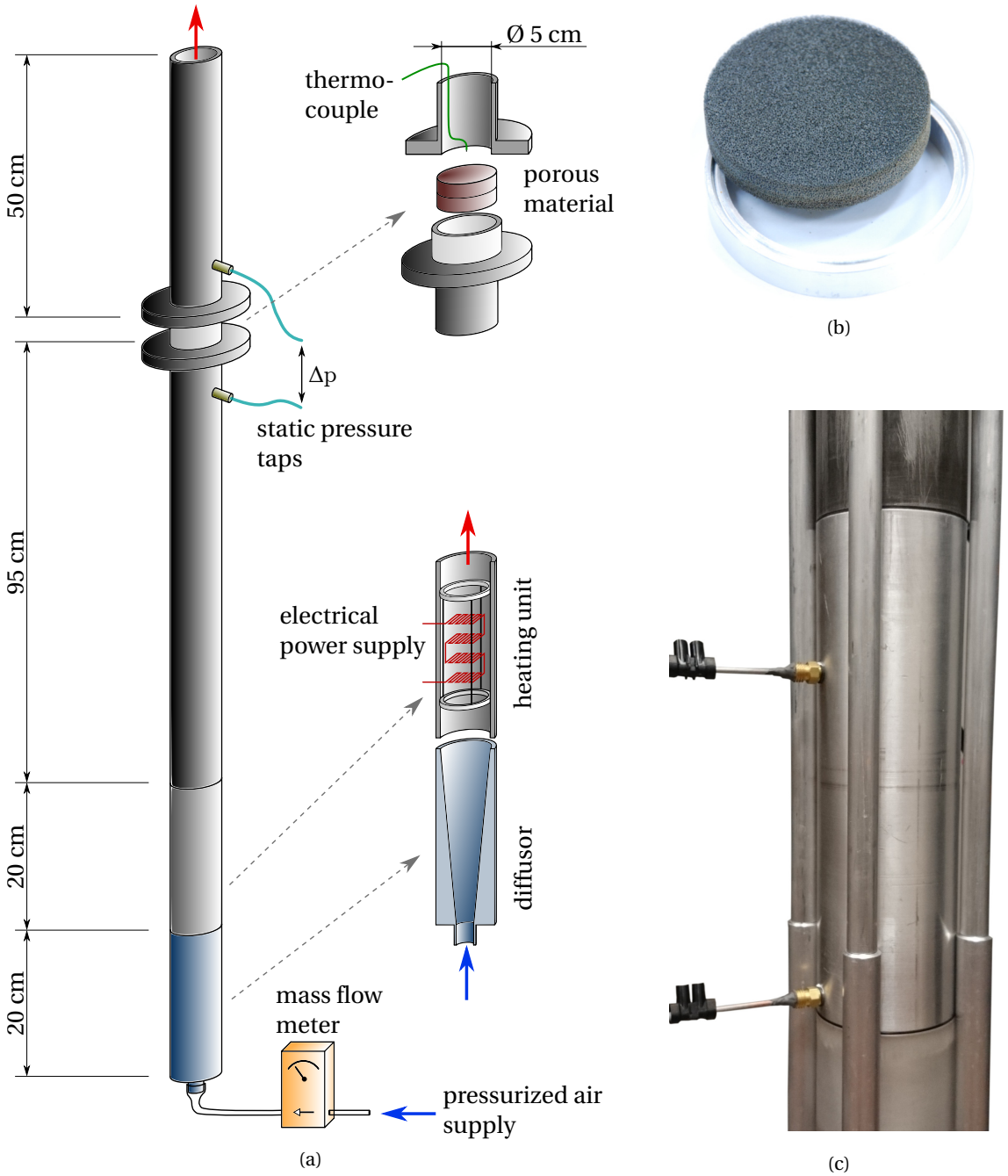

Figure 3.2: Experimental test rig used for specifying porous material properties at varying temperatures (a). Pressurized air was forced through a cylindrical material sample (b) and the static pressure drop was recorded. The existing test setup was expanded by installing a flow heating unit (c).

3.4. Experimental Results

In order to analyze sample thickness effects, measurements of the normalized pressure drop $\Delta p/t$ at ambient temperature were compared. Figure 3.3 depicts measured data points together with the fitted curves, indicated by dashed lines. With increasing thickness, the curves showed a trend towards lower normalized pressure drops, especially for high seepage velocities. The deviation between the normalized pressure drops can be primarily attributed to entrance and exit effects.

An experimental study on these effects was carried out by Baril et al. [68] for metal foams with different pore sizes and sample thicknesses. The microscopic geometry of the porous material used in their experiments matches closely to the P800 metal foam. Below a certain sample thickness, a non-linear relation between Δp and t was observed since the overall pressure drop was dominated by entrance and exit effects. These effects were considered to be negligible with respect to the bulk pressure drop for sample thicknesses larger than 50 times the pore size which corresponds to $t = 4\,\text{cm}$. In the following, it is therefore assumed that for $t \geq 6\,\text{cm}$ the linear relation between pressure drop and sample thickness, as suggested by the Hazen-Dupuit-Darcy equation (Eq. 3.3), holds true.

The influence of fluid temperature on the normalized pressure drop of a sample stack with $t = 6\,\text{cm}$ is shown in Figure 3.4 for the three temperatures $T = 22$, 50 and 90 °C. A limit for the linear region was defined based on Eq. 3.4 and in the following, the requirement $F_f/F_{visc} < 0.1$ is used. The requirement corresponds to $v_s < 0.25$ for the metal foam used in the experiments and a magnification of this region is included in Figure 3.4. Within the linear region, the normalized pressure drop increased with fluid temperatures while the opposite behavior was observed for higher seepage velocities. The results agree with the predictions based on Eq. 3.3 where the viscosity and density affect the linear and non-linear term, respectively. Neglecting the quadratic term of the Hazen-Dupuit-Darcy equation introduces a resistivity error which increases for higher seepage velocities. Figure 3.5 shows resistivity values that would result if only a single measurement of v_s and Δ_p would be used to calculate R according to Darcy's linear equation. For unknown values of R and C, a Reynolds number criterion for the linear region would be required.

The variation of the flow resistivity R with temperature is plotted in Figure 3.6 for different sample thicknesses. For $t = 6\,\text{cm}$, error bars indicate the interval around the mean in which 68 % of the simulated temperature and resistivity ratios lie (refer to Sec. 3.4.1). Additionally, the power-law based relation between resistivity and temperature (Eq. 3.6) was plotted for $n = 0.6$. The experimental results follow the same trend but indicate a slight offset from the expected relation. The highest change of resistivity with temperature was observed for the thickness $t = 6\,\text{cm}$. For lower sample thicknesses, deviation from the expected relation can partly be attributed to the dominance of entrance and exit effects since Darcy's relation does not hold true. Generally,

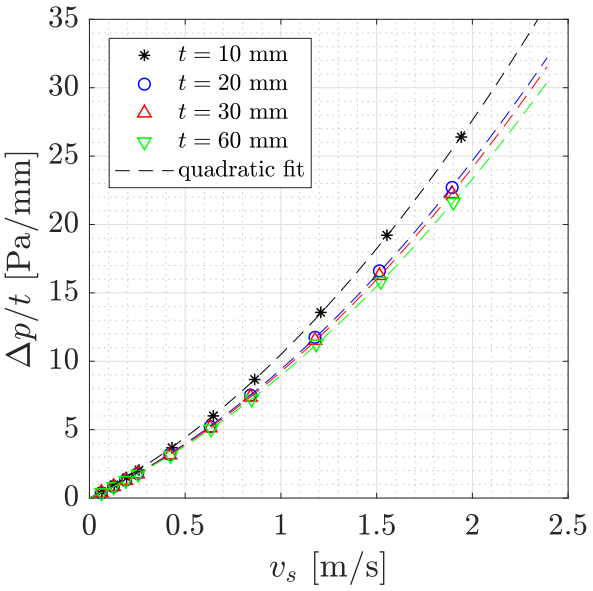

Figure 3.3: Normalized pressure drop along porous metal foam samples with varying thicknesses at ambient conditions. The dashed lines represent least-square quadratic fits to the experimental measurements.

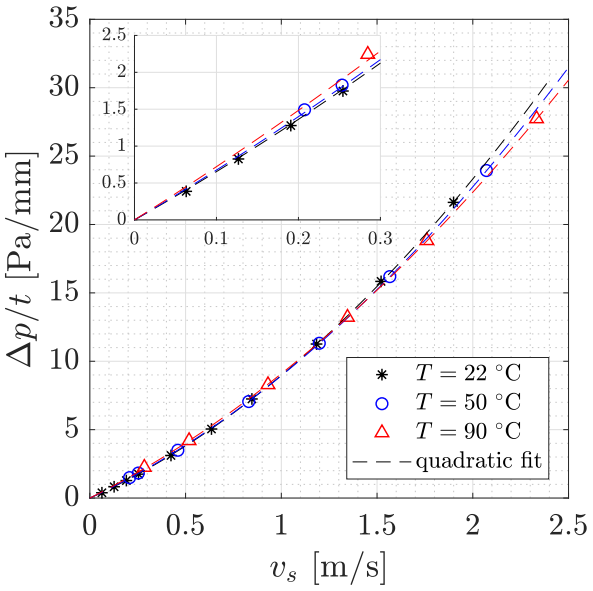

Figure 3.4: Change in normalized pressure drop along porous samples with $t = 6\,\text{cm}$ due to changing fluid temperatures. Quadratic curve fitting is indicated by the dashed lines and a magnification of the linear flow region is provided.

measurements at the higher temperature $T = 90\,°\mathrm{C}$ show better agreement with the theoretical prediction.

The effects of fluid temperature on permeability and form coefficient were determined by correcting the fitting coefficients C_a and C_b for the change in fluid viscosity and density, respectively. Figure 3.7 depicts the ratios of geometrical constants of the Hazen-Dupuit-Darcy relation for the temperatures $T = 50$ and $90\,°\mathrm{C}$ and a sample thickness of $t = 6\,\mathrm{cm}$. The uncertainty bounds of both ratios are included. From the experimental results it can be inferred that the geometrical coefficients were not independent from temperature. At $T = 90\,°\mathrm{C}$ the deviation with respect to ambient conditions lay in the order of 5 % for both coefficients. The variation with temperature could have been caused by geometrical changes of the porous material or the measurement setup itself due to thermal expansion. The combination of increasing permeability and lower form coefficient at higher temperatures implies that the measured pressure drop was lower than it would have been expected from theory. Even though the expected values $K/K_0 = 1$ and $C/C_0 = 1$ do not lie within the random uncertainty limits, it is assumed that additional systematic errors can explain the deviations. Thus, a clear temperature dependency of the geometrical constants cannot be derived. Data for higher flow temperatures would be required in order to assess possible thermal effects on permeability and form coefficient.

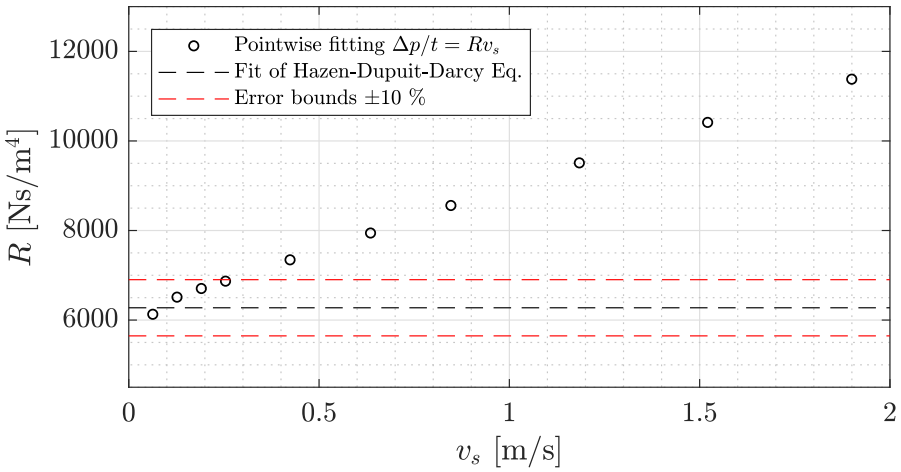

Figure 3.5: Flow resistivity R calculated from single measurement pairs of Δp and v_s under the assumption that Darcy's linear relation holds true. For comparison, the true value from quadratic fitting of multiple measurement pairs is plotted.

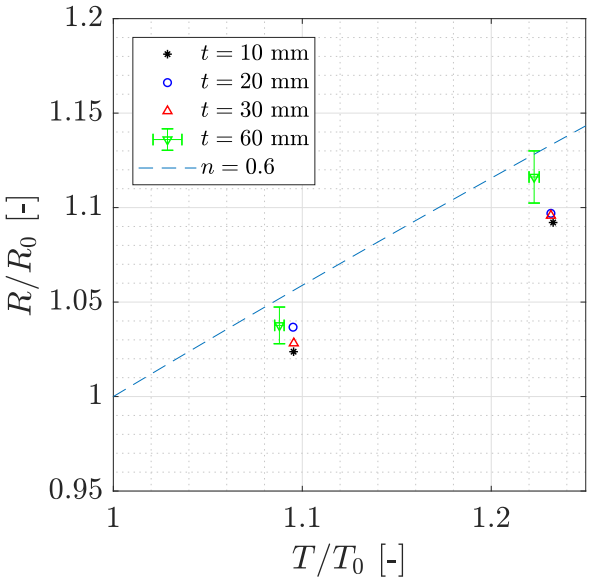

Figure 3.6: Change of flow resistivity ratio R/R_0 with temperature for different sample thicknesses. The theoretical relation given by the power law in Eq. 3.6 with $n = 0.6$ is plotted as reference. Error bars for $t = 6$ cm indicate regions which contain 68 % of simulated values.

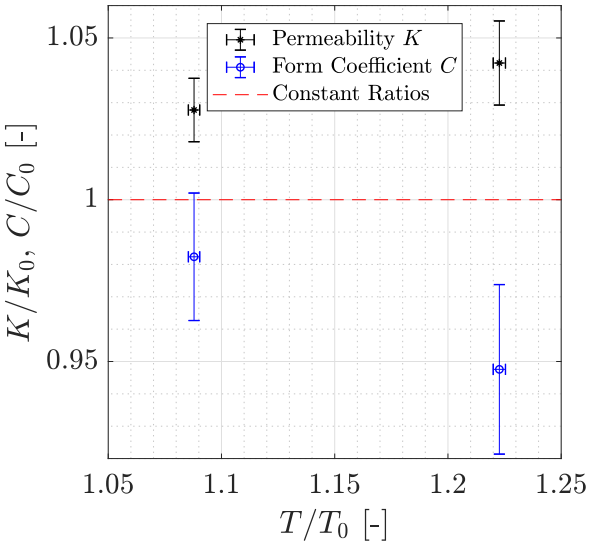

Figure 3.7: Change of material constants C/C_0 and K/K_0 with temperature for $t = 6$ cm. A constant ratio of unity, as expected from theory, is indicated by the dashed line. Error bars indicate regions which contain 68 % of simulated values.

3.4.1. Uncertainty Quantification

Uncertainty quantification was performed in order to evaluate the precision of the experimentally obtained material parameters C, K and R. A single measurement point consisted of the seepage velocity through the porous sample and the corresponding pressure drop. Both values contain uncertainties due to the limited accuracy of the measurement equipment and varying experimental conditions. The porous material parameters were obtained from a number of measurement points via least square fitting.

The match between data points and model can be quantified through the coefficient of determination R^2. If $R^2 = 1$, all data points perfectly represent the assumed quadratic relation between pressure drop and seepage velocity. The coefficient of determination for the fitting curves plotted in Figure 3.3 and 3.4 were larger than 99.99 % which indicates that the measurement points followed the Hazen-Dupuit-Darcy relation. However, high values of R^2 do not provide information about the accuracy of the model coefficients themselves.

In general, measurement uncertainties can be divided into random and systematic errors. The former can be reduced by repeating the experiment while the latter remains and is inherent to the measurement setup. Systematic errors could arise from flow leakage at the sample side walls or from an inhomogeneous seepage velocity and temperature distribution within the pipe. For every measurement point, the quantities $\dot{m}$ and Δp were obtained by averaging 50 data points which were recorded within 10 s. Data points were only acquired for converged flow conditions i.e. when the mass flow rate was within ±0.04 % FS around the set point. Assuming that the measurement points were normally distributed, the standard deviation is given by

$$\sigma = \sqrt{\frac{1}{N-1}\sum_{i=1}^{N}\left(M_i - \overline{M}\right)^2}, \tag{3.8}$$

where N is the number of data points, M_i is the value of a single measurement and $\overline{M}$ denotes the arithmetic mean. The distribution of measurement results around the mean is related to the repeatability of the experiment under the assumption that the measurement conditions remain unchanged. An estimate of the measurement accuracy is harder to obtain since systematic errors cannot be quantified. Table 3.1 lists the standard deviations σ and uncertainties u of the measurement devices provided by the manufacturers. Absolute and relative values are given for the measurement case $t = 6$ cm at ambient temperature and for a flow rate of $\dot{m} = 4.5 \times 10^{-3}\,\mathrm{kg\,s^{-1}}$. The standard deviations σ of the mass flow measurements agree with the repeatability (<0.2 %) of the device provided by the manufacturer and is much lower than the uncertainty of the device. The opposite was observed for the pressure measurements for which standard deviations are

likely to be dominated by fluctuations in $\dot{m}$. Including the accuracy of the measurement devices would result in large uncertainties of the material parameters in the order of 5 to 10 % while additional systematic errors from the measurement setup are still not taken into account. The following uncertainty quantification is restricted to random errors and focuses on the repeatability of the results rather than on estimating the deviation from the true value.

The histograms in Figure 3.8 show that the assumption of normally distributed measurements is justified. It can be inferred that mass flow rate and temperature were converged at the time of data acquisition. Only a single temperature value was recorded per flow case. The standard deviation and accuracy of the temperature measurements were estimated from observed variations during the 10 s acquisition period and from temperature offsets with respect to calibrated devices, respectively.

Since $v_s = v_s(\dot{m}, T)$ (Eq. 3.7), the standard deviation of mass flow rate $\sigma_{\dot{m}}$ and temperature σ_T affects the random error of the seepage velocity. Taking error propagation into account, the random uncertainty of the seepage velocity σ_{vs} follows from

$$\sigma_{vs} = \sqrt{\left(\frac{\partial v_s}{\partial \dot{m}}\sigma_{\dot{m}}\right)^2 + \left(\frac{\partial v_s}{\partial T}\sigma_T\right)^2} = \frac{R_{\text{air}}}{A_p p_\infty}\sqrt{(T\sigma_{\dot{m}})^2 + (\dot{m}\sigma_T)^2}\,. \tag{3.9}$$

The random errors of single measurements affected the precision of curve fitting parameters C_a and C_b. The problem of a so called errors-in-variables regression was tackled by using a Monte Carlo method. From the normal distributions of the fitting input variables Δp and v_s, random samples were drawn. Samples were not bootstrapped directly from the recorded data sets because of the limited number of measurements and due to the lack of experimental temperature data distributions. The conservative assumption of independent variables was made since the random errors of the pressure measurements could not be isolated from the variations in $\dot{m}$. Least-square curve fitting was applied to $N = 1000$ random data sets, resulting in probability distributions of the parameters C_a and C_b. The fitting parameters followed a normal distribution and their standard deviation was used to define intervals which contain 68 % of the Monte Carlo simulated data points. This interval can be interpreted as a confidence range of the actual fitting parameter value [69].

Figure 3.9 depicts the probability distribution of the fitting parameters $C_a = R$ and $C_b = \rho C$, corresponding to the case $t = 6$ cm at ambient temperature. The 68 % confidence range of both parameters is indicated in form of the standard deviation σ_{sim}. It is concluded that the random measurement errors affected the linear coefficient C_a less than the quadratic coefficient C_b.

The change of material coefficients with temperature was evaluated based on the ratios C/C_0,K/K_0 and R/R_0, where the index 0 refers to conditions at ambient temperature. The random uncertainty of a ratio between two error containing variables follows from error propagation (Eq. 3.9). Using the example of the resistivity, it follows

$$\sigma_{R-R} = \frac{1}{R_0}\sqrt{\sigma_R^2 + \frac{R^2}{R_0^2}\sigma_{R0}^2}\,. \tag{3.10}$$

The standard deviation of form coefficient and permeability resulted from the curve-fitting error plus the random error of the temperature dependent viscosity and density. To simplify the error analysis, it was assumed that the fluid properties and the curve-fitting coefficients were independent variables. From Eq. 2.9 and Eq. 2.10 it was deduced that a temperature deviation of $\sigma_T = 0.5$ K translates into $\sigma_\rho = \pm 2 \times 10^{-3}\,\mathrm{kg\,m^{-3}}$ and $\sigma_\mu = \pm 2.4 \times 10^{-8}\,\mathrm{N\,s\,m^{-2}}$ at ambient fluid conditions. An overview over the mean value and standard deviation of the material parameters is given in Table 3.2. The error bars in Figures 3.6 and 3.7 mark the standard deviations σ_{sim} of temperature ratios and material parameter ratios.

From the uncertainty analysis, it is inferred that random measurement errors affected the standard deviation of the form coefficient stronger than the precision of resistivity and permeability. This is more pronounced in the analysis of coefficient ratios due to error propagation. The analysis of random errors revealed the sensitivity of material coefficients to inaccuracies of the measurement setup. Systematic errors and the uncertainty of the devices (e.g. due to incorrect calibration) were not considered. However, it is expected that these errors can account for the differences between observed and expected temperature behavior. The major contributor to random errors was the fluctuating mass flow, even for converged flow conditions. Previous measurement campaigns relied on fluid temperature data from the flow meter. Deviations between the temperatures measured at the inflow of the test rig and directly downstream of the sample were observed in this campaign. For more accurate calculations of the seepage velocity, it is suggested to rely on temperature data acquired close to the porous sample.

	Mean	Std. deviation σ	σ [%]	Accuracy
Mass flow rate $\dot{m}$	$4.50 \times 10^{-3}\,\mathrm{kg\,m^{-3}}$	$6.1 \times 10^{-6}\,\mathrm{kg\,m^{-3}}$	0.13	$2.81 \times 10^{-5}\,\mathrm{kg\,m^{-3}}$
Pressure drop Δp	$1.30 \times 10^{3}\,\mathrm{Pa}$	3.8 Pa	0.29	0.45 Pa
Temperature T	296.45 K	0.5 K $^{(*)}$	0.17 $^{(*)}$	2 K $^{(*)}$
Seepage Velocity v_s	$1.90\,\mathrm{m\,s^{-1}}$	$4.1 \times 10^{-3}\,\mathrm{m\,s^{-1}}$ $^{(**)}$	0.22 $^{(**)}$	-

Table 3.1: Repeatability and accuracy of measurements, expressed in the form of standard deviations σ and uncertainty ranges, respectively. Properties marked with $(*)$ were estimated based on observed fluctuations during the experiments. Standard deviations which resulted from error propagation are indicated with $(**)$.

	Mean	Std. deviation σ	σ [%]
$R = C_a$ [Ns/m^4]	6274	46	0.73
$K = \mu / R$ [m^2]	2.9×10^{-9}	2.2×10^{-11}	0.75
$C = C_b / \rho$ [m^{-1}]	2242	36	1.61

Table 3.2: Mean and standard deviation of the material parameters as obtained from the Monte Carlo Simulation for $t = 6$ cm at ambient temperature. The parameters were derived from the fitting coefficients C_a and C_b under consideration of error propagation.

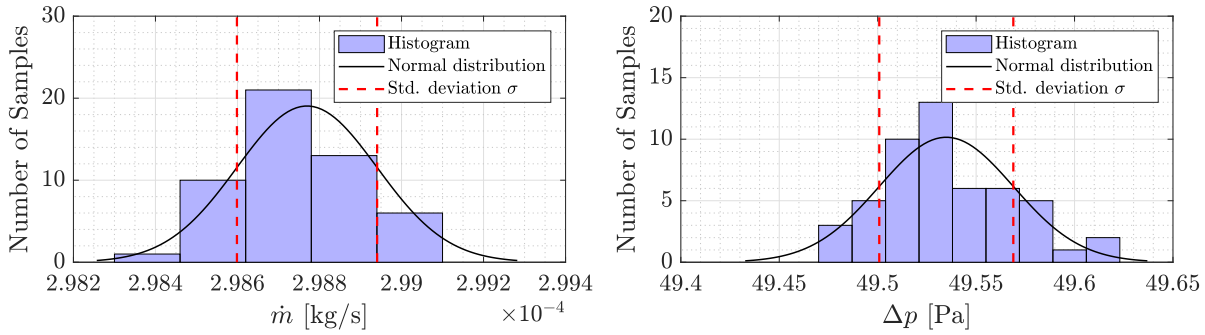

Figure 3.8: Histograms showing the quasi normal distribution of measured mass flow rates $\dot{m}$ and pressure drops Δp for the case $v_s = 0.13\,\mathrm{m\,s^{-1}}$. Red dashed lines mark the standard deviation of an approximate, continuous normal distribution.

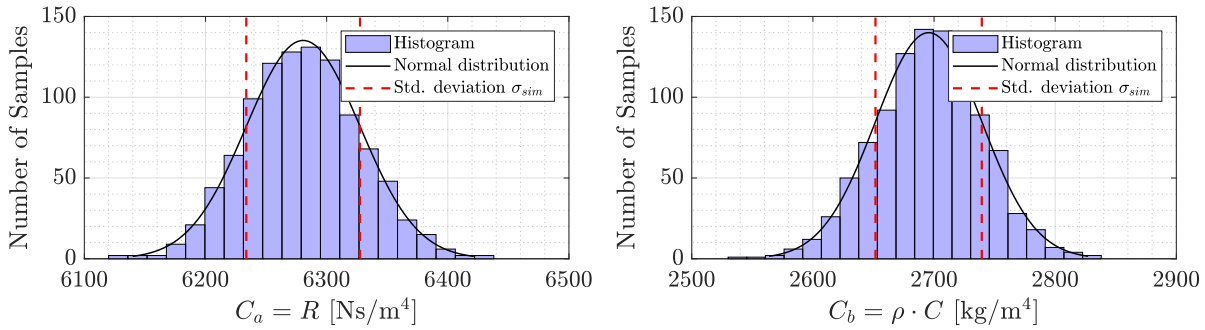

Figure 3.9: Histograms of fitting parameters C_a and C_b as a result of Monte Carlo sampling from uncertain input data. The 1000 samples were normally distributed and the standard deviations σ_{sim} represent the 68 % confidence intervals of the mean values.

4

Polymeric Coating of Porous Metal Foams

Noise reduction capabilities of porous TEs depend on macroscopic factors, such as the dimension and shape of the insert, as well as on the microscopic structure of the single pores. The focus in this chapter lies on active change of material properties on a pore-size scale. The use of open-cell metallic foams proved to be effective in mitigating low-frequency TBL-TE noise. Maintaining this general structure, active change in pore size through polymeric coating and heating of porous TEs is proposed. The achievable pore size variation is estimated analytically and verified experimentally. Beside geometrical influences, potential interactions between surface pressure fluctuations and the soft coating are addressed.

4.1. Pore Size Effects

Upon heating, the polymeric coating expands while the macroscopic geometry of the TE remains unchanged. Inside the metal foam, the ratio between fluid volume and solid material decreases and so does the porosity φ of the TE. Considering a simple, circular open cell structure as depicted in Figure 4.1, the change of porosity can be expressed through a change in pore diameter. The extent to which increasing temperature influences the porosity of the foam depends on the thermal expansion coefficient of the coating. The volumetric heat expansion coefficient α_v is defined as

$$\alpha_v = \frac{1}{V_0}\frac{\Delta V}{\Delta T}\,, \tag{4.1}$$

where V_0 is the initial volume and ΔV denotes the achievable change in volume for a temperature change ΔT. This relation is valid under the assumption that the change in volume is small and that the expansion coefficient is constant in the temperature range of interest. Motivated by the goal of actively influencing the properties of the porous metal foam, a high volume change of the coating material is desired. From Eq. 4.1, the conditions for maximum expansion ΔV of the coating material can be analyzed. The thermal expansion coefficient depends on the choice of coating material and its absolute value should be as high as possible. Regarding practical applications of activated porous materials, a negative thermal expansion (NTE) would be beneficial in the scope of airframe noise reduction. In this case, the natural temperature gradient in the atmosphere could be used to switch between higher flow resistivity at cruise conditions and opening pores during the final approach. Even though NTE materials exist [70], they were not considered suitable for TE coating. Some of the drawbacks are limited reversibility, a small temperature range in which NTE behavior occurs and the restriction to thin-film applications. The proposed mechanism of active pore size change upon heating was therefore investigated based on common, heat expanding materials. In general, the material group of polymers has high thermal expansion coefficients compared to natural materials, ceramics or metals [71]. The expansion of the metal foam structure was expected to be negligible with respect to the volume change of the polymeric coating.

For the choice of a suitable polymeric coating with high volumetric expansion coefficient α_v, the operating temperature should lie above the glass transition temperature T_g of the material. This temperature marks the transition between a hard, glassy material and a soft, rubbery material. Simha and Boyer [72] provided a list with thermal expansion coefficients for several polymers in the glassy and rubbery state. The thermal expansion coefficients in the rubbery regime (i.e. for temperatures above T_g) are roughly 2.5 times as high as

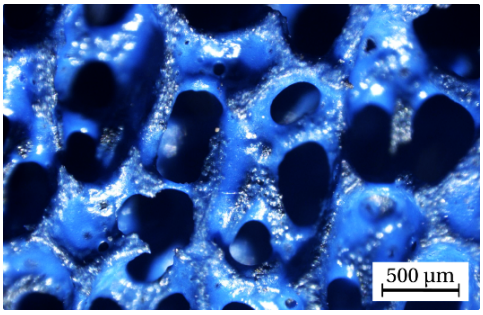

Figure 4.1: Microscopic image of polymerically coated metal foam surface

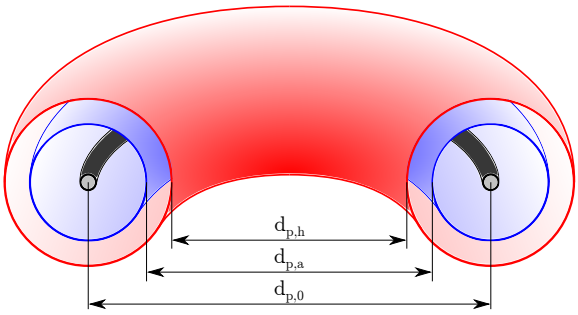

Figure 4.2: Schematic of circular metal foam pore covered with polymer (blue). Upon heating, the rubbery coating expands (red) and the inner pore diameter decreases.

in the glassy state. Above the glass temperature, typical values of the volumetric heat expansion coefficient are in the order of $\alpha_v = 8 \times 10^{-4}\,\mathrm{K}^{-1}$ for Polyurethane and $\alpha_v = 13 \times 10^{-4}\,\mathrm{K}^{-1}$ for Polyethylene.

For a given expansion coefficient, the temperature change ΔT, which is limited by the melting point of the material, should be as high as possible. In addition, a high initial polymer volume V_0 results in a larger expansion of the material. It is limited by the size of the metal pores since applying too many polymeric coating layers leads to complete closure of the pore structures.

The variation of pore size with temperature is illustrated in Figure 4.2. A circular cell with an initial, nominal pore diameter of $d_{p,0}$ is coated with a polymeric material such that the new pore size results in $d_{p,a}$ at ambient temperature. Regarding the coating as a torus around the metal structure, the required volume of coating material $V_{coat,a}$ at ambient temperature is

$$V_{coat,a} = 2\pi^2 \frac{d_{p,0}}{2} \left(\frac{d_{p,0}}{2} - \frac{d_{p,a}}{2} \right)^2 , \tag{4.2}$$

assuming that the volume of the metallic structure can be neglected. The volume change with increasing temperature can be calculated using Eq. 4.1 which results in $\Delta V = \alpha_v V_{coat,a} \Delta T$. Rearranging Eq. 4.2 and considering the volume change due to thermal expansion, the pore size $d_{p,h}$ in heated conditions amounts to

$$d_{p,h} = d_{p,0} - 2\sqrt{\frac{V_{coat,a}(1+\alpha_v \Delta T)}{\pi^2 d_{p,0}}} . \tag{4.3}$$

4.2. Compliant Material Effects

Thermal activation of the coated foam influences not only the geometrical properties of the porous TE but also the coating material characteristics. As mentioned in the previous section, the polymeric coating can behave as a hard, glassy material or as a soft, rubbery material, depending on the temperature. In the following, it is evaluated whether changing coating material properties, such as changes of the elastic modulus, influence the turbulent wall pressure spectrum. Based on a literature review, different possible compliant material effects are presented and their impact on TBL-TE noise reduction is discussed. The review is restricted to rigid, coated TE structures, while interactions of the fluid-structure type are not considered. The reader is referred to Howe [25], Herr [24] and Kamps et al. [26] for studies on TBL-TE noise reduction by means of limp TE extensions.

The concept of using a certain form of pressure-material interaction for noise reduction is used in different fields of research. The first group of studies concentrates on vibroacoustics i.e. the relation between structural vibrations and radiated noise. Strong surface pressure fluctuations in the convective pressure regime can excite structural vibrations which in turn are scattered into the acoustic domain when surface discontinuities are encountered [25]. Polymeric wall coatings are able to absorb vibrational energy and hence reduce scattered noise. Rao [73] listed several applications in which viscoelastic materials were used to damp structural vibrations. The damping characteristics of viscoelastic coatings strongly depend on temperature, mainly because the ratio of elastic modulus and loss modulus changes. In the scope of activated porous TEs,

the metallic foam can be regarded as a rigid, infinitely stiff structure which is not excited by turbulent boundary layer pressure fluctuations. In previous experiments [35, 36], no surface vibrations were reported for flow speeds up to $40\,\mathrm{m\,s^{-1}}$. A vibrating porous structure would have resulted in distinct peaks in the far-field noise spectrum, which was not observed. To conclude, dampening surface coatings are only effective if the subjacent structure vibrates. For rigid structures, changing viscoelastic material properties upon heating are not expected to affect TBL-TE noise generation.

Another research area is dedicated to the *acoustic* damping characteristics of soft coatings. Zheng [74] developed an analytical model for predicting the radiated noise of turbulent flow over a compliant wall. The analysis relied on acoustic wave propagation within the coating material and reflection at the interface between soft coating and rigid wall. Howe [75] investigated the effects of compliant coatings on pressure fluctuations originating from shed vorticity. The material property of interest in studies of this kind is the acoustic impedance i.e. the coating surface reaction to incoming *sound* waves. However, for TBL-TE noise reduction, the acoustic domain only plays a minor role compared to the convective domain, in which pressure fluctuations propagate much slower than with the speed of sound (refer to Sec. 2.2.2). Pressure fluctuations in the convective pressure regime need to be damped before being scattered into the acoustic domain at the TE.

A third field of research focuses on the use of compliant coatings for skin friction drag reduction. Under certain conditions, the turbulent structures close to the wall can interact with the soft coating and are potentially damped. This interaction is either employed to delay turbulent transition by damping flow instabilities or to influence turbulent structures close to the wall. Gad-El-Hak [76] summarized previous experiments in the field of compliant coating research. It is pointed out that substantial drag reduction achievements by different groups of researchers are highly controversial and many results proved to be irreproducible. Reduction in skin friction drag through compliant coatings is accompanied by attenuated surface pressure fluctuations in the *convective* domain. In the following, the effects of surface compliance are evaluated and it is argued that applicability in the scope of TBL-TE noise reduction strongly depends on flow and material properties.

Two different approaches exist for explaining the influence of compliant surfaces on turbulent structures close to the surface. The first theory suggests that turbulent energy is dissipated in the coating through compression and expansion caused by fluctuating wall pressure. Kulik [77] investigated the validity of the first theory by estimating the amount of turbulent energy that is dissipated in a viscoelastic coating. An important parameter in this analysis is the *compliance* of the coating material which represents the ratio between the coating surface deformation and the applied wall pressure. It is a function of the pressure fluctuation statistics and the coating thickness. Furthermore, the mechanical properties of the material, namely density, Poisson's ratio and complex elastic modulus, influences the compliant behavior. For a given wall pressure spectrum, the wall-normal surface displacement amplitude was derived by Kulik [77]. Subsequently, the energy dissipated within one period of compression and expansion of the coating material was related to the dissipation of turbulent energy by frictional forces. Viscous dissipation occurs for all wall-bounded flows and therefore, it is an appropriate measure to evaluate the dissipation capabilities of the soft coating. Kulik [77] concluded that the energy which is absorbed by the coating is negligible compared to the energy that is dissipated by viscous forces close to the surface. His results include varying material properties, coating thicknesses and flow speeds which are representative for the flow conditions and materials used in this thesis. For water, even at the strongest point of interaction (i.e. resonant behavior of the coating), the ratio of energy dissipated in the coating $E_{d,c}$ over viscous dissipation $E_{d,v}$ is in the order of $E_{d,c}/E_{d,v} \approx 5 \times 10^{-4}$. For air flow, the compliance of the coating is much lower and hence, dissipation in the viscoelastic material is further decreased and a ratio of only $E_{d,c}/E_{d,v} \approx 10^{-6}$ results.

From the previous analysis, it is inferred that dissipation of turbulent energy, even in the case of soft coatings, cannot account for Reynolds stress reduction. The second theory relies on induced surface waves and interaction of the moving coating surface with the fluctuating fluid velocities close to the wall. This way, the Reynolds stresses are directly influenced and damping of turbulent motions occurs if there is a phase shift between the moving surface and the turbulent motions. Kulik [77] showed that the velocity magnitude of the excited coating surface is in the same order as the fluctuating velocity components in the flow. Maximum interaction between the turbulent flow and the coated surface is desired for effective reduction of Reynolds stress. This is achieved by carefully considering the flow characteristics and by tuning the material properties accordingly. Kulik et al. [78] analyzed the required coating properties for effective drag reduction with a focus on mechanical wave propagation in the viscoelastic material. The effects of longitudinal waves due to

compression and expansion of the material surface as well as transverse shear waves were considered. Two requirements have to be fulfilled for maximum compliance. First, the frequency of the fluctuating properties in the boundary layer has to match the resonant frequency of the coating and second, the wavelengths of both oscillations have to be matched.

The model of elastic wave propagation in the coating material used by Kulik et al. [78] suggests that the first resonance wavelength λ_0 of the deformation wave directly depends on the coating thickness $\lambda_0 \approx 3t$. The resonance frequency ω_0 and the propagation velocity V_0 of the surface waves at resonance depend on the loss tangent μ_l and Poisson's ratio σ of the coating. An approximation of the resonance properties (for $\mu_l < 0.1$) is [78]

$$\omega_0 = \frac{C_t}{t}(2.244 + 1.96\sigma) \quad \text{and} \tag{4.4}$$

$$V_0 = C_t(2.826 - 4.5\sigma + 3.9\sigma^2)\,. \tag{4.5}$$

The propagation velocity of transverse shear waves within the material is denoted with C_t. It depends on the elastic modulus E, the density and Poisson's ratio of the material and can be approximated by [79]

$$C_t = \sqrt{\frac{E}{2\rho(1+\sigma)}}\,. \tag{4.6}$$

The resonance frequency ω_0 of the material surface should lie close to the dominant frequency of the wall pressure fluctuations if compliance between flow and coating is desired. In Section 2.2.5, the wall pressure scaling was addressed. The typical frequency range, for which the spectral density is highest, can be deduced from this analysis. Kulik et al. [78] used an empirical estimation of the frequency region around the spectral density peak. Their requirement for the material's non-dimensional resonance frequency reads as

$$6.67 \times 10^{-3} < \frac{f_0 \nu}{u_\tau^2} < 2.00 \times 10^{-2}\,. \tag{4.7}$$

For this expression, it is assumed that the inner scaling law for the frequency is applicable. The requirement of meeting a certain resonance frequency f_0 poses a constraint on the friction velocity u_τ and therefore prescribes flow velocity and Reynolds number.

The second condition for maximum interaction between flow and compliant material is the coincidence of wavelengths. This can be achieved by matching the speed of the surface waves V_0 to the convection velocity U_c of the pressure fluctuations which results in the requirement

$$V_0 = U_c\,. \tag{4.8}$$

Since $V_0 = V_0(\sigma, E, \rho)$ (Eq. 4.5 and Eq. 4.6), the second condition restricts the material choice for a given flow speed U.

The previous analysis shows that material properties and flow conditions cannot be chosen independently. Kulik et al. [78] predicted certain combinations of coating thickness t and flow speed U which were expected to result in skin friction reduction. Here, the compliance between air flow and a relatively stiff coating is of interest. Soft, gel-like materials are not sturdy enough to be applied as internal coating for metallic foams. An experimental study, which focuses on the specific case of low-speed air flow over stiff coatings, was carried out by Boiko et al. [79] with the goal of verifying drag reduction. For flow speeds in the order of $30\,\mathrm{m\,s^{-1}}$ and a coating stiffness of $E \approx 1.1\,\mathrm{MPa}$, they reported a skin friction drag reduction of $< 5\,\%$. Their study showed that compliance between a stiff coating and low-speed flow results in measurable reduction of turbulence intensity close to the wall.

The required parameter space for compliant flow-material interaction was estimated by using the two conditions from Eq. 4.7 and Eq. 4.8. Table 4.1 lists the underlying coating material properties and flow parameters which are representative for the test conditions described in Sec. 4.3 and Sec. 5.1, respectively. Since the modulus of the rubbery coating depends on temperature, two different elasticities were chosen to demonstrate their influence on the parameter space. Figure 4.3 shows the required coating thickness t for varying flow speeds U and different combinations of E/ρ.

It can be inferred that a reduced elastic modulus generally results in lower required flow speeds and higher coating thicknesses. For the low elasticity value, the minimum coating thickness has to be in the order of 10 mm for compliant behavior. This value cannot be reached for coated metallic foams with pore sizes in the

order of 1 mm. The required thickness can be reduced by choosing a material with higher modulus. However, matching the propagation speed of the material waves to the convection speed of the pressure fluctuations means that interaction is only possible for high speeds. In order to verify that the frequency region proposed in Eq. 4.7 is suitable, the frequency limits for the investigated case (with $U = 25\,\mathrm{m\,s^{-1}}$) were calculated. Figure 4.4 depicts the pressure spectrum according to Goody's model. The chosen frequency region of interest for the compliance estimation agrees well with the maximum spectral density.

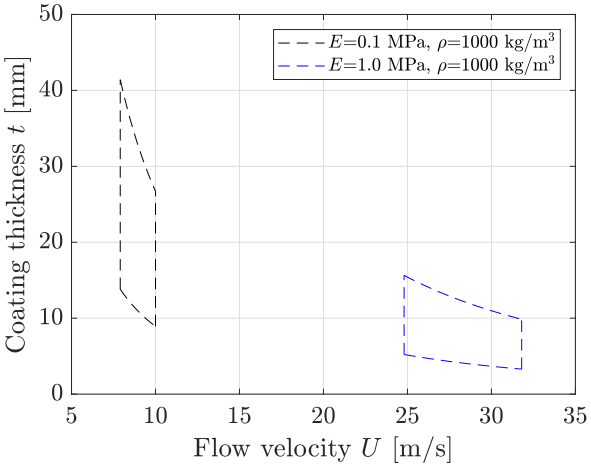

Figure 4.3: Theoretical compliance limits based on conditions in Eq. 4.7 and 4.8 for different material properties. Combinations of thickness t and flow speed U which lie within the bounds could result in fluid-surface interactions.

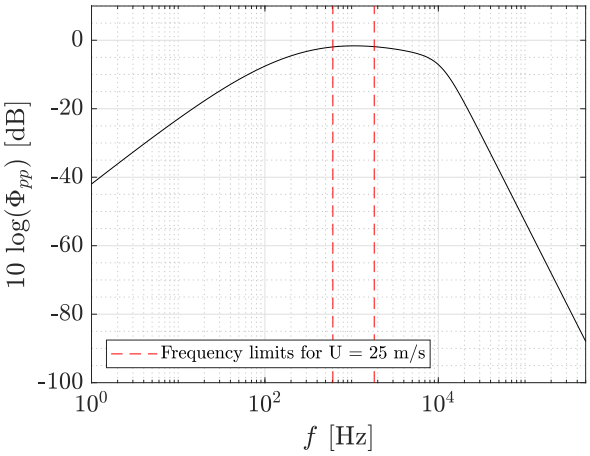

Figure 4.4: Frequency limits (indicated by dashed lines) according to Eq. 4.7. Pressure spectral density based on Goody's model for the flow conditions $U = 25\,\mathrm{m\,s^{-1}}$ and $T = 20\,°\mathrm{C}$.

Property	Assumed values
Elastic modulus	$E = 0.1 \ldots 1\,\mathrm{MPa}$
Material density	$\rho = 1000\,\mathrm{kg\,m^{-3}}$
Poisson's ratio	$\sigma = 0.5$
Kinematic viscosity	$\nu = 1.5064 \times 10^{-5}\,\mathrm{m^2\,s^{-1}}$

Table 4.1: Assumptions for calculating the interaction of turbulent flow structures with coating surface motions.

The analysis of compliant material effects shows that dissipation of turbulent energy in the viscoelastic polymer can be neglected. The surface motion of a compliant coating can lead to reduction of turbulence intensities even for stiff materials subject to air flow. However, this combination requires thick coating layers, high flow speeds and smooth surfaces. The review of literature in the field of compliant wall coatings reveals that most studies focus on soft, gel-like materials subject to water flows. For this combination, relative strong material waves develop. Nevertheless, even for underwater applications, results of drag reduction are controversially discussed and repeatability of such experiments is generally low. No interactions between wall pressure fluctuations and a coated, metallic foam are expected. The thickness of the stiff coating is too low and not sufficiently smooth. The irregular surface structure and inhomogeneities in the coating thickness are expected to prevent the occurrence of mechanical surface wave patterns.

4.3. Experimental Characterization of Coating Properties

In order to achieve active pore size change, the 1200 µm metal foam was covered with a polymer in the form of a liquid rubber spray from the company Plasti Dip as illustrated in Figure 4.1. In advance, rubber sprays from different manufacturers were applied to metal foam samples in order to identify the optimum consistency and curing time. Among the tested sprays, Plasti Dip performed best.

The coating material properties were required for investigating possible flow compliance and achievable pore size changes. The modulus of Plasti Dip was obtained from a Dynamic Mechanical Analysis (DMA). Thin test samples with a thickness of 0.2 mm were produced by spraying several layers of coating material on Teflon plates. At room temperature, a modulus of $E \approx 0.1\,\mathrm{MPa}$ was measured. Material inhomogeneities, such as small enclosed air bubbles, could explain the low value which did not allow for DMA measurements

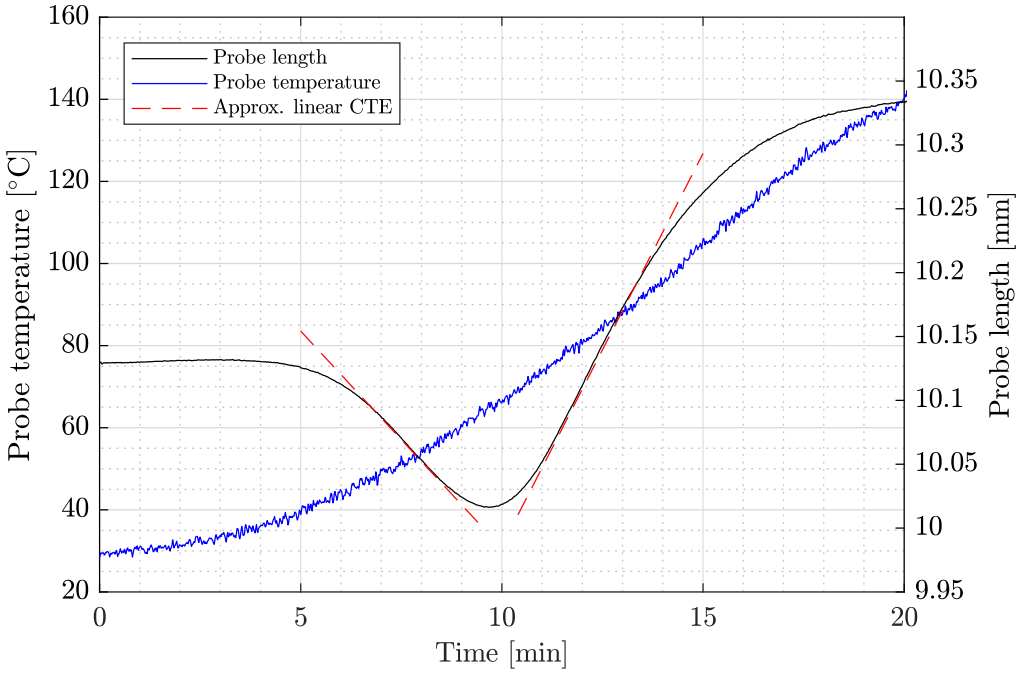

Figure 4.5: TMA results of the material Plasti Dip in the form of probe length and temperature as a function of the program time. The two regions with quasi-linear coefficients of thermal expansion are indicated by red dashed lines.

above room temperature. Given the limitations of the measurement device and insufficient sample quality, the result at ambient temperature is not representative for a thicker coating layer.

The thermal expansion coefficient of the coating material determines the achievable pore size change upon heating. In order to specify α_v, a Thermomechanical Analysis (TMA) of a thin film sample of Plasti Dip was carried out, using a Diamond TMA system of the company Perkin Elmer. A static force of 5 mN was applied to the sample with dimensions 0.21 mm (thickness), 2.75 mm (width) and 10.26 mm (length). Starting from ambient conditions, the sample temperature was increased at a rate of 10 °C/min up to 180 °C. Figure 4.5 shows the sample length and sample temperature as a function of time. Due to the thermal inertia of the material, the highest achievable sample temperature was around 150 °C. The plot indicates two regions where both, temperature and material expansion changed linearly with time. In the temperature range between 40 °C and 65 °C, a negative linear thermal expansion of $\alpha_l = -6.41 \times 10^{-4}\,\mathrm{K}^{-1}$ was observed. For temperatures above 70 °C, a linear expansion of $\alpha_l = 8.45 \times 10^{-4}\,\mathrm{K}^{-1}$ was found.

Three layers of liquid rubber were applied to the TE inserts manufactured from the 1200 µm metal foam from both sides. For reasons of comparability in terms of the noise mitigation characteristics, the permeability of the coated foam was intended to match the properties of the 800 µm foam. Subsequent to every layer of coating, compressed air was used to increase the penetration of the liquid rubber into the metal foam and to prevent the closure of individual pores.

The achievable pore size change upon heating was determined experimentally by using microscopic images of the pore sizes. The temperature of a coated metal foam sample was increased up to 169 °C through electric heating wires and a type-K thermocouple was used for monitoring the surface temperature of the sample. When steady-state conditions were reached, a sequence of images was acquired using a digital Nikon D80 camera equipped with an AF Micro Nikkor 200 mm lens. The optical setup resulted in a magnification factor of $M = 1$ with a resolution of 3872 X 2592 pixels. During the post-processing, congruent images at ambient and maximum temperature were compared and the changes in pore diameter were measured at different surface locations.

The pore size change resulting from a temperature difference of $\Delta T = 151\,°\mathrm{C}$ is listed in Table 4.2 for four different surface locations. For pore sizes $d_{p,a}$ between 200 µm and 400 µm at ambient temperature, the average diameter decreased by up to 21 µm upon heating. Figure 4.6 depicts the four measurement locations on the surface of the heated porous material. A magnification of location 1 is provided together with the pore diameters in vertical and horizontal directions for both surface temperatures.

From the results in Table 4.2 it can be inferred that the pore size change strongly depends on the mea-

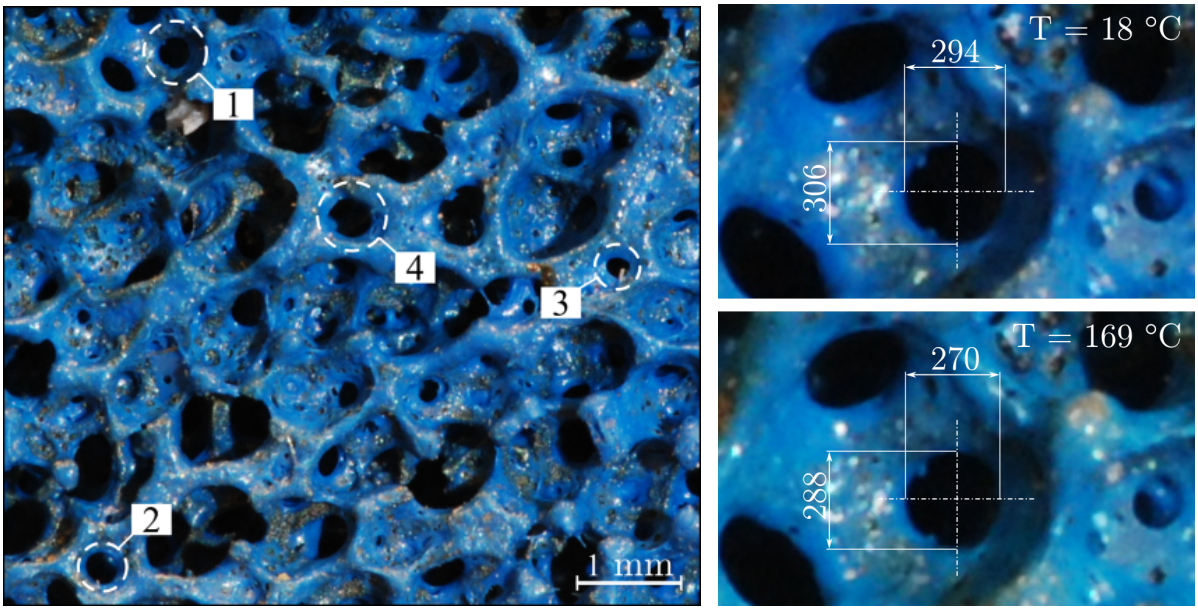

Figure 4.6: Microscopic image of coated metal foam. On the left-hand side, the positions used for calculation of the achieved pore size change are depicted. On the right-hand side, an enlarged visualization of position 1 for two different temperatures, including horizontal and vertical diameters of the pore, is given. Measures are given in µm unless otherwise specified.

surement location. Due to the irregular microscopic structure of the metal foam and as a result of the coating technique, the coating layer thickness varied for individual pores. In Figure 4.6, the irregularly distributed polymeric coating is visible. Taking the average pore size at ambient conditions as the reference value, the diameter change upon heating lay between 2 % and 9 % for the four locations considered in the post-processing. Microscopic images of the uncoated metal foam confirmed that thermal expansion of the metallic structure did not contribute to the observed pore size changes. However, a slight displacement of the field of view for identical camera positions implies that macroscopic expansion of the porous metal sample occurred.

For validation of the results, the theoretical pore size change of a coated metal foam, subject to the same temperature increase as during the experiment, was obtained from Eq. 4.2 and Eq. 4.3. It is assumed that applying the coating material shrank the original pore size of $d_{p,0} = 1200\,\mu\text{m}$ down to $d_{p,a} = 800\,\mu\text{m}$. For isotropic coating material behavior, the volumetric thermal expansion coefficient α_v equals $3\alpha_l$. Taking the region with negative thermal expansion into account, an effective pore size reduction of $\Delta d_p = 40\,\mu\text{m}$ would be expected.

Compared to the theoretical analysis of achievable pore size change, the measured values are lower. The idealized assumptions, such as the torus-shaped pores and homogeneously applied coating, leads to a larger polymeric material volume which can expand with increasing temperature. The limiting factors for pore size change upon heating were defined as the coating volume, the maximum temperature and the thermal expansion coefficient of the coating material. Given the material properties, these limits were reached in the current experiment. The maximum temperature lay within the melting region of the polymer and from the microscopic images it was inferred that additional coating layers would have sealed individual pores. The conclusion drawn from the experiment is that active pore size change due to heating of polymeric coating affects the porosity of the metal foam. However, with respect to the nominal pore size of the foam, the achievable change is relatively small. The effects on TBL-TE noise generation are discussed in Sec. 5.5.4.

Position		$d_{p,a}$ at $T = 18\,°C$ [µm]	$d_{p,h}$ at $T = 169\,°C$ [µm]	Δd_p [µm]
1	hor.	294	270	24
	ver.	306	288	18
	avg.	300	279	**21**
2	hor.	291	274	17
	ver.	302	289	13
	avg.	297	281	**15**
3	hor.	221	197	24
	ver.	191	178	13
	avg.	206	188	**19**
4	hor.	422	411	11
	ver.	367	360	7
	avg.	394	385	**9**

Table 4.2: Change of pore size Δd_p upon heating at 4 different locations (Figure 4.6). At every position, the horizontal and vertical diameter of the pores was measured for two different surface temperatures.

5

Aeroacoustics of Heated Trailing Edges

From the previous analysis of heating effects on flow resistivity and permeability, several potential activation mechanisms, with partly opposing effects on noise mitigation, were identified. In the present chapter, the effects of TE heating on radiated far-field noise levels are determined by means of aeroacoustic measurements in an anechoic wind tunnel. Noise characteristics of heated and unheated TE inserts are presented and the quality of the acoustic results is assessed. The main objective is to identify the dominant activation mechanisms by including the results from the previous chapters.

5.1. Experimental Setup

An overview over the experimental setup in the wind tunnel and important measures are illustrated in Figure 5.1. The main components of the setup, namely the flow facility, the acoustic array and the heating setup, are described in the following.

5.1.1. Wind Tunnel and Airfoil Model

Acoustic measurements were carried out in the anechoic wind tunnel of Delft University of Technology (A-Tunnel). The vertical, open-jet wind tunnel can provide flow velocities up to $42\,\mathrm{m\,s^{-1}}$ with the contraction used in this campaign. The size of the rectangular contraction outlet is 40 x 70 cm^2. TBL-TE noise was evaluated for a NACA0018 airfoil with chord length $c = 20\,\mathrm{cm}$. An interchangeable TE with a length of $0.2c = 4\,\mathrm{cm}$ allowed for the use of different solid and porous inserts. The airfoil was placed between two wooden side plates with a height of 1.2 m and a distance between the contraction outlet and the leading edge of 0.5 m. All experiments were carried out for a geometrical angle of attack of 0° which was adjusted based on a digital inclination measuring device.

Experiments in the vertical wind tunnel were performed at two different flow speeds $U = 15\,\mathrm{m\,s^{-1}}$ and $U = 25\,\mathrm{m\,s^{-1}}$. For the given airfoil setup and flow conditions, these flow speeds refer to chord-based Reynolds numbers of $Re_1 = 1.88 \times 10^5$ and $Re_2 = 3.14 \times 10^5$, respectively. To ensure turbulent flow past the TE, transition was forced at $x/c = 0.2$ using carborundum grains with a diameter of 0.84 mm. Turbulent state of the boundary layer was verified by placing an external microphone at different span- and streamwise locations close to the airfoil surface.

A solid TE insert as well as two porous TEs made from metal foams with pore sizes of 800 µm and 1200 µm were used during the experimental campaign. The porous inserts were manufactured through spark erosion (EDM) machining. Each porous TE was composed out of three individual pieces with spanwise dimensions 13 cm (2x) and 14 cm (1x). Figure 5.2 shows the geometry of the TE inserts and gives an overview over the different porous versions that were tested beside the solid reference TE.

5.1.2. Acoustic Measurements

For quantification of the emitted TBL-TE noise from different TE configurations, a phased microphone array was used. Instead of measuring the far-field noise spectrum with a single microphone, a phased array provides information about the locations of noise sources and their intensities. In this way, the TE as a noise source can be isolated from interfering background noise sources. The acoustic array consisted of 64 G.R.A.S. 40PH free-field microphones with built-in preamplifiers. The microphones were distributed according to a

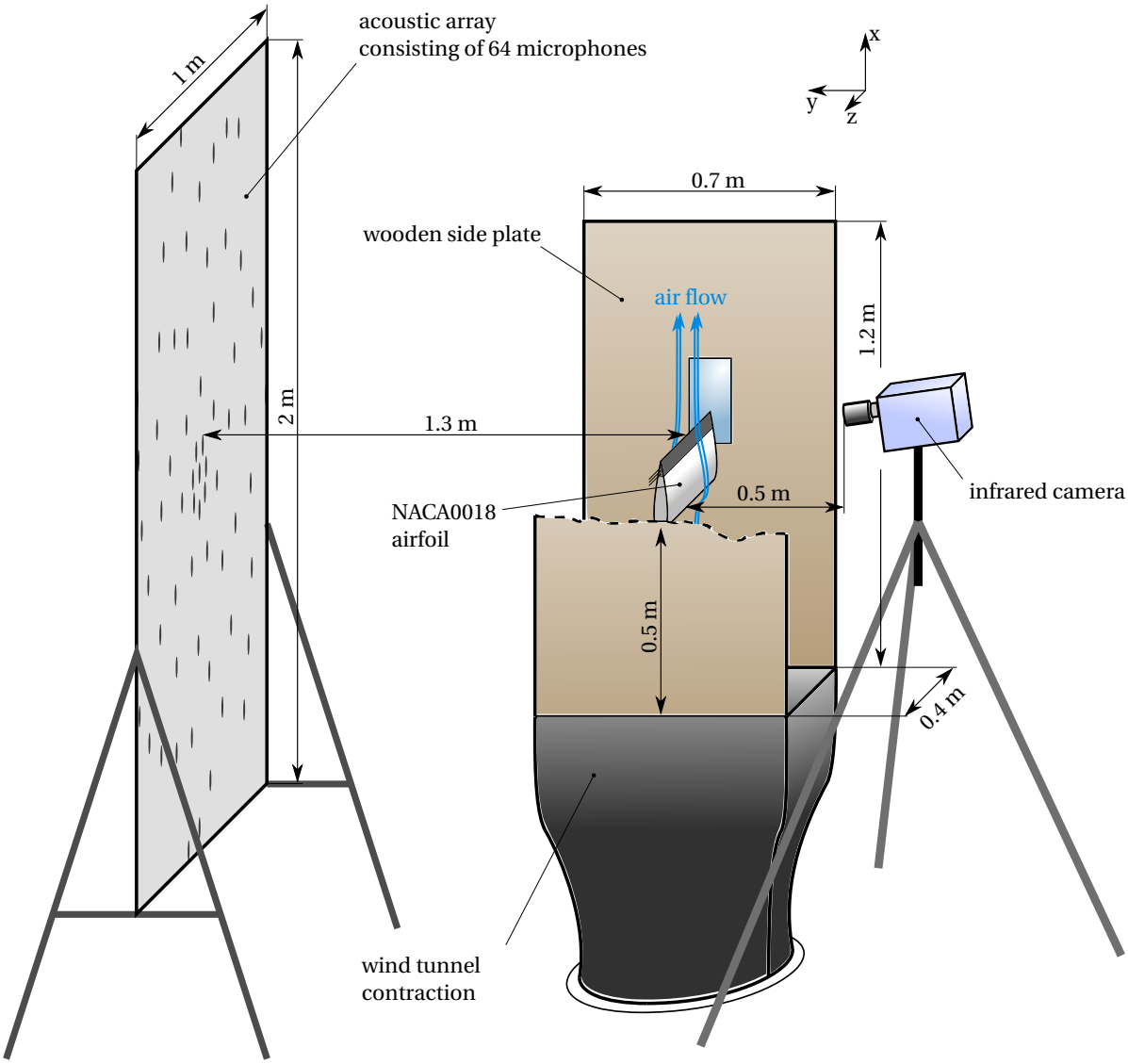

Figure 5.1: Main components of experimental setup for measuring noise characteristics from various TE inserts. The experiments were conducted in the vertical, anechoic wind tunnel at TU Delft.

variation of Underbrink's design [80] consisting of seven logarithmic spiral arms and one microphone in the center. The array was located 1.3 m away from the airfoil plane. Given this distance, the test section side plates restricted the width of the acoustic array. Microphones which were located too far from the array center could not detect the noise emitted by the TE. For this reason, and without compromising resolution in vertical direction, the Underbrink design was stretched. The microphones were spread across a 1 m wide and 2 m high plane and the array layout is illustrated in Figure 5.3.

5.1.3. Heating Setup

The experimental campaign mainly focused on the effects of temperature changes on porous TEs and their noise mitigation capabilities. For temperature control, the porous TE inserts were equipped with electrical heating wires. A total of 12 heating wires, with an outer diameter of 1.1 mm each, were aligned in the spanwise direction and distributed across the TE cross-section according to Figure 5.4. The feed-through in the tunnel side plates was sealed by using high-temperature resistant Kapton tape. Each individual heating wire consisted of a conductive inner wire with a diameter of 0.6 mm, covered with an electrical insulation. The core was manufactured out of a copper-nickel alloy (CuNi44) with a high length-specific electrical resistance of $R_s = 1.73\,\Omega\,\mathrm{m}^{-1}$. Insulation from the metallic foam was required due to the high electrical conductivity of the porous metal foam. For insulation, a polymeric (PVDF), high-temperature shrinking tube was used. The

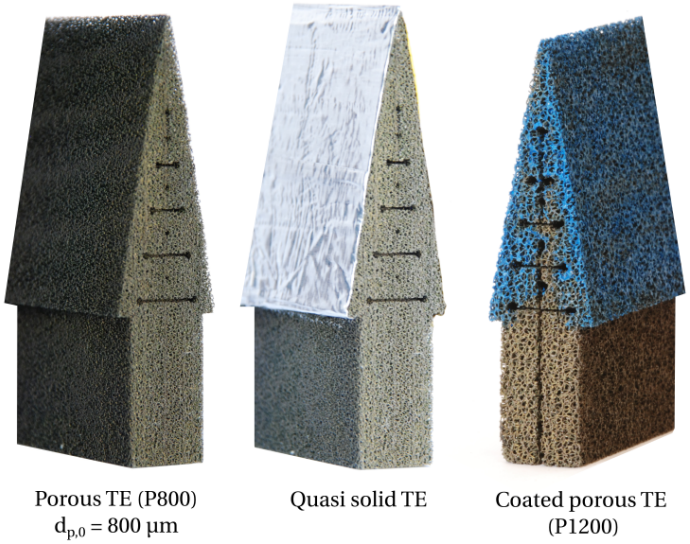

Figure 5.2: Different TE inserts used during the experimental campaign

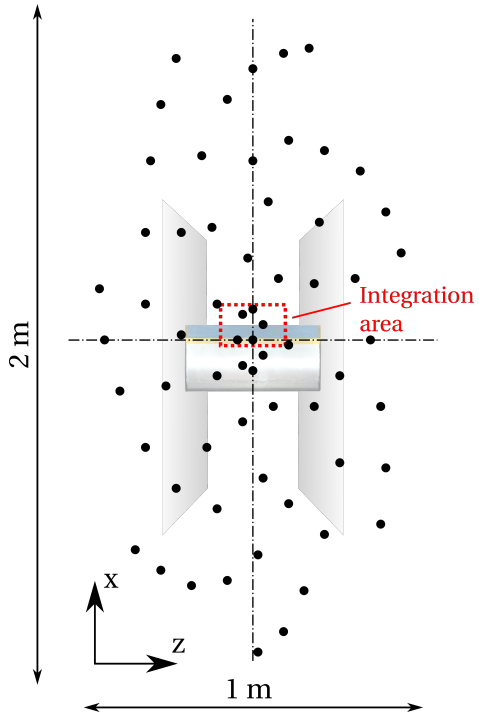

Figure 5.3: Microphone distribution and location of array relative to airfoil and integration area. Components are drawn to scale.

nominal operating temperature limit was 175 °C; however, heating tests indicated that for short time periods, the insulation material could withstand temperatures up to 300 °C without melting.

The heating wire temperature is a function of the electric current I which flows through the wire. The voltage V required to overcome a given resistance R follows from Ohm's law $V = RI$. Together with the well-known definition of electric power $P_{el} = VI$ it follows that the power dissipation due to the resistance in the electric circuit is a quadratic function of the current

$$P_{diss} = RI^2 \,. \tag{5.1}$$

The power is dissipated in form of heat which was the desired output in the case of this experimental setup. The resistance of a single wire spanning the entire TE width of 0.4 m amounted to $R_w = 0.4R_s = 0.69\,\Omega$. In order to restrict the voltage, the heating wires were hooked up in pairs which cut the resistance of the system in half. Considering the total amount of 6 heating wire pairs and a current of $I = 10$ A, the available heating power resulted in $P_{el} \approx 210$ W. The overall resistance of the heating system, including the heating wire connections, amounted to $R_{\text{sys}} = 4.1\,\Omega$. A power supply which could provide a maximum voltage of 50 V and a maximum current of 10 A was used for the experiments.

The surface temperature of the TE was analyzed using a CEDIP Titanium 530L IR infrared camera with a resolution of 320 x 256 pixels. To avoid interactions with the open-jet air flow, the distance between the infrared camera and the TE was 0.5 m. The camera lens was inclined such that it was positioned perpendicular to the TE surface. Due to the emitted noise from the camera cooling system, the surface temperature distribution could not be recorded simultaneously to the acoustic measurements. Assuming steady flow conditions and a constant electrical power supply, infrared images were taken prior to the microphone recording for every test case. The heating wire temperature was measured using a type-K thermocouple placed inside the porous material close to the wire surface (see Figure 5.4).

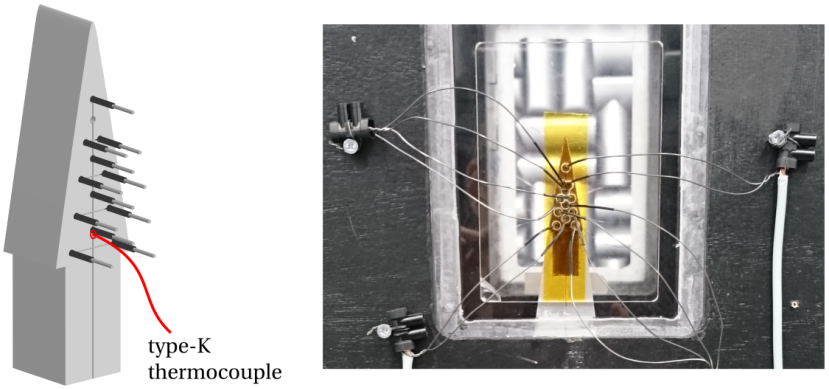

Figure 5.4: CAD model showing the layout of the 12 heating wires and the location of the thermocouple (left). Pairs of heating wires were connected in series and gap between tunnel side wall and airfoil was sealed with Kapton tape (right).

5.2. Beamforming Algorithm

The microphone array measurements were processed by using a conventional frequency-domain beamforming algorithm developed by the Aircraft Noise and Climate Effects (ANCE) department of TU Delft. For far-field spectra of TBL-TE noise, the method of Source Power Integration was applied.

For each test configuration, the microphone recording time was 60 s at a sampling frequency of 50 kHz. The raw signals were split into time windows of $\Delta t = 0.1$ s which resulted in a frequency resolution of $\Delta f = 10$ Hz. The data in every time window were weighted using a Hann function and a window overlap of 50 % was chosen.

A Fourier transform was applied to the time domain sound pressure levels of every microphone in order to determine the complex pressure amplitudes $p(f)$ as a function of frequency. For each of the 1199 windows, the spectral densities of the 64 microphones were linked by calculating the Cross Spectral Matrix $CSM_k = 0.5 p(f_k) p(f_k)^*$ for a certain frequency f_k of interest. Results from the individual windows were averaged in order to obtain a single CSM for every frequency. The frequency range of interest was determined upon reviewing the source maps as well as the signal-to-noise-ratio of the TE noise and the background noise. For the given experimental setup, the range $f_{\min} = 500$ Hz up to $f_{\max} = 5000$ Hz was chosen during the post-processing.

A conventional delay-and-sum beamforming method in the frequency domain [81] was used to obtain the noise source location and strength in the airfoil aligned scan plane of interest. The dimensions of the scan plane amounted to 2 m in height and 1 m in width with a resolution of 0.01 m. The frequency-dependent resolution of the acoustic camera follows from Rayleigh's limit which can be written as [82]

$$\Delta x = l \tan\left(1.22 \frac{c_0}{f D}\right), \tag{5.2}$$

where Δx is the smallest resolvable length scale, l is the distance between the array and the scan plane, c_0 is the speed of sound and D is the diameter of the circular array. For the highest frequency of interest $f_{\max} = 5000$ Hz and under the assumption of $D = 2$ m in the vertical direction, a minimum value of $\Delta x_{min} = 0.05$ m results. It can be concluded that the discretization of the scan plane is fine enough with regard to the achievable array resolution.

For every scan grid point j, a frequency-specific steering vector $\vec{g}_j(f_k) = (g_{j,1}(f_k), g_{j,2}(f_k), ..., g_{j,n}(f_k))^T$ was constructed. The index n refers to the number of microphones and the steering vector components are defined as

$$g_{j,n} = \frac{\exp(-2\pi i f_k \Delta t_{j,n})}{4\pi \left\| \vec{r}_{j,n} \right\|^2}. \tag{5.3}$$

The expression of $g_{j,n}$ represents the received signal of microphone n emitted from a modeled monopole source (ideal point source) located in the scan plane at point j. The time delay of the signal is denoted with $\Delta t_{j,n}$ while the vector from a scan grid point to a specific microphone is $\vec{r}_{j,n}$. The corresponding amplitudes of the steering vectors $\vec{g}_j$ are obtained in the form of the source autopowers A_j by minimizing the difference between the recorded and modeled pressure data.

In quiescent air, the time delay Δt_j in Eq. 5.3 directly follows from the speed of sound c_0 and the distance between scan point and receiver $\left\| \vec{r_{j,n}} \right\|$. If the propagation path of the emitted sound waves is affected by uniform air flow with Mach number $\vec{M}$, the corrected time delay follows from

$$\Delta t = \frac{1}{c\beta^2} \left(-\vec{M} \cdot \vec{r} + \sqrt{\left(\vec{M} \cdot \vec{r}\right)^2 + \beta^2 \left\| \vec{r} \right\|^2} \right) \tag{5.4}$$

where $\beta^2 = 1 - \left\| \vec{M} \right\|^2$. For measurements in open-section wind tunnels, where the microphone array is located outside the flow, the emitted sound waves pass regions with different air speeds as well as the non-uniform shear layer. As suggested by Sijtsma [83], the uniform Mach number in Eq. 5.4 can be replaced by an effective Mach number

$$M_{x,eff} = M_x \frac{y_{sl}}{y} \, . \tag{5.5}$$

The relation is given for noise propagation in the y-direction perpendicular to the vertical component of the Mach number M_x. For the distance $y = 1.3\,\mathrm{m}$ between scan plane and array, a shear layer distance of $y_{sl} = 0.5$ proved to be appropriate. For the given experimental setup, this value resulted in a flow speed independent position of the main noise source.

The beamforming results were further used to obtain the spectrum of TBL-TE noise emitted by the airfoil. The method of Source Power Integration (SPI) was applied with the intention to isolate TBL-TE noise from background sources such as noise from interactions between the flow and the test section side plates. For SPI, an integration area in the scan plane was defined according to Figure 5.3. Centered around the TE, the integration area extended 0.13 m in streamwise direction and 0.2 m in spanwise direction. The integration area should include the complete main lobe of TBL-TE noise for the whole frequency range of interest while excluding side lobes and contributions from other noise sources. For every frequency, the experimentally obtained source powers $A_{j,exp}$ were summed up within the integration area. The integrated source power of the experiment P_{exp} was obtained by applying a correction factor to the sum of the $A_{j,exp}$ within the area of interest [84]

$$P_{exp} = \frac{P_{sim}}{\sum_{j=1}^{J} A_{j,sim}} \sum_{j=1}^{J} A_{j,exp} \, . \tag{5.6}$$

The scaling factor was determined by applying beamforming to a simulated point source in the center of the integration area with sound power P_{sim} (typically chosen to be 1). Finally, the ratio between P_{sim} and the integrated $A_{j,sim}$ was multiplied with the experimental data. From the corrected, integrated source powers, the SPLs at a distance of 1 m from the scan plane were calculated according to Eq. 5.8.

The strength of noise sources within the scan plane was quantified in the form of Sound Pressure Levels (SPL) which logarithmically express the ratio between the effective sound pressure p_e and a reference sound pressure $p_0 = 2 \times 10^{-5}\,\mathrm{Pa}$

$$\mathrm{SPL} = 10 \log_{10} \frac{p_e^2}{p_0^2} \, . \tag{5.7}$$

For visualization of the beamforming results, the source autopowers A_j were converted into SPLs as received at a distance r from the scan plane

$$\mathrm{SPL}_j = 20 \log_{10} \frac{\sqrt{A_j}}{r\, p_0} \, . \tag{5.8}$$

For the results presented in the following, a reference distance of $r = 1\,\mathrm{m}$ was chosen.

The spectral information of noise measurements is commonly expressed through the energy content of a signal within a certain frequency band. The energy level and spectral resolution depends on the chosen bandwidth. For a constant-bandwidth analysis, energy contributions are summed up over constant frequency intervals Δf centered around f_c. The use of larger bandwidths with increasing frequency is referred to as constant percentage bandwidth analysis. The center frequency of constant percentage bands is obtained from $f_c = \sqrt{f_u f_l}$, where f_l and f_u refer to the lower and upper bound of the bands, respectively. In the following, use is made of 1/3-octave bands (tertsbands) with standardized center frequencies that can be approximately calculated from

$$f_c = 10^{n/10} \, , \tag{5.9}$$

where n is the band number.

The recorded microphone data were discretized by calculating the CSM for specific frequencies f_k. The components of the individual CSM_k represented the energy content of the signals within bands of constant

width $\Delta f = 10\,\text{Hz}$. Therefore, SPLs obtained from beamforming and source power integration can be interpreted as Pressure Band Levels (PBL) which contain the energy of 10 Hz bands. Summation of multiple band levels led to the PBL of 1/3-octave bands which are denoted with $\text{SPL}_{1/3}$ in the following. Note that the connecting lines between discrete band levels plotted over f_c do not represent the actual SPL distribution within the bands but only serve the purpose of visualization.

5.3. Evaluation of Beamforming Results

The sensitivity of microphone array measurements with respect to the location and size of the integration area is assessed in the following. Furthermore, the quality of the results is evaluated based on background noise levels and based on the repeatability of measurements.

5.3.1. Integration Area

Radiated far-field noise spectra of different TE configurations were obtained from Source Power Integration. Since TBL-TE noise is the airfoil self-noise source of interest, the integration area needs to capture the noise emitted from the TE region while excluding background noise sources. In Figure 5.5, noise sources within the 1/3-octave band centered around $f_c = 1.6\,\text{kHz}$ are plotted for a solid and porous TE, respectively. Source noise levels are given in SPLs as observed at a distance of $r = 1\,\text{m}$ from the airfoil plane. The streamwise location of the source peak was determined from the maximum SPL along the centerline ($z = 0$) of the airfoil. In the solid reference case, the source location coincided with the TE location for both tested flow speeds. The result confirms that the appropriate shear correction was applied to the steering vector.

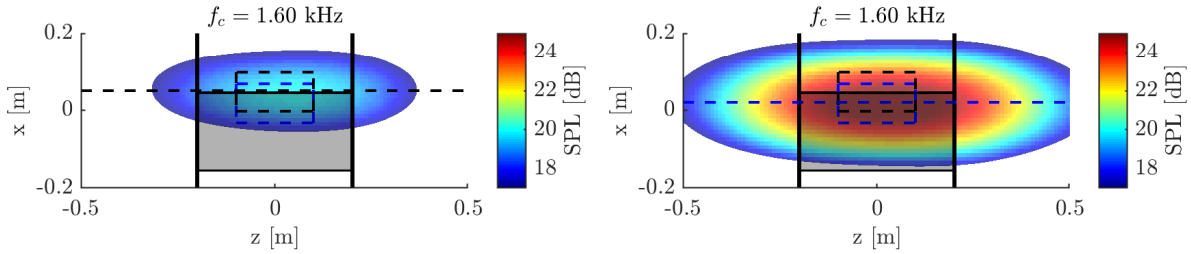

Figure 5.5: Source maps of 1/3-octave bands centered around f_c for solid TE (a) and porous TE (b) at a flow speed of $U = 15\,\text{m s}^{-1}$. Horizontal dashed lines indicate maximum noise source locations. Squares centered around the TE (dashed black) and upstream of the TE (dashed blue) illustrate integration areas.

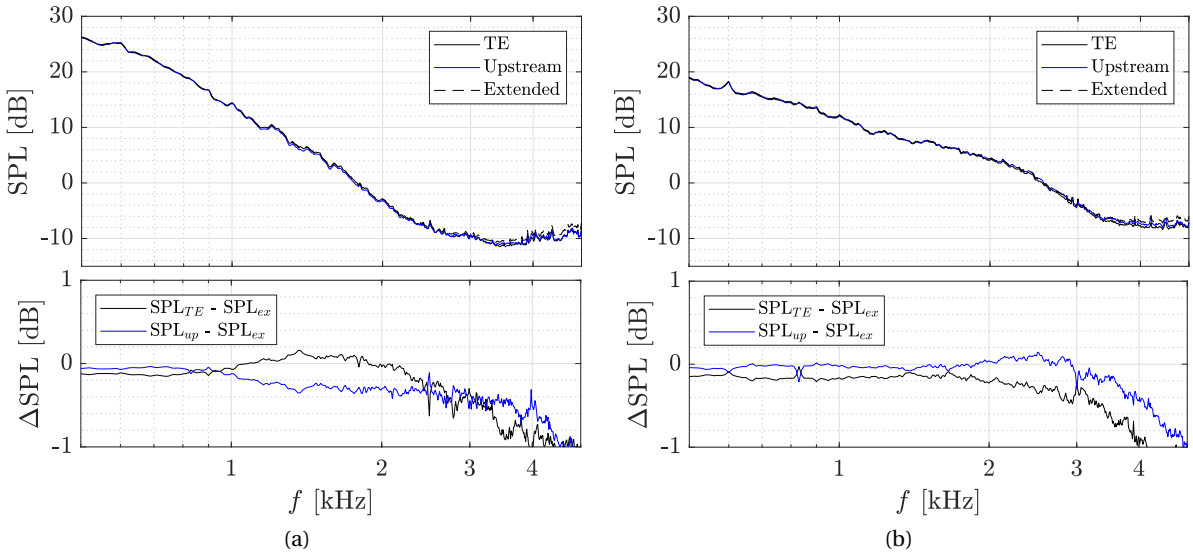

Figure 5.6: Far-field noise spectra obtained from source power integration over different areas for a solid (a) and porous (b) TE at $U = 15\,\text{m s}^{-1}$. Corresponding integration locations are depicted in Figure 5.5.

An upstream shift of approximately $0.015c$ (3 cm) with respect to the TE was observed in the porous case. The main noise source was therefore located in proximity to the permeable-impermeable junction. This observation agrees with an analytical study of Kisil and Ayton [30] who predicted noise generation at the junction between the solid and porous material in addition to scattering at the TE.

The use of a fixed integration area for all test cases required a sensitivity analysis of the noise results with respect to changes in the streamwise location and size of the integration area. The chosen locations are indicated by black and blue dashed lines in Figure 5.5. Both integration areas were centered around the maximum noise source location of the solid and porous TE. A streamwise length of $0.25c$ was chosen for both areas based upon the extension of the main lobe. Additionally, a third region, incorporating both areas, was defined. The integration areas with a spanwise length of $0.5c$ were aligned with the airfoil centerline ($z = 0$). Figure 5.6 shows a comparison between resulting spectra in a frequency range between 0.5 kHz and 5 kHz. The SPL represent the energy content within 10 Hz bands. Slightly higher SPLs resulted in the cases where the integration area matched to the TE configuration. For frequencies up to approximately 3 kHz, an enlarged integration area did not alter the characteristics of the noise spectra considerably and it was therefore used for all TE configurations treated in this report.

5.3.2. Background Noise

Background noise sources in wind tunnels affect the quality of acoustic measurements especially when emitted noise levels of interest are low, such as it is the case for experiments on TBL-TE noise reduction. In background noise spectra from the A-Tunnel facility of TU-Delft, Roberto Merino-Martínez [85] found tonal noise contributions from the wind tunnel fan and its control unit as well as from interactions between flow and wind tunnel nozzle. For a low flow speed of $U = 15\,\mathrm{m\,s^{-1}}$, the SPLs resulting from TBL-TE noise were relatively low compared to background noise sources. Figure 5.7 shows the wind tunnel background noise in the absence of the test section compared to noise spectra from a solid and porous TE for matching flow speeds. The plotted noise spectra were obtained from a single array microphone, located at the same height as the TE. Background noise levels were recorded at a distance of 1.43 m away from the center of the wind tunnel contraction while the array was placed slightly closer to the tunnel (1.3 m) during the experimental campaign. Comparability of the results is still provided since it can be assumed that background noise levels are relatively insensitive to the array position due to the absence of strong noise sources directly in front of the array. Furthermore, the noise levels of the tonal peaks agreed for all measurements. The signal-to-noise-ratio (SNR), defined as the difference between the measured SPL and the background noise level, was higher for low frequencies except for distinct tonal peaks. SNRs based on single microphone measurements can be used to quantify the increase in noise levels due to the presence of the test section and the airfoil model.

The beamforming algorithm in combination with SPI can be used to distinguish between TBL-TE noise and other airfoil self-noise sources or background noise. The quality of the noise measurements should therefore be assessed based on the source maps instead of relying on the SNR. SPI was only performed for frequency bands which showed a clear source maximum in the TE region. Figure 5.8 depicts source maps of the limiting frequency bands for the solid and porous TE at $U = 15\,\mathrm{m\,s^{-1}}$. Below the 1/3-octave band centered around $f_c = 0.63$ kHz, TBL-TE noise could not be distinguished from other airfoil noise sources due

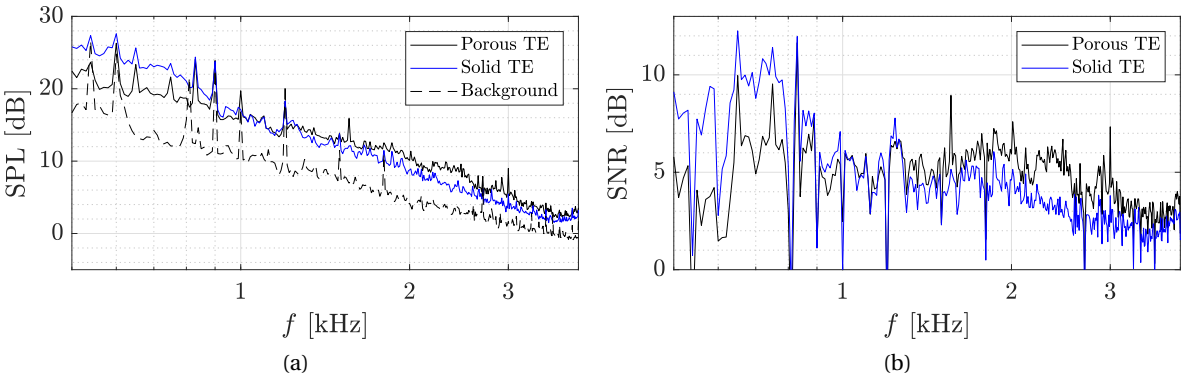

Figure 5.7: Spectral noise levels of empty wind tunnel (background) and noise levels of installed model with solid and porous TE at $U = 15\,\mathrm{m\,s^{-1}}$ (a). The sound pressure was recorded with a single microphone at a distance of 1.3 m from the TE, measured perpendicular to the airfoil chord. The SNR (b) represents the difference between noise from the installed airfoil setup and background noise.

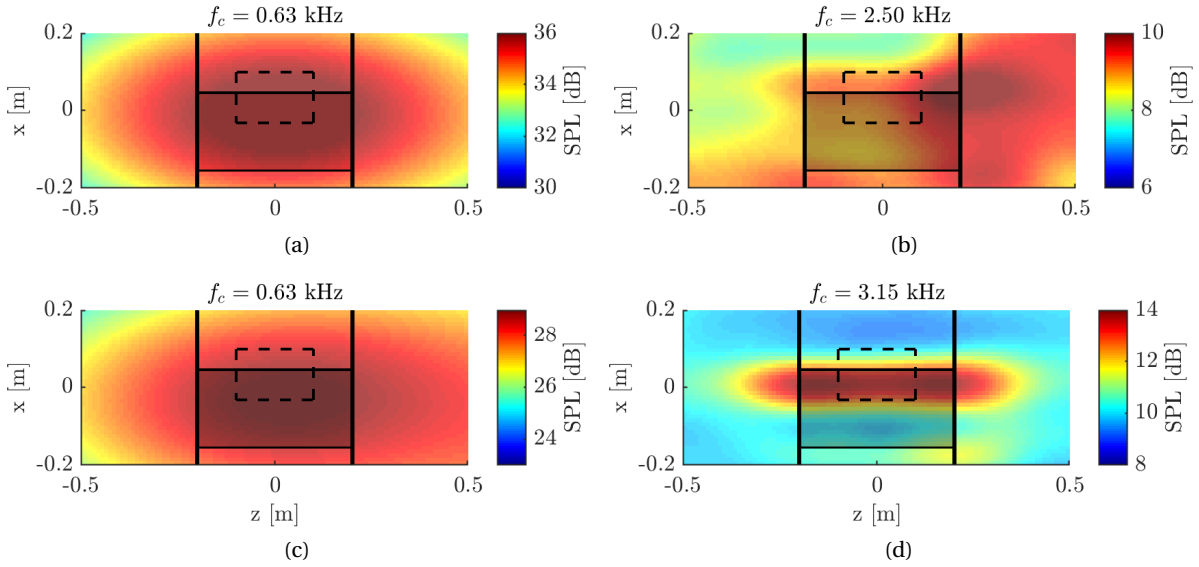

Figure 5.8: Source maps for minimum (a),(c) and maximum (b),(d) considered 1/3-octave bands centered around f_c. Source levels correspond to a flow speed of $U = 15\,\mathrm{m\,s^{-1}}$ for the solid (a),(b) and the porous (c),(d) TE.

to decreasing array resolution. An upper limit had to be defined since TBL-TE noise contributions were in the order of background noise levels for sufficiently high frequencies. For low frequencies, noise mitigation through porous TEs was effective. This agrees well with previous experimental studies [32–34] where high-frequency excess noise was attributed to the surface roughness of porous materials. With increasing flow speed $U = 25\,\mathrm{m\,s^{-1}}$, TBL-TE noise became dominant over background noise sources even for the frequency band centered around $f_c = 4\,\mathrm{kHz}$.

Noise spectra for 1/3-octave bands up to $f_c = 3.15\,\mathrm{kHz}$ are plotted in the following. Up to this frequency, the source plots indicated clear TBL-TE noise contributions and errors due to the choice of integration area were expected to be below 1 dB. Due to low noise levels, spectra of the solid TE at $U = 15\,\mathrm{m\,s^{-1}}$ were only plotted up to $f_c = 2.5\,\mathrm{kHz}$.

5.3.3. Repeatability

The repeatability of far-field noise measurements depends on ambient conditions such as fluctuations in flow velocity, ambient pressure or temperature. Furthermore, changing background noise levels could affect the beamforming results. In an effort to assess the influence of random error sources, recording of the porous TE noise spectra was repeated five times. The maximum observed differences between the five runs are plotted in Figure 5.9 for different test configurations. For constant 10 Hz bands, variations between the spectral levels were less than 1.5 dB while for 1/3-octave bands, the differences were reduced to < 0.25 dB due to the averaging of energy content from a larger frequency range. Largest deviations were observed in the high-frequency regime and for a low flow speed i.e. in the domain where background noise was dominant over TBL-TE noise.

Far-field noise measurements of heated and unheated cases were acquired alternating which implied that a time span of roughly 15 min lay in between repetitions of the same configuration. Despite this time interval and changing wind tunnel settings, acoustic measurements were repeatable and it is concluded that for the considered frequency regions in this report, random errors in 1/3-octave band levels of less than 0.25 dB can be expected. Moreover, it is argued that the activation through heating provided reproducible results and that no permanent geometrical changes remained when the inserts were cooled down.

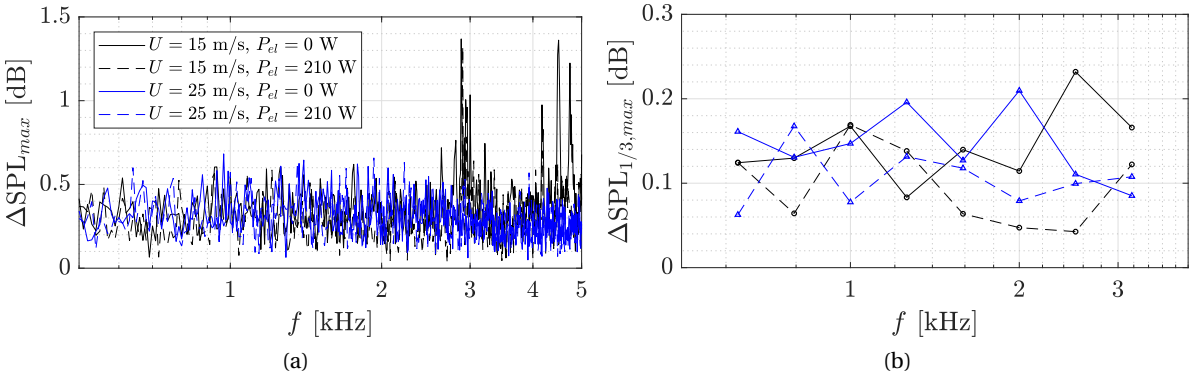

(a) (b)

Figure 5.9: Maximum absolute differences between noise spectra from five repetitions. Spectra are plotted for constant band widths of 10 Hz (a) as well as for 1/3-octave bands (b).

5.4. Heated Solid Trailing Edges

The development of a thermal boundary layer above a heated surface possibly affects the magnitude of wall pressure fluctuations (Sec. 2.4). Effects of a heated TE surface on TBL-TE noise radiation were investigated by using the porous TE with installed heating wires and sealed surfaces.

First, the influence of sealing pressure and suction sides of the porous TE with aluminum tape was evaluated by comparing its far-field noise to the solid reference TE. Figure 5.10 depicts the measured noise spectra for two flow speeds. The slope of the quasi-solid spectra is slightly steeper than for the reference case. It is assumed that geometrical changes due to the additional aluminum tape layer influenced the noise generation mechanism slightly; however, deviations from the reference TE stayed below 1.5 dB.

For the two different flow speeds, the achievable wall temperature of the quasi-solid TE is shown in Figure 5.11. The electrical power input of $P_{el} = 210$ W resulted in maximum surface temperatures of 80 °C and 70 °C for $U = 15\,\mathrm{m\,s^{-1}}$ and $U = 25\,\mathrm{m\,s^{-1}}$, respectively. Lower temperatures were observed in the root and tip region of the TE because of the heating wire layout. Far-field noise spectra of the heated TE cases are included in Figure 5.10. Only marginal offsets from the quasi-solid TE at ambient conditions (< 0.4 dB) were observed.

Antonia et al. [86] experimentally studied the development of a thermal boundary layer beneath an existing turbulent boundary layer initiated by a step change in surface heat flux. In agreement with previous work they found that the thermal boundary layer thickness δ_t grows in the streamwise direction x according to $\delta_t \propto x^{0.8}$. They concluded that fully developed thermal conditions were reached approximately $100\delta_0$ downstream of the surface heat flux jump. The turbulent boundary layer thickness at the TE of the NACA0018

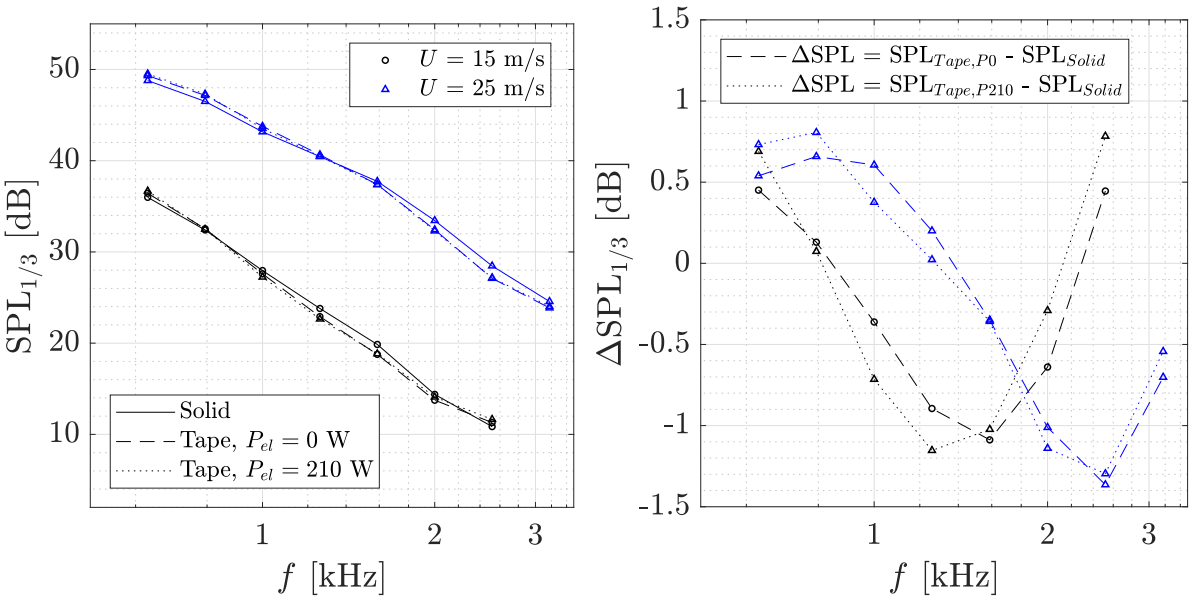

Figure 5.10: Far-field noise spectra of solid and quasi solid TEs including the effects of TE heating. The comparison of noise levels ΔSPL between the different configurations shows that quasi solid and reference TE behave similarly while heating effects are marginal.

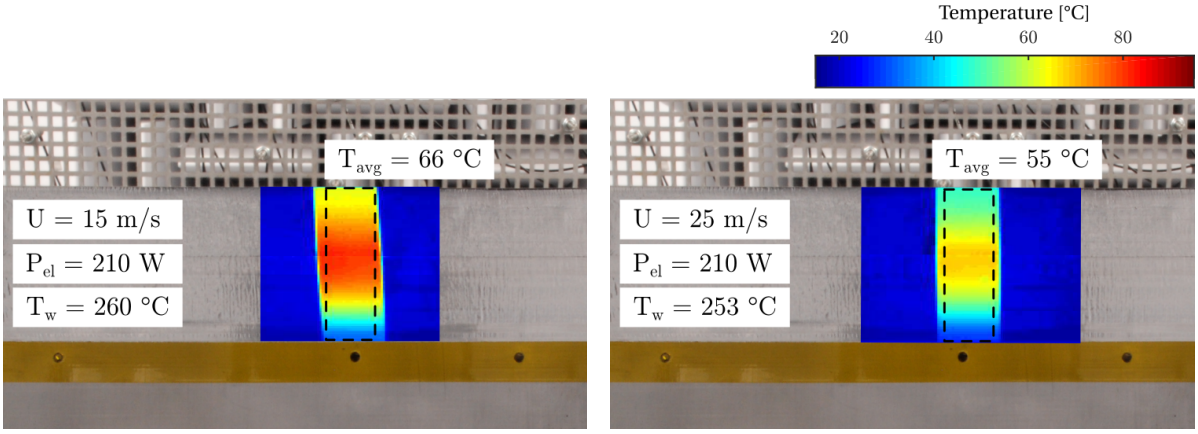

Figure 5.11: Thermal images of heated, quasi solid TEs for two different flow speeds. The surface temperature T_{avg} resulted from averaging within the marked area.

airfoil is estimated to be in the order of $\delta_0 = 10\,\text{mm}$ for $U = 15\,\text{m}\,\text{s}^{-1}$. Considering the short heated surface length of $< 4\,\text{cm}$, it is concluded that no considerable thermal boundary layer developed and that the flow structures were only marginally influenced upon heating.

5.5. Heated Porous Trailing Edges

TBL-TE noise mitigation capabilities of porous materials have been shown in a number of experimental and analytical studies. The results presented in this chapter focus on the *active* change of noise reduction characteristics by means of heated porous TEs. In addition to changing fluid properties in the TE region, possible activation due to geometrical changes of a polymerically coated TE are treated. Finally, the sensitivity of the results with respect to the heating wire layout is evaluated.

5.5.1. Heating Wire Installation Effects

A comparison of far-field noise spectra from porous and solid TEs is given in Figure 5.12 for two different flow speeds. In agreement with previous campaigns [32–35], low-frequency noise was effectively reduced by up to 10 dB. Above a frequency of 1.3 kHz for $U = 15\,\text{m}\,\text{s}^{-1}$ and 2 kHz for $U = 25\,\text{m}\,\text{s}^{-1}$, the use of a porous TE led to noise increase. The occurrence of excess noise is commonly attributed to the higher surface roughness of porous materials. Above a frequency of 1.25 kHz, the slope of the porous TE noise spectra changed with respect to the linear trend at lower frequencies. This hump was not present in the spectrum of the solid TE.

The installation of heating wires inside the P800 metal foam affected the porosity φ of the material since a certain volume of air was replaced by the non-permeable wires. From the known wire diameter, it follows that the effective porosity of the TE decreased from $\varphi = 91.65\,\%$ to $\varphi = 88.1\,\%$. The change in porosity slightly affected the noise mitigation characteristics as shown in Figure 5.12. Far-field noise levels were approximately 1 dB higher in the low-frequency range for both velocities while high-frequency bands were less affected. Based on an aeroacoustic characterization of porous materials, Herr et al. [32] suggested to avoid large rigid structures embedded in porous materials (such as support structures for porous inserts) mainly in order to reduce high-frequency excess noise. In the present case, it is concluded that the installation of 12 spanwise oriented, non-permeable elements negatively influenced the communication between suction and pressure side. Additional noise might have been generated by interactions between the flow and the streamwise pattern of solid elements.

5.5.2. Temperature Characteristics

The performance of TE heating was evaluated based on measurements of the wire and surface temperature. The results are summarized in Figure 5.13 in form of IR image overlays. For the case of $U = 15\,\text{m}\,\text{s}^{-1}$, two power input levels were tested. The achievable average surface temperature in the center region of the TE amounted to 52 °C and 73 °C for the low and high power input, respectively. Maximum surface temperatures were observed at the root of the TE while the tip remained at ambient temperature. The non-homogeneous temperature distribution resulted from strong forced convection of heat caused by flow over the airfoil surface. The mean flow partly penetrated the porous metal foam with its high surface area which led to a strong

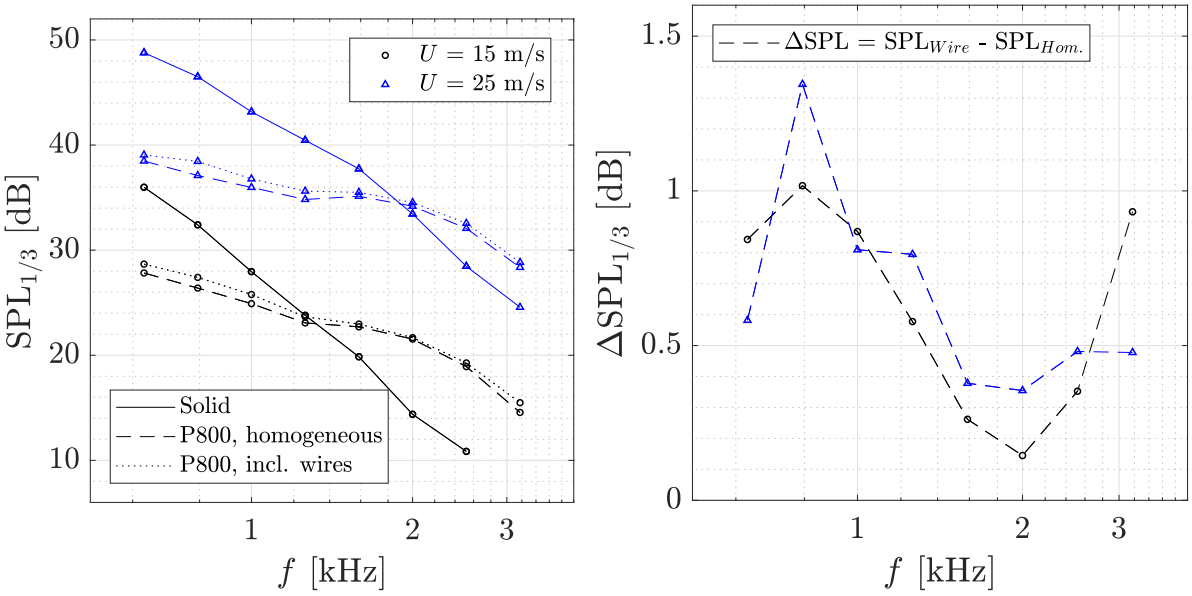

Figure 5.12: Effects of heating wire installation on far-field noise characteristics of porous TEs. A comparison to the solid TE spectra shows effective noise mitigation for low frequencies and increased noise levels in the high-frequency domain.

heat transfer from the material to the flow. Forced convection was most dominant in the tip region due to the decreasing material thickness and poor heat conductivity of the porous metal foam. For the higher flow velocity $U = 25\,\mathrm{m\,s^{-1}}$, convection effects were more pronounced. At maximum power settings, the average surface temperature was 50 °C and a strong temperature gradient in streamwise direction was observed.

The wire temperature was mainly influenced by the electric current and only slightly decreased with increasing flow speed. Wire temperatures of approximately 270 °C close to the root of the TE indicated a strong temperature gradient within the porous material. It is expected that the wire temperature approached the surface temperature more closely in the TE tip region. A more detailed analysis of the heating layout impact on TBL-TE noise is given in Sec. 5.5.5.

5.5.3. Far-Field Noise Levels

Results from the acoustic measurements confirmed that active change of TBL-TE noise characteristics can be achieved by changing the temperature of a porous TE. Far-field noise spectra for two different flow speeds and variations in the heating power input are depicted in Figure 5.14. A broadband increase in noise levels was observed for increasing TE temperature. Five measurements of heated and unheated TEs were alternately conducted and the average SPLs of the runs were plotted in Figure 5.14. Similar levels of noise increase were observed for $U = 25\,\mathrm{m\,s^{-1}}$ at the maximum power setting and $U = 15\,\mathrm{m\,s^{-1}}$ with reduced power. This indicates a relation between the change in broadband noise and the surface temperature distribution. Given the maximum heating input of 210 W, measurements were limited to relatively low flow speeds for which forced convection was less influential and larger spectral noise changes resulted. The maximum SPL variation was observed in the frequency band centered around $f_c = 1.25\,\mathrm{kHz}$ for all heated cases.

The dominant activation mechanism which led to the variation in far-field noise levels is assumed to be the change in TE resistivity upon heating. For communication between the suction and pressure side of the TE, cross-flow through the porous insert must occur. A conservative estimate of the cross-flow order of magnitude can be obtained by assuming that the strongest pressure fluctuations in the boundary layer are responsible for the driving pressure difference Δp between the suction and pressure side. From Eq. 2.6 it can be calculated that $p_{rms} \approx 4\,\mathrm{Pa}$ for the highest tested flow speed $U = 25\,\mathrm{m\,s^{-1}}$. From the resistivity of the P800 metal foam and the TE thickness at the root $t = 1.5\,\mathrm{cm}$, it follows that the seepage velocity lies in the order of $v_s \approx 0.1\,\mathrm{m\,s^{-1}}$ which clearly falls into the linear Darcy flow regime. Based on the experimental results in Chapter 3 it was concluded that with increasing fluid temperature, the seepage velocity decreases for a given pressure difference. Assuming that the seepage flow is effectively heated while penetrating the porous material, the change in fluid viscosity can increases the material resistivity and therefore hampers the communication between the two TE surfaces.

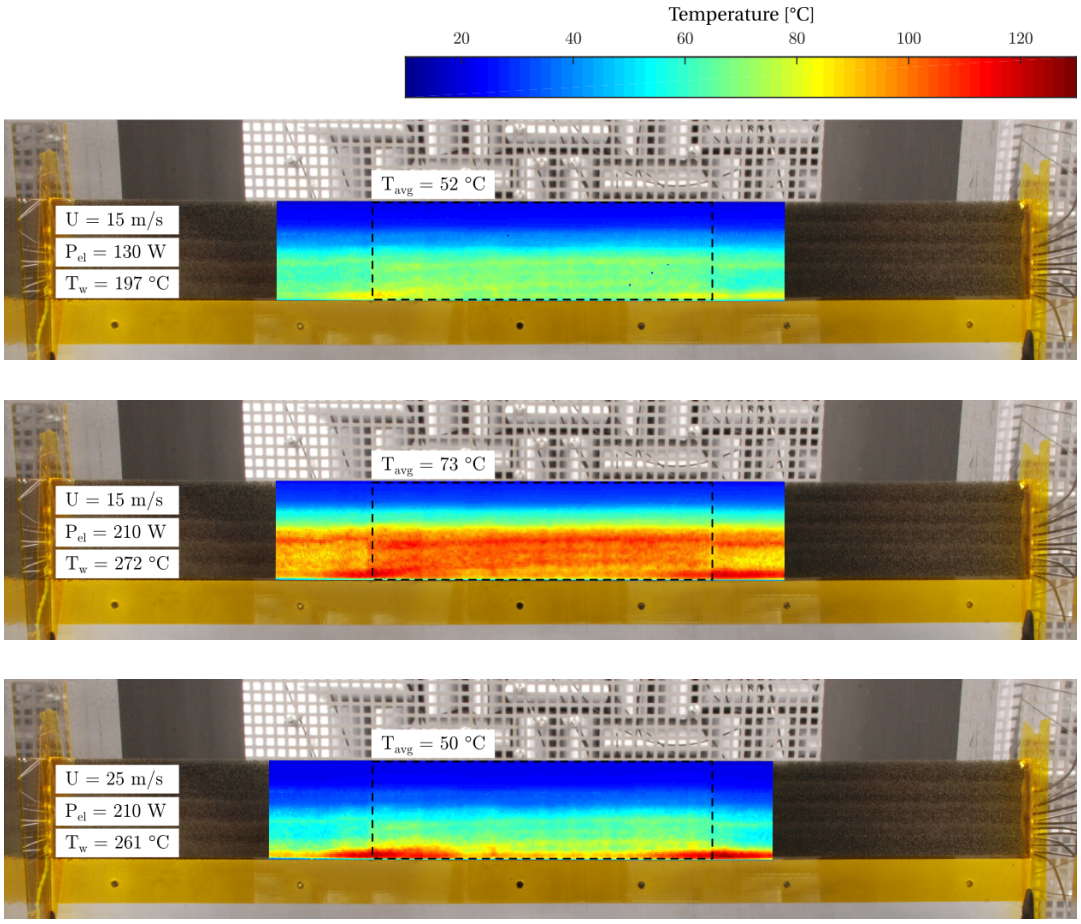

Figure 5.13: Thermal image overlays for three different flow and heating conditions. Dashed areas indicate the averaging regions.

The far-field noise spectra of heated TEs indicate that the frequency bands around 2 kHz and 2.5 kHz were less affected by resistivity changes. This frequency region coincides with the hump in the spectra of unheated porous TEs which was attributed to surface roughness noise. It was observed that roughness noise was unaffected and remained the dominant source for moderate heating levels which agrees with the fact that TE heating did not alter the geometry of the porous metal surface.

Interestingly, the same trend of broadband noise increase and smoothing of the spectral hump was found in the analysis of heating wire installation effects (Figure 5.12). Due to a temperature gradient of roughly 150 °C between the heating wires and the TE surface, the change in material resistivity was not uniform but mostly affected the region close to the heat sources. It is therefore expected that TE heating aggravated the effects responsible for higher noise levels due to the installation of non-permeable regions within the inserts. The expansion of the heating wire insulation was assumed to be negligible since the wires were tightly enclosed in the metal foam. Based on the surface temperature, an effective resistivity of the heated TE can be derived. According to Eq. 3.6, the resistivity increased by 20 % upon heating, assuming that the flow temperature throughout the insert was 100 °C. In a number of experimental studies, the effect of changing permeability on far-field noise spectra was evaluated [32, 33, 36, 42]. For a resistivity increase of less than 50 %, only marginal changes in emitted noise levels (in the order of 1 dB) can be expected according to these studies. However, transferring their observations directly to the present results from TE heating is flawed, firstly because the pore geometry is unaffected by heating and secondly because of the non-uniform temperature distribution inside the material.

From the resulting noise spectra of heated porous TEs, it is inferred that potential noise *reduction* effects of increasing fluid temperature in the vicinity of the TE were not dominant. Supported by the results from Sec. 5.4, a positive impact on pressure fluctuations in the turbulent boundary layer is not expected despite higher heat transfer from the material and better mixing due to increased surface roughness.

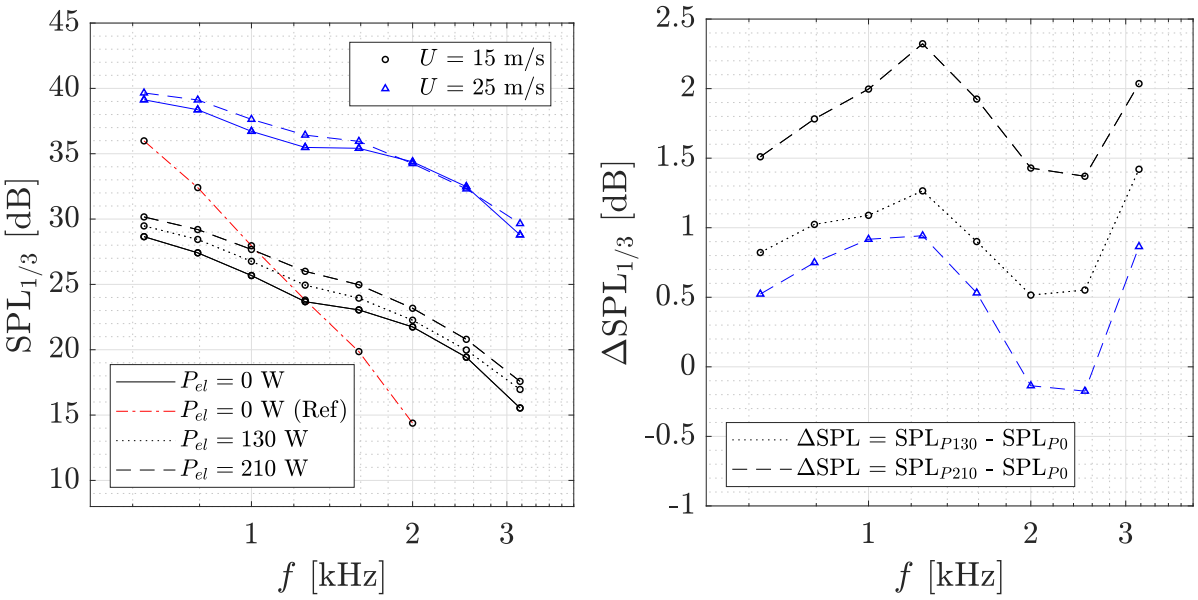

Figure 5.14: Far-field noise spectra of heated porous TEs compared to spectra at ambient conditions. Broadband noise levels increased with rising surface temperature. For $U = 15\,\mathrm{m\,s^{-1}}$, noise levels of the solid reference TE are included.

Critical analysis of the results indicates that additional effects other than resistivity variations could have played a role. Especially for the heated inserts at $U = 15\,\mathrm{m\,s^{-1}}$, broadband noise levels *exceeded* the solid TE noise even in the mid-frequency regime (Figure 5.14). Even though a lack of communication between suction and pressure side would affect the mitigation mechanism negatively, it cannot account for increasing noise beyond the reference case. Excess noise from heated porous TEs might have been caused by fluid which was effectively heated when penetrating the porous material. Local variations in fluid temperature and density were identified as sources of aeroacoustic noise in previous studies.

In the analysis of acoustic source terms based on Lighthill's analogy [11], the term $p - c_0^2\rho$ is commonly neglected due to the assumption of homentropic flow. For the isentropic propagation of acoustic pressure waves, pressure and density fluctuations are balanced. However, this simplification excludes noise sources resulting from changing fluid properties due to temperature variations within the flow field. A study of Morfey [87] concluded that convected flow inhomogeneities can effectively scatter pressure waves in the convective domain into far-field noise. For very low Mach numbers, he showed that variations of the fluid density in the shear layer between a hot, turbulent jet and ambient air led to additional noise. From the resulting velocity scaling law he concluded that scattered far-field noise levels due to convected flow inhomogeneities can surpass noise generated by free turbulence.

The work of Morfey [87] was restricted to free turbulence and the scaling laws were derived for the specific case of jet noise. Ffowcs Williams and Hall [18] derived the well-known U^5 scaling of TBL-TE noise and showed that scattering in the presence of a rigid, semi-infinite surface is much more efficient than the contribution of free turbulence. It is unlikely that convected density fluctuations contribute considerably to broadband far-field noise levels given the dominance of edge noise and the relatively low temperature changes between ambient and heated fluid. This assumption is underlined by the observation that the maximum noise source location was not strongly affected by heating. Figure 5.15 shows a comparison of the source plots for heated and unheated TE conditions at $U = 15\,\mathrm{m\,s^{-1}}$. A slight downstream shift of the maximum noise source location in the order of 1 cm was observed while the general shape of the main lobe remained unaltered. If convected flow inhomogeneities played a major role in noise scattering, a more distinct downstream shift of the source location would have been expected.

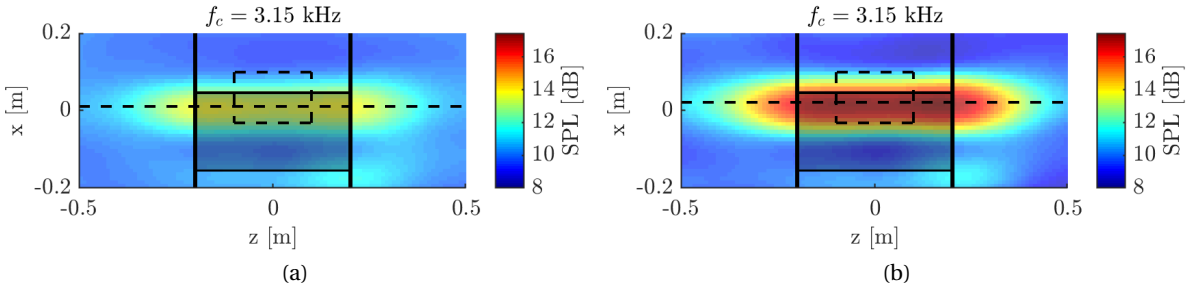

Figure 5.15: 1/3-octave band source maps of the porous TE at ambient conditions (a) and the heated ($P_{el} = 210$ W) porous TE (b) at a flow speed of $U = 15\,\mathrm{m\,s^{-1}}$. Horizontal dashed lines indicate maximum noise source locations and dashed squares illustrate the integration areas.

5.5.4. Trailing Edges with Polymeric Coating

The feasibility of actively changing the permeability of porous TEs was investigated on the basis of heated, polymerically coated inserts. Knowing the isolated effects of TE heating on aeroacoustics, the impact of changing pore sizes due to thermal expansion of the rubbery coating were estimated. Figure 5.16 shows the far-field spectra of the coated porous TE at ambient conditions and for a heating power input of 210 W. For comparability, the spectra of the P800 metal foam at ambient conditions are included. Slightly higher noise levels resulted from the coated P1200 foam within the whole frequency range of interest. Deviations between the two spectra at ambient temperature can be solely attributed to geometrical differences since the soft coating is not expected to affect the wall pressure spectrum (Sec. 4.2). Increasing noise levels can be explained by higher flow resistivity due to reduced pore sizes and plugged pores.

The heating wire installation and electrical power input was identical for the P800 and the coated P1200 TE. The average surface temperatures and their streamwise gradients agreed well between the two cases. Upon heating, the emitted far-field noise levels increased as expected from the previous analysis of heated TEs and from the fact that an expanding coating would lead to increasing resistivity values. An important comparison between the noise levels of the coated and uncoated TE for the same heating inputs is shown in Figure 5.16. The spectra of both TE cases follow the same trend and it is concluded that the effects of changing fluid properties dominated over possible variations in the pore size. The small achievable pore size changes as observed in Sec. 4.3 are in agreement with the aeroacoustic results.

5.5.5. Sensitivity of Results With Respect to Heating Setup

In a second experimental campaign, the influence of the surface temperature distribution on the achievable change in far-field noise was evaluated. Modifications of the heating wire setup aimed for higher surface temperatures close to the TE tip. The modified TE wiring is depicted in Figure 5.17 together with a comparison of the surface temperature profiles in the centerline of the airfoil. For better comparability, the difference between ambient and surface temperature was plotted. The average surface temperature remained similar while a more uniform temperature distribution was achieved in the second campaign. The setup described in Sec. 5.1 was modified by using an acoustic array with optimized microphone distribution [88]. Furthermore, an Optris PI 640 infrared camera was used for recording the surface temperature. Temperature calibration of the two different thermal cameras was performed based on the known flow temperature T_∞.

Figure 5.17 shows that far-field noise spectra were similarly affected by both heated TE configurations. Differences in the plotted ΔSPL values remained below 0.3 dB. It is assumed that the change of noise spectra is insensitive to surface temperature changes in the TE tip region. In addition, the results of the second campaign showed that TE heating effects were reproducible despite changes in the experimental setup.

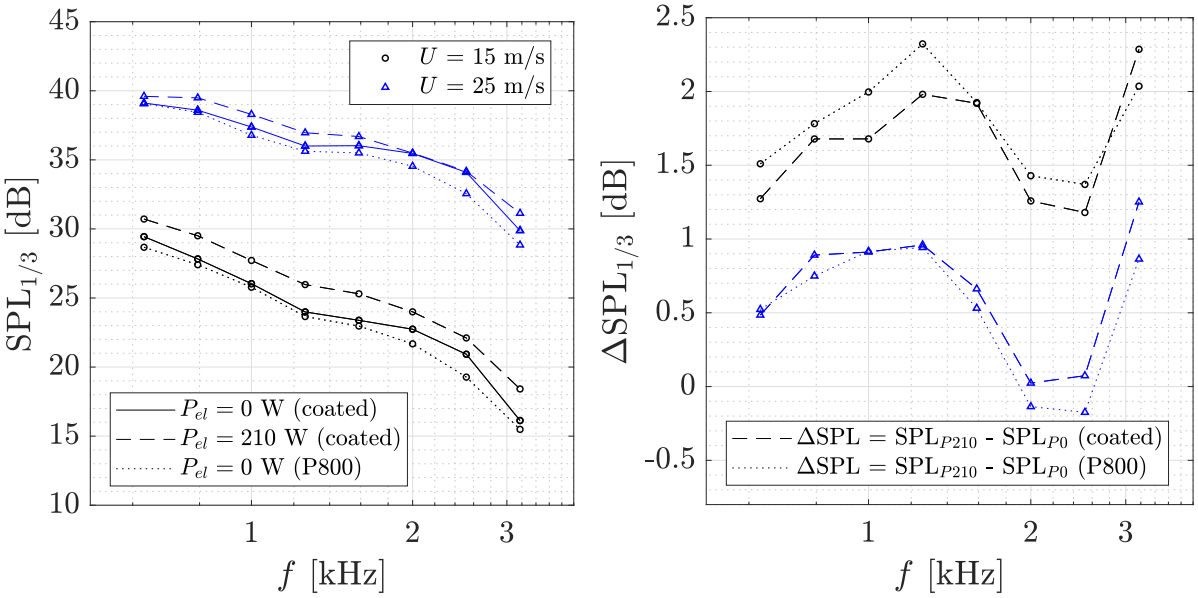

Figure 5.16: Far-field noise spectra of heated TEs with polymeric coating. Noise characteristics of the coated P1200 metal foam are comparable to the P800 foam at ambient conditions. TE heating affects far-field noise radiation of coated and uncoated (P800) TEs similarly.

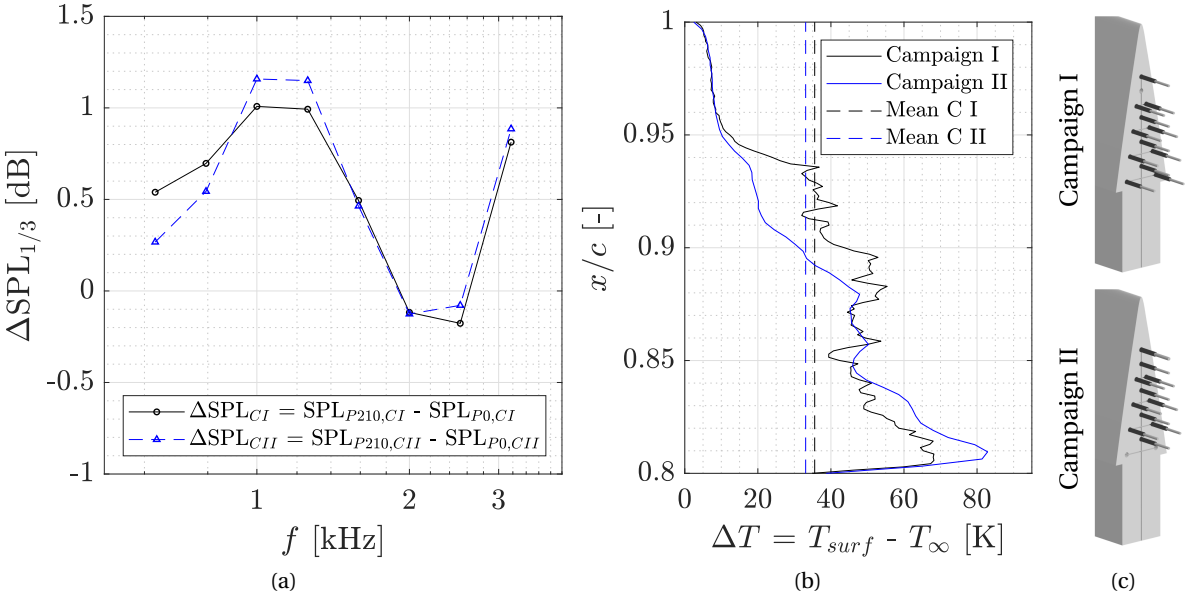

Figure 5.17: Sensitivity of noise spectra with regard to changing heating wire setups for $U = 25\,\mathrm{m\,s^{-1}}$ (a). The different surface temperature distributions (b) did only marginally influence far-field noise. The heating wire setups used in the two campaigns are illustrated in (c).

5.6. Noise Scaling

For verification of the aeroacoustic results, the measured far-field noise spectra were normalized and the resulting scaling laws were compared to previously reported results. From Eq. 1.1 it can be inferred that the noise intensity scales with U^5 as well as with geometrical factors in form of a flow specific length scale δ and the wing span. Several different boundary layer parameters have been used for TBL-TE noise scaling with the goal of representing the size of turbulent structures responsible for noise generation [10]. For the airfoil geometry and Reynolds numbers used here, an estimate of the boundary layer displacement thickness δ^* was obtained from XFOIL [89] due to the lack of experimental data. Table 5.1 lists the flow conditions during the experiments, where the data for $U = 10\,\mathrm{m\,s^{-1}}$ was obtained during the second campaign. Omitting the properties which remained approximately constant throughout the experiments, the relation

$$SPL_{1/3,scaled} = SPL_{1/3} - 10\log\left(\left(\frac{U}{U_{ref}}\right)^n \frac{\delta^*}{L}\right) \tag{5.10}$$

for the scaled SPLs results. For simplicity, the reference speed and length were chosen as $U_{ref} = 1\,\mathrm{m\,s^{-1}}$ and $L = 1\,\mathrm{m}$, respectively. The factor n indicates the power of the free stream velocity which leads to the best collapse of noise spectra. Frequency scaling was applied in the form of the chord-based Strouhal number

$$St = \frac{fc}{U}\,. \tag{5.11}$$

Figure 5.18 shows the scaled noise spectra of the solid reference TE for the flow speeds $U = 10$, 15 and $25\,\mathrm{m\,s^{-1}}$. The noise spectra were plotted with a velocity exponent of $n = 4.5$, for which closest agreement between the individual cases was observed. Previous experimental studies showed similar scaling laws with exponents slightly lower than the well-known U^5 scaling. Oerlemans and Migliore [90] argued that a lower exponent could result from insufficient correction of the integrated source power (refer to Eq. 5.6).

$U_{nom.}$ [$\mathrm{m\,s^{-1}}$]	U_{real} [$\mathrm{m\,s^{-1}}$]	Re [-]	δ^* [mm] (XFOIL)
10	10.3	1.36×10^5	2.81
15	14.7	1.88×10^5	2.55
25	24.5	3.14×10^5	2.24

Table 5.1: Nominal flow speeds during the experiments and real velocities and Reynolds numbers obtained from Pitot tube measurements. The displacement thickness was adapted from XFOIL.

From the scaled noise spectra it can be inferred that within the plotted frequency range, TBL-TE noise was the dominant source. As it was already deduced from the source plots, high-frequency TBL-TE noise cannot be distinguished from background noise if the flow speed is too low. The spurious frequency bands which deviated from the correct scaling are indicated by dotted lines in Figure 5.18.

Scaling of the noise spectra was also applied to the airfoils with porous TE inserts. Figure 5.19 depicts the normalized SPLs according to Eq. 5.10 where $\delta^*/L = 1$ was inserted since displacement thicknesses above the porous insert were expected to deviate from the values predicted by XFOIL. The same velocity exponent $n = 4.5$ as for the solid TE was used. Previously reported scaling laws for TBL-TE noise emitted by partially permeable airfoils are not consistent. In some experiments, $n = 5$ was found for both, solid and porous TEs [32]. Jaworski and Peake [29] derived a U^6 scaling for airfoils with porous edges which indicates less efficient noise scattering compared to solid TEs. Applying a chord-based frequency scaling did not lead to collapsing spectra of porous TEs. The hump locations in the spectra (previously attributed to roughness noise) seem to be independent from the flow speed. The difference between the slopes of the solid and porous TE spectra shows that permeable inserts mainly mitigate low-frequency noise while high-frequency bands receive additional energy from surface roughness noise.

The U^5 scaling was derived for acoustically non-compact airfoils i.e. for airfoils with a long chord length compared to the acoustic wavelength. According to the criterion [12]

$$\frac{2\pi fc}{c_0} \ll 1\,, \tag{5.12}$$

typical edge noise behavior is expected for frequencies higher than $f > 300\,\mathrm{Hz}$, given the present airfoil geometry. Due to the low turbulence inflow and on the basis of the source plots in Sec. 5.3, it is concluded that TBL-TE noise dominates in the low-frequency bands and that interactions with leading edge noise are low.

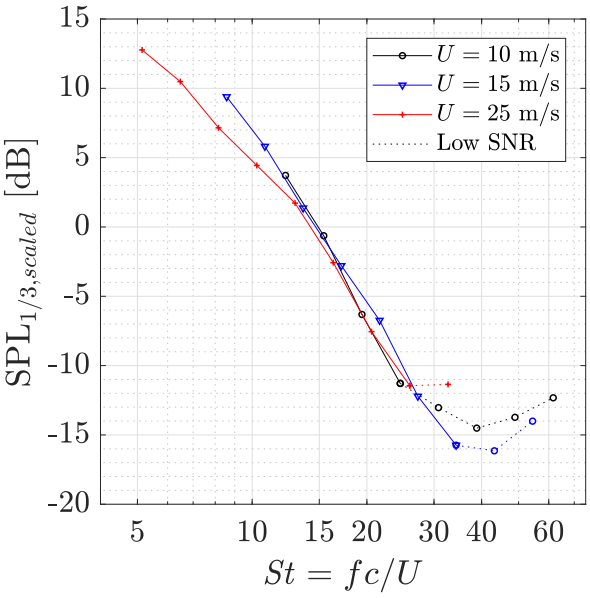

Figure 5.18: Scaling of far-field noise spectra from solid TEs at different flow speeds. Levels were scaled according to Eq. 5.10 with $n = 4.5$. A chord-based Strouhal number was used for frequency scaling.

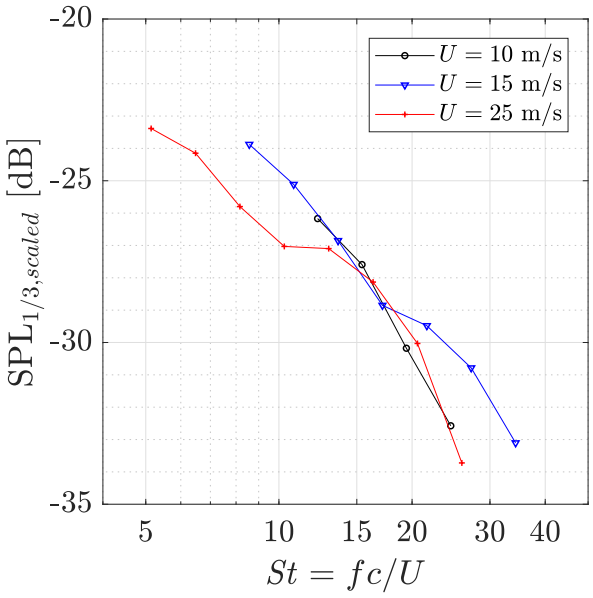

Figure 5.19: Scaling attempt of far-field noise spectra from porous TEs at different flow speeds. Levels were scaled according to Eq. 5.10 with $n = 4.5$ and by assuming $\delta^* / L = 1$. A chord-based Strouhal number was used for frequency scaling.

General scaling laws for the heated TE cases were not found. However, from the far-field characteristics it follows that the most appropriate quantity to predict the change in noise level upon heating is the surface temperature. The wire temperature and electrical power input only weakly depended on the flow speed and are not representative for scaling purposes.

6

Conclusions and Recommendations

The objective of this thesis was to experimentally demonstrate the concept of actively controlled porous materials and to assess the implications for TBL-TE noise mitigation. In the scope of the proposed activation mechanism, namely heating of a polymerically coated porous TE, a distinction between geometrical effects and changing fluid properties was made. From the results of literature study and experiments, the research questions posed in Sec. 1.3 were answered and the main findings are stated in the following.

The first research question addresses the feasibility of the activation mechanism. The sub-questions can be answered as follows:

I.a *Are compliant material effects between surface pressure fluctuations and the heated coating material beneficial for noise mitigation?*
The analysis of possible pressure fluctuation damping mechanisms shows that neither dissipation of turbulent energy nor beneficial interactions between convected pressure waves and surface motions of the compliant coating can be expected. In particular, this holds true for stiff polymeric coatings, such as the sprayable Plasti Dip, applied to rough surfaces.

I.b *What is the achievable pore diameter change of the coated metal foam upon heating?*
Given a maximum activation temperature range and an initial pore size, the volumetric heat expansion coefficient of the coating material defines achievable geometrical changes on a pore-scale level. From the TMA of Plasti Dip it is concluded that a pore size change of $\Delta d_p = 40\,\mu\text{m}$ is theoretically achievable for a porous metal foam with an initial pore size of $d_{p,0} = 1200\,\mu\text{m}$. Results from microscopic imaging imply that actual pore size changes stay below $\Delta d_p = 20\,\mu\text{m}$ due to inhomogeneous coating.

I.c *Is there an observable change in far-field noise levels of porous TEs upon activation of the coating material?*
Aeroacoustic measurements show that far-field noise levels of a NACA0018 airfoil with coated porous TE increase upon heating. A broadband change of up to 2 dB is found for a flow speed of $15\,\text{m}\,\text{s}^{-1}$ and an electrical heating input of 210 W. Since the same changes in emitted noise levels are observed for an uncoated porous TE with comparable surface temperature distribution, it is inferred that the expansion of the coating material plays a minor role compared to fluid temperature effects.

This leads to the conclusion that the proposed activation mechanism is partly effective in changing far-field noise levels. Significant changes of the pore geometry are not achievable mainly because of the low coating volume that can be applied to the porous metal foam. Thus, the change of fluid temperature in the proximity of the porous TE is the dominant influence factor which is addressed by the second research question. The answers to the following sub-questions shed light on the physical mechanisms that alter TBL-TE noise generation:

II.a *What is the functional relation between the resistivity of the permeable metal foam and flow temperature?*
Based on a simple power-law relation between fluid temperature and viscosity, the material resistivity depends on the fluid temperature as follows: $R/R_0 = (T/T_0)^{0.6}$. Using a resistivity rig with built-in heating unit, this relation is observed in good approximation. It is inferred that in the linear Darcy

flow regime, pressure communication between upper and lower side of a permeable TE is hampered upon heating. For the metal foam with 800 µm pore size, the assumption of linear flow behavior is valid up to $v_s = 0.25\,\mathrm{m\,s^{-1}}$. The material specific constants, namely permeability and form coefficient, are not independent from temperature but show variations which tend to counterbalance the effects of increasing resistivity with temperature. However, tested flow temperatures are too low to rule out the effects of measurement uncertainties. A method based on Monte Carlo sampling from known measurement distributions is proposed for estimating the uncertainty of fitting parameters. It is concluded that random measurement errors mostly affect the form coefficient. Limited accuracy and precision of the mass flow meter dominate measurement errors.

II.b *How large is the change in broadband far-field noise levels upon heating of a solid/porous TE and do the results indicate the development of a thermal boundary layer?*
From common scaling laws of wall pressure spectra it is inferred that higher fluid temperatures close to the surface cause reduced pressure fluctuation magnitudes. Far-field noise levels of a quasi-solid TE are not influenced by heating. Thus, it is concluded that the heated surface is too short for the development of a notable thermal boundary layer. For porous TEs, a broadband noise increase is observed upon heating. Noise reducing effects, such as changing fluid temperature in the boundary layer or increased viscous dissipation inside the foam, are therefore not the dominant activation mechanisms.

II.c *Does the installation of heating wires affect far-field noise characteristics of the porous TE and how sensitive are aeroacoustics with respect to changing wire temperature and placement inside the foam?*
Equipping the porous TE with heating wires results in increased broadband noise levels of up to 1.5 dB. The level of TBL-TE noise increase upon heating can best be related to the average surface temperature. For a temperature of 75 °C, far-field noise band levels increase by up to 2.5 dB. Effective heat transfer between the metal foam and the penetrating fluid is assumed since strong temperature gradients along the TE surface and inside the foam occur. Since higher flow temperatures prove to hamper pressure communication, it is stated that resistivity changes upon heating are a main factor for active change of TBL-TE noise emissions. The increase of broadband noise levels with rising fluid temperature is related to the installation effects and similar spectral characteristics are observed. It is therefore argued that not only a uniform change of material resistivity accounts for the magnitude of noise increase but also a non-uniform resistivity distribution with peak values close to the wires. From a variation of the heating wire distribution, it is inferred that noise levels are not sensitive to the surface temperature of the TE tip.

II.d *Are microphone array measurements suitable for detecting small changes of far-field noise levels upon activation?*
Based on the source maps and from applicability of common scaling laws, it is concluded that noise spectra represent TBL-TE noise well within the plotted frequency regions. The use of a fixed, enlarged integration area for SPI is not expected to influence the comparison between solid and porous TE configurations considerably for frequencies below 3 kHz. The repetition of porous TE noise measurements shows that heating effects are reproducible and that the observed changes in noise levels exceed random errors of the measurement technique.

From the analysis of TE temperature effects, it is found that far-field noise levels increase upon heating and partly exceed solid airfoil noise even in the low-frequency regime where no surface roughness noise contribution is expected. This is primarily attributed to resistivity effects; however, excess noise from convected flow inhomogeneities could play an additional role.

In the following, recommendations for future research in the field of permeable materials for airfoil self-noise reduction are listed. From the insights gained throughout the thesis project, possible improvements to the experimental setup as well as alternative solutions for active change of material properties are suggested.

+ Porous materials for TBL-TE noise reduction are commonly characterized by permeability and form coefficient. These properties relate flow through the material to a certain pressure drop which provides a measure of the communication between suction and pressure side of a porous TE. To date, porous material parameters are determined for converged flow conditions (i.e. thick samples) and for *constant* seepage velocities. For future studies, it is suggested to expand the analysis to fluctuating flows and to express the material parameters as a function of flow frequency. This would result in a more accurate

description of the interactions between convected pressure fluctuations and porous materials since the true nature of the pressure field in the vicinity of permeable materials is highly unsteady. In previous studies, it was found that permeability decreases strongly with increasing frequency. This could be an interesting approach towards explaining the observation that porous TEs are most effective in mitigating low-frequency noise.

+ To improve the accuracy of measurements with the existing resistivity rig, it is recommended to measure the flow temperature close to the position of the porous sample. The temperature value provided by the mass flow meter deviated from thermocouple measurements. Furthermore, the heating power output of the modified rig could be increased in order to assess whether permeability and form coefficient are temperature dependent.

+ It was shown that the proposed activation mechanism of heating up a coated TE was not effective in terms of changing the material structure on a pore-scale level. Nevertheless, a temperature controlled activation mechanism is advantageous due to the lack of moving parts and since naturally occurring temperature differences can be used. It is recommended that future research on innovative permeable materials focuses on large-scale activation solutions. Figure 6.1 illustrates a possible activation mechanism that influences the permeability of a porous TE upon heating. Two thin, perforated sheets, which can move freely in only one direction, are embedded within the porous foam. Upon thermal expansion, the relative movement between the sheets influences the overlap of the perforations and thus alters the permeability of the insert. This design would overcome the major issue of the thin expanding coating layer used in this project. Thermal expansion of the sheets in spanwise direction would be in the order of several millimeters.

+ One of the main motivations behind actively controlled porous material properties for low-noise TE applications is the improvement of aerodynamic performance in conditions where noise mitigation is not prioritized. A porous insert with high flow resistivity is expected to be beneficial for lift and drag characteristics of the airfoil. Wake profile measurements were performed in this work; however, only marginal changes were observed upon heating. It is recommended that future studies on activated porous materials include the measurements of airfoil loads especially for angles of attack different from zero at which aerodynamic effects are expected to become more pronounced.

+ In the scope of the second research question, the effect of a TE temperature *below* ambient conditions was investigated. The TE was cooled down by spraying liquid nitrogen on the metal foam. However, it was found that a constant coolant supply would be required since the strong forced convection led to almost instantaneous TE heating after starting the wind tunnel. The replacement of the heating wires with thin tubes would allow for pumping a coolant through the metal foam. Due to its complexity, such a configuration would not be suited for real-life applications but it could support the conclusion that resistivity effects are the cause of the observed far-field noise changes.

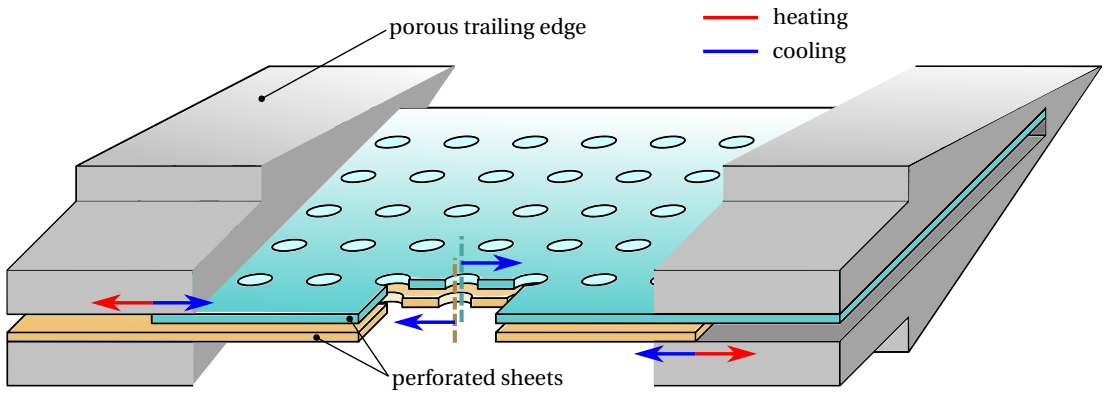

Figure 6.1: Proposed temperature activation mechanism which relies on macroscopic thermal expansion of perforated sheets. The permeability characteristics could be tuned by adjusting sheet overlap and hole spacing.

References

[1] W. Dobrzynski, "Almost 40 Years of Airframe Noise Research: What Did We Achieve?" *Journal of Aircraft*, vol. 47, no. 2, pp. 353–367, 2010.

[2] G. Ruijgrok, *Elements of Aviation Acoustics*. Delft University Press, 1993.

[3] L. Chow, K. Mau, and H. Remy, "Landing Gears and High Lift Devices Airframe Noise Research," in *Proc. of the 8th AIAA/CEAS Aeroacoustics Conference*, June 2002.

[4] Lothar Bertsch, "Noise Prediction within Conceptual Aircraft Design," Ph.D. dissertation, Universität Carolo-Wilhelmina zu Braunschweig, 2013.

[5] E. Pedersen and K. P. Waye, "Perception and annoyance due to wind turbine noise - a dose-response relationship," *The Journal of the Acoustical Society of America*, vol. 116, pp. 3460–3470, 2004.

[6] T. Burton, D. Sharpe, N. Jenkins, and E. Bossanyi, *Wind Energy Handbook*. John Wiley & Sons, 2001.

[7] C. J. Doolan, D. J. Moreau, and L. A. Brooks, "Wind turbine noise mechanisms and some concepts for its control," *Acoustics Australia*, vol. 40, no. 1, pp. 7–13, 2012.

[8] J. Ffowcs Williams, "Aeroacoustics," *Annual Review of Fluid Mechanics*, vol. 9, pp. 447–468, 1977.

[9] G. Lilley, "A study of the silent flight of the owl," in *Proc. of the 4th AIAA/CEAS Aeroacoustics Conference*, 1998.

[10] T. F. Brooks, D. S. Pope, and M. A. Marcolini, "Airfoil self-noise and prediction," *NASA Reference Publication 1218*, 1989.

[11] M. J. Lighthill, "On sound generated aerodynamically I. General theory," *The Royal Society*, vol. 211, pp. 564–587, 1952.

[12] Stefan Pröbsting, "Airfoil Self-Noise - Investigation with Particle Image Velocimetry," Ph.D. dissertation, Technische Universiteit Delft, 2015.

[13] C. Arce León, R. Merino-Martínez, S. Pröbsting, D. Ragni, and F. Avallone, "Acoustic emissions of semi-permeable trailing edge serrations," *Acoustics Australia*, May 2017.

[14] M. Fink and D. Bailey, "Airframe Noise Reduction Studies and Clean-Airframe Noise Investigation," *NASA Contractor Report 159311*, 1980.

[15] S. Oerlemans, P. Sijtsma, and B. M. López, "Location and quantification of noise sources on a wind turbine," *Journal of Sound and Vibration*, vol. 299, pp. 869–883, 2007.

[16] M. J. Lighthill, "On sound generated aerodynamically II. Turbulence as a source of sound," *The Royal Society*, vol. 222, pp. 1–32, 1954.

[17] N. Curle, "The influence of solid boundaries upon aerodynamic sound," *The Royal Society*, vol. 231, pp. 505–514, 1955.

[18] J. Ffowcs Williams and L. Hall, "Aerodynamic sound generation by turbulent flow in the vicinity of a scattering half plane," *Journal of Fluid Mechanics*, vol. 40, pp. 657–670, 1970.

[19] T. Lutz, A. Herrig, W. Würz, M. Kamruzzaman, and E. Krämer, "Design and Wind-Tunnel Verification of Low-Noise Airfoils for Wind Turbines," *AIAA Journal*, vol. 45, pp. 779–785, 2007.

[20] M. S. Howe, "Aerodynamic noise of a serrated trailing edge," *Journal of Fluids and Structures*, vol. 5, pp. 33–45, 1991.

[21] M. Azarpeyvand, M. Gruber, and P. F. Joseph, "An analytical investigation of trailing edge noise reduction using novel serrations," in *Proc. of the 19th AIAA/CEAS Aeroacoustics Conference*, Berlin, Germany, 2013.

[22] F. Avallone, S. Pröbsting, and D. Ragni, "Three-dimensional flow field over a trailing-edge serration and implications on broadband noise," *Physics of Fluids*, vol. 28, 2016.

[23] M. Herr and W. Dobrzynski, "Experimental Investigations in Low-Noise Trailing-Edge Design," *AIAA Journal*, vol. 43, no. 6, pp. 1167–1175, June 2005.

[24] M. Herr, "Design Criteria for Low-Noise Trailing-Edges," in *Proc. of the 13th AIAA/CEAS Aeroacoustics Conference*. American Institute of Aeronautics and Astronautics, 2007.

[25] M. S. Howe, *Acoustics of Fluid-Structure Interactions*. Cambridge University Press, 1998.

[26] L. Kamps, C. Brücker, T. F. Geyer, and E. Sarradj, "Airfoil Self Noise Reduction at Low Reynolds Numbers Using a Passive Flexible Trailing Edge," in *Proc. of the 23rd AIAA/CEAS Aeroacoustics Conference*, June 2017.

[27] R. E. Hayden, "Exploratory investigation of aeroacoustic optimization of the variable impedance edge concept applied to upper surface blown configurations," *NASA Contractor Report 145072*, 1976.

[28] M. S. Howe, "On the added mass of a perforated shell, with application to the generation of aerodynamic sound by a perforated trailing edge," *Proceedings of the Royal Society of London*, vol. 365, no. 1721, pp. 209–233, 1979.

[29] J. W. Jaworski and N. Peake, "Aerodynamic noise from a poroelastic edge with implications for the silent flight of owls," *Journal of Fluid Mechanics*, vol. 723, pp. 456–479, 2013.

[30] A. Kisil and L. Ayton, "Aerodynamic noise from rigid trailing edges with finite porous extensions," *Journal of Fluid Mechanics*, vol. 836, pp. 117–144, 2018.

[31] L. Rossian, R. Ewert, and J. W. Delfs, "Prediction of Airfoil Trailing Edge Noise Reduction by Application of Complex Porous Material," in *New Results in Numerical and Experimental Fluid Mechanics XI*. Springer International Publishing, 2018, pp. 647–657.

[32] M. Herr, K.-S. Rossignol, J. Delfs, N. Lippitz, and M. Mößner, "Specification of Porous Materials for Low-Noise Trailing-Edge Applications," in *Proc. of the 20th AIAA/CEAS Aeroacoustics Conference, AIAA AVIATION Forum*, June 2014.

[33] T. Geyer, E. Sarradj, and C. Fritzsche, "Porous airfoils: noise reduction and boundary layer effects," in *Proc. of the 15th AIAA/CEAS Aeroacoustics Conference*, May 2009.

[34] T. Geyer and E. Sarradj, "Trailing edge noise of partially porous airfoils," in *Proc. of the 20th AIAA/CEAS Aeroacoustics Conference, AIAA AVIATION Forum*, June 2014.

[35] A. Rubio Carpio, F. Avallone, and D. Ragni, "On the Role of the Flow Permeability of Metal Foams on Trailing Edge Noise Reduction," in *Proc. of the 2018 AIAA/CEAS Aeroacoustics Conference. Atlanta, Georgia*, June 2018.

[36] A. Rubio Carpio, R. Merino-Martínez, F. Avallone, D. Ragni, M. Snellen, and S. van der Zwaag, "Broadband Trailing Edge Noise Reduction Using Permeable Metal Foams," in *Proc. of the 46th International Congress and Exposition on Noise Control Engineering Taming Noise and Moving Quiet*, August 2017, pp. 4373–4383.

[37] T. F. Geyer and E. Sarradj, "Noise reduction and aerodynamics of airfoils with porous trailing edges," in *Proc. of the 2018 Inter-Noise*, Chicago, Illinois, August 2018.

[38] S. A. Showkat Ali, M. Azarpeyvand, and C. R. I. da Silva, "Trailing-edge flow and noise control using porous treatments," *Journal of Fluid Mechanics*, vol. 850, pp. 83–119, 2018.

[39] B. Y. Zhou and N. R. Gauger, "On the Adjoint-based Control of Trailing-Edge Turbulence and Noise Minimization via Porous Material," in *Proc. of the 21th AIAA/CEAS Aeroacoustics Conference, AIAA AVIATION Forum*, June 2015.

[40] J. Schulze and J. Sesterhenn, "Optimal distribution of porous media to reduce trailing edge noise," *Computers & Fluids*, vol. 78, pp. 41–53, 2013.

[41] X. Sagartzazu, L. Hervella-Nieto, and J. Pagalday, "Review in Sound Absorbing Materials," *Archives of Computational Methods in Engineering*, vol. 15, pp. 311–342, 2008.

[42] E. Sarradj and T. Geyer, "Noise Generation by Porous Airfoils," in *Proc. of the 13th AIAA/CEAS Aeroacoustics Conference*. American Institute of Aeronautics and Astronautics, 2007.

[43] F. M. White, *Viscous Fluid Flow*, 2nd ed. McGraw-Hill, 1991.

[44] S. B. Pope, *Turbulent Flows*. Cambridge University Press, 2000.

[45] T. F. Brooks and T. Hodgson, "Trailing edge noise prediction from measured surface pressures," *Journal of Sound and Vibration*, vol. 78, pp. 69–117, 1981.

[46] N. Renard and S. Deck, "On the scale-dependent turbulent convection velocity in a spatially developing flat plate turbulent boundary layer at Reynolds number Re = 13 000," *Journal of Fluid Mechanics*, vol. 775, pp. 105–148, 2015.

[47] H. Choi and P. Moin, "On the space-time characteristics of wall-pressure fluctuations," *Physics of Fluids A: Fluid Dynamics*, vol. 2, pp. 1450–1460, 1990.

[48] P. Moin, "Revisiting Taylor's hypothesis," *Journal of Fluid Mechanics*, vol. 640, pp. 1–4, 2009.

[49] G. Schewe, "On the structure and resolution of wall-pressure fluctuations associated with turbulent boundary-layer flow," *Journal of Fluid Mechanics*, vol. 134, pp. 311–328, 1983.

[50] A. L. Lagenelli, A. Martellucci, and L. Shaw, "Prediction of Turbulent Wall Pressure Fluctuations in Attached Boundary Layer Flow," in *Proc. of the 14th AIAA Fluid and Plasma Dynamics Conference*, June 1981.

[51] Y. C. Küçükosman, J. Christophe, and C. Schram, "Trailing edge noise prediction based on wall pressure spectrum models for NACA0012 airfoil," *Journal of Wind Engineering & Industrial Aerodynamics*, vol. 175, pp. 305–316, 2018.

[52] M. Goody, "Empirical Spectral Model of Surface Pressure Fluctuations," *AIAA Journal*, vol. 42, pp. 1788–1794, 2004.

[53] T. Meyers, J. B. Forest, and W. J. Devenport, "The wall-pressure spectrum of high-reynolds-number turbulent boundary-layer flows over rough surfaces," *Journal of Fluid Mechanics*, vol. 768, pp. 261–293, 2015.

[54] G. S. Beavers and D. D. Joseph, "Boundary conditions at a naturally permeable wall," *Journal of Fluid Mechanics*, vol. 30, pp. 197–207, 1967.

[55] S. Glegg and W. Devenport, "The far-field sound from rough-wall boundary layers," *Proceedings of the Royal Society A*, vol. 465, pp. 1717–1734, 2009.

[56] Y. Liu, A. P. Dowling, and H.-C. Shin, "Effects of Surface Roughness on Airframe Noise," in *Proc. of the 12th AIAA/CEAS Aeroacoustics Conference*, Cambridge, Massachusetts, USA, May 2006.

[57] B. R. Kramer, B. C. Smith, J. P. Heid, G. K. Noffz, D. M. Richwine, and T. Ng, "Drag Reduction Experiments Using Boundary Layer Heating," in *Proc. of the 37th AIAA Aerospace Science Meeting and Exhibit*, January 1999.

[58] J. L. Lage, "The fundamental theory of flow through permeable media," in *Transport Phenomena in Porous Media*, D. B. Ingham and I. Pop, Eds. Pergamon, 1998, pp. 1–30.

[59] J. M. Baloyo, "Open-cell porous metals for thermal management applications: fluid flow and heat transfer," *Materials Science and Technology*, vol. 33, 2017.

[60] "Acoustics - materials for acoustical applications - determination of airflow resistance," International Organization for Standardization, ISO 9053, 1993.

[61] J. R. Philip, "Transient Fluid Motions in Saturated Porous Media," *Australian Journal of Physics*, vol. 10, pp. 43–53, 1957.

[62] P. Sheng and M.-Y. Zhou, "Dynamic Permeability in Porous Media," *Physical Review Letters*, vol. 61, pp. 1591–1594, 1988.

[63] D. R. A. Christie, "Measurement of the acoustic properties of a sound absorbing material at high temperatures," *Journal of Sound and Vibration*, vol. 46, pp. 347–355, 1976.

[64] W. W. Pulkrabek and W. E. Ibele, "The effect of temperature on the permeability of a porous material," *International Journal of Heat and Mass Transfer*, vol. 30, pp. 1103–1109, 1987.

[65] D. A. Nield, "Resolution of a Paradox Involving Viscous Dissipation and Nonlinear Drag in a Porous Medium," *Transport in Porous Media*, vol. 41, pp. 349–357, 2000.

[66] *Operation Manual Digital Pressure Gauge, Series 2100*, Mensor Corporation.

[67] *Instruction Manual EL-FLOW Select Series, Thermal Mass Flow Meters and Controllers*, Bronkhorst High-Tech B.V.

[68] E. Baril, A. Mostafid, L.-P. Lefebvre, and M. Medraj, "Experimental Demonstration of Entrance/Exit Effects on the Permeability Measurements of Porous Materials," *Advanced Engineering Materials*, vol. 10, pp. 889–894, 2008.

[69] W. H. Press, S. A. Teukolsky, W. T. Vetterling, and B. P. Flannery, *Numerical Recipes in C*. Cambridge University Press, 2002.

[70] C. Lind, "Two Decades of Negative Thermal Expansion Research: Where Do We Stand?" *Materials*, vol. 5, pp. 1125–1154, 2012.

[71] M. F. Ashby, *Materials Selection in Mechanical Design*, 3rd ed. Elsevier Butterworth-Heinemann, 2005.

[72] R. Simha and R. F. Boyer, "On a General Relation Involving the Glass Temperature and Coefficients of Expansion of Polymers," *The Journal Of Chemical Physics*, vol. 37, no. 5, pp. 1003–1007, 1962.

[73] M. D. Rao, "Recent applications of viscoelastic damping for noise control in automobiles and commercial airplanes," *Journal of Sound and Vibration*, vol. 262, pp. 457–474, 2003.

[74] Z. Zheng, "Effects of compliant coatings on radiated sound from a rigid-wall turbulent boundary layer," *Journal of Fluids and Structures*, vol. 19, pp. 933–941, 2004.

[75] M. Howe, "Surface pressure fluctuations produced by vortex shedding from a coated airfoil," *Journal of Sound and Vibration*, vol. 113, pp. 233–244, 1987.

[76] M. Gad-El-Hak, "Compliant Coatings Research: A Guide to the Experimentalist," *Journal of Fluids and Structures*, vol. 1, pp. 55–70, 1987.

[77] V. M. Kulik, "Deformation of viscoelastic coating in a turbulent flow," *Thermophysics and Aeromechanics*, vol. 16, no. 1, pp. 43–55, 2009.

[78] V. M. Kulik, I. Lee, and H. H. Chun, "Wave properties of coating for skin friction reduction," *Physics of Fluids*, vol. 20, 2008.

[79] A. V. Boiko, V. M. Kulik, H.-H. Chun, and I. Lee, "Verification of drag-reduction capabilities of stiff compliant coatings in air flow at moderate speeds," *International Journal of Naval Architecture and Ocean Engineering*, vol. 3, pp. 242–253, 2011.

[80] J. R. Underbrink, "Circulary symmetric, zero redundancy, planar array having broad frequency range applications," U.S. Patent US 6,205,224 B1, 2001.

[81] C. S. Allen, W. K. Blake, R. P. Dougherty, D. Lynch, P. T. Soderman, and J. R. Underbrink, *Aeroacoustic Measurements*, Thomas J. Mueller, Ed. Springer-Verlag Berlin Heidelberg, 2002.

[82] R. Merino-Martínez, M. Snellen, and D. G. Simons, "Functional Beamforming Applied to Imaging of Flyover Noise on Landing Aircraft," *Journal of Aircraft*, vol. 53, pp. 1830–1843, 2016.

[83] P. Sijtsma, "Phased array beamforming applied to wind tunnel and fly-over tests," *National Aerospace Laboratory NLR Report*, 2010.

[84] R. Merino-Martínez, P. Sijtsma, and M. Snellen, "Inverse Integration Method for Distributed Sound Sources," in *Proc. of the 7th Berlin Beamforming Conference*, Berlin, 2018.

[85] Roberto Merino-Martínez, "Microphone arrays for imaging of aerospace noise sources," Ph.D. dissertation, Technische Universiteit Delft, 2018.

[86] R. A. Antonia, H. Q. Danh, and A. Prabhu, "Response of a turbulent boundary layer to a step change in surface heat flux," *Journal of Fluid Mechanics*, vol. 80, pp. 153–177, 1977.

[87] C. L. Morfey, "Amplification of aerodynamic noise by convected flow inhomogeneities," *Journal of Sound and Vibration*, vol. 31, pp. 391–397, 1973.

[88] S. Luesutthiviboon, "Design of an Optimized Acoustic Array for Aero-acoustic Research in an Open-jet Anechoic Wind Tunnel," Master's thesis, Technische Universiteit Delft, 2017.

[89] Mark Drela and Harold Youngren, "XFOIL 6.9," 1986, MIT.

[90] S. Oerlemans and P. Migliore, "Aeroacoustic Wind Tunnel Tests of Wind Turbine Airfoils," in *Proc. of the 10th AIAA/CEAS Aeroacoustics Conference*, 2004.

[91] M. Weidenfeld and A. Manela, "On the attenuating effect of permeability on the low frequency sound of an airfoil," *Journal of Sound and Vibration*, vol. 375, pp. 275–288, 2006.

[92] J. Katz and A. Plotkin, *Low-Speed Aerodynamics*. Cambridge University Press, 2001.

[93] J. E. Ffowcs Williams, "The acoustics of turbulence near sound-absorbent liners," *Journal of Fluid Mechanics*, vol. 51, pp. 737–749, 1972.

A

Potential Flow Field in the Vicinity of a Permeable Trailing Edge

In the scope of relating TE resistivity to far-field noise levels, the possibility of using an analytical model was evaluated. The main motivation was to predict the impact of resistivity changes upon heating on emitted noise levels. For this purpose, the approach of Weidenfeld and Manela [91] was adapted and its applicability to porous TEs was tested.

Weidenfeld's model provides a numerically cheap method for calculating the acoustic power emitted from permeable, thin 2D airfoils. Instead of considering the porous material on a pore-scale level, only macroscopic effects, which follow from Darcy's law (Eq. 3.2), are taken into account. The description of the flow field near the airfoil is based on potential flow theory and an acoustic analogy is applied for the radiated far-field noise. In the following analysis, the focus lies on the unsteady flow field resulting from a convected vortex over a partially porous airfoil.

Implementation of the near-field flow solution closely followed the procedure described in [92]. The 2D airfoil was discretized by N panels of length $c_j = c/N$. A bound vortex with strength Γ_j was placed at $0.25c_j$ of each panel and a control point was defined at $0.75c_j$. The sum of bound vortices equals to the overall circulation of the airfoil Γ_a from which the loads can be derived. In every time step t_n, a wake vortex of strength Γ_w was shed. Applying Kelvin's theorem, the shed vortex strength follows from

$$-\Gamma_{w,n} = \Gamma_{a,n} - \Gamma_{a,n-1} \,. \tag{A.1}$$

Unsteady wake roll-up was implemented by considering the interactions between previously shed wake vortices. In order to simulate the mechanism leading to TBL-TE noise, a free vortex Γ_f was released upstream of the airfoil at time $t = 0$. The unsteady velocity field around the airfoil followed from the induced velocities of free, bound and shed vortices. The strength of the bound vortices was updated in every time step and resulted from satisfying the condition that the surface-normal induced velocity v_i has to vanish in every control point of the solid airfoil

$$v_{i,a} + v_{i,w} + v_{i,f} = 0 \,. \tag{A.2}$$

For a partially permeable airfoil, Weidenfeld and Manela [91] suggested to modify the boundary condition in Eq. A.2 by replacing the RHS with the seepage velocity v_s through the airfoil surface. The instantaneous

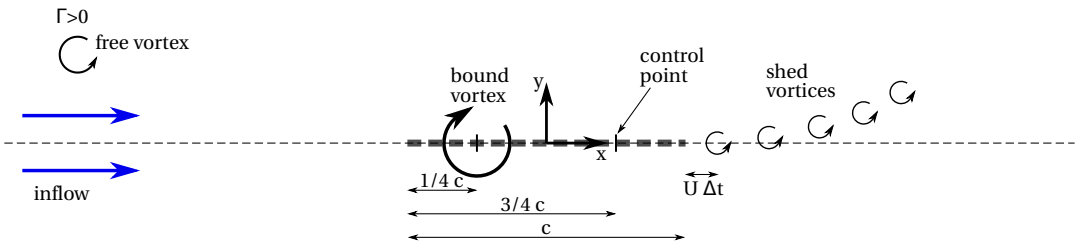

Figure A.1: 2D permeable airfoil and its interaction with a convected vortex. The airfoil is represented by a lumped vortex element and the wake is simulated by discrete shed vortices.

seepage velocity follows from the pressure difference Δp between suction and pressure side of the airfoil

$$v_s(x,t) = -\kappa h(x) \Delta p(x,t) \,. \tag{A.3}$$

Here, $\kappa = K/(\mu t)$ denotes the permeability parameter of a porous material with permeability K and thickness t. The permeability distribution along the airfoil is expressed through $h(x)$. The relation in Eq. A.3 is valid in the linear Darcy flow regime, i.e. for low seepage velocities.

The driving pressure difference Δp is obtained from the instantaneous flow field at the airfoil surface in the form of the unsteady Bernoulli equation

$$\Delta p(x,t) = \rho U \gamma(x,t) + \rho \frac{\partial}{\partial t} \int_0^x \gamma(s,t)\, \mathrm{d}s \,. \tag{A.4}$$

Instead of using a continuous circulation distribution γ, the discrete circulations Γ_j of the airfoil panels were used here.

Implementing the unsteady potential flow model for the case of a convected vortex past a permeable surface required additional modeling with respect to commonly used schemes. The following list summarizes the main assumptions and approximations for the near-field calculations.

- In potential flow theory, a model for the vortex core is required to avoid singularities. Especially when the time step Δt becomes too small, shed vortices are located close to each other and high induced velocities close to the vortex center regions lead to unstable simulations. A correction of the vortex-induced velocity by a factor of

  $$1 - \exp(-r^2/c_{lo}) \tag{A.5}$$

  proved to be effective. The constant of the so called Lamb-Oseen vortex was chosen as $c_{lo} = 0.003$ for modeling the free and wake vortices. Directly in the center $r = 0$, the induced velocity vanishes while it approaches the original value of the irrotational vortex for large distances away from the core.

- In order to capture the true unsteady behavior of the airfoil, a continuous sheet of shed wake vortices would be required. If discrete vortices are shed, their initial location downstream of the TE has to be determined. Within one time step, the airfoil moves $\Delta x = U \Delta t$ and Katz and Plotkin [92] suggested to place the shed vortex at a distance of 0.2 - 0.3Δx behind the TE. For locations further downstream, it was argued that unsteady effects are underestimated due to the limited influence of the most recent shed vortex. Weidenfeld and Manela [91] carried out their simulations for a shedding distance of Δx behind the TE and therefore introduced a certain error in the unsteady behavior. Varying the vortex location in multiple simulations resulted in observable variations of the unsteady airfoil loads. For reasons of comparability, Weidenfeld and Manela's choice was adapted in the present study.

- Special attention was paid to the impact of airfoil permeability on the numerical scheme. The unsteady loads (i.e. the pressure distribution) of a solid airfoil, which encounters a convected vortex, were mainly influenced by the term $\rho U \gamma(x,t)$ in Eq. A.4. In the case of a permeable surface, the unsteady term in Bernoulli's law can lead to unstable numerical behavior.

  The main cause of unstable behavior was identified as the instantaneous change of seepage velocity with changing pressure fields. Already low local pressure differences caused high changes of seepage velocity which in turn affected the bound vortex distribution and led to increasing magnitude of the unsteady term in Bernoulli's equation. It is assumed that in reality, inertial effects would prevent the strong coupling between seepage flow and pressure fluctuations.

  In the implementation of the numerical scheme, the time derivative of the integrated circulation distribution was approximated by the finite difference

  $$\frac{\int_0^x \gamma(s,t_n)\, \mathrm{d}s - \int_0^x \gamma(s,t_{n-n_x})\, \mathrm{d}s}{n_x \Delta t} \,. \tag{A.6}$$

  Depending on the permeability distribution, only n_x values higher than 4 led to stable results.

Correct implementation of the potential flow model was checked by comparing the time evolving airfoil circulation to the results of Weidenfeld and Manela [91]. Note that their permeability distribution is numerically

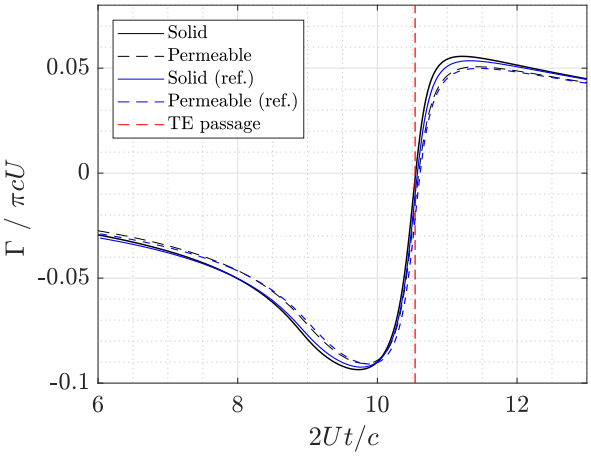

Figure A.2: Unsteady airfoil loading in the case of a permeable and non-permeable surface. For validation of the implementation, the results from Weidenfeld and Manela [91] are included. The underlying simulation parameters are listed in Table A.1.

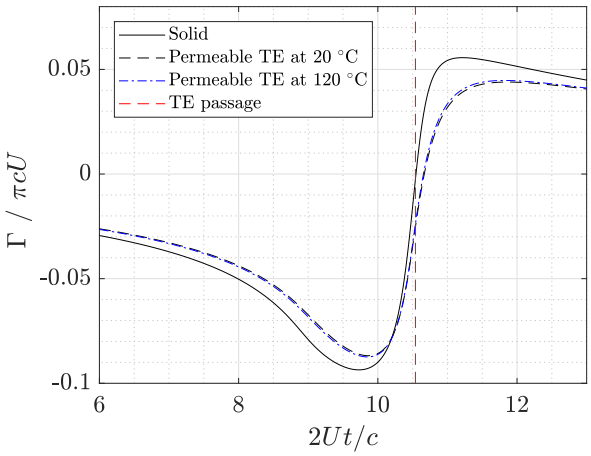

Figure A.3: Unsteady loads of an airfoil with permeable TE of length $0.2c$. The results for two different flow temperatures (i.e. different resistivity values) are plotted.

easy to handle since the permeability at the airfoil tip vanishes while it gradually increases towards the TE. This way, high seepage velocities in the suction peak region are avoided. Furthermore, a relatively low permeability parameter was chosen which is beneficial for numeric stability as well. The simulation parameters used for the comparability study are listed in Table A.1.

Figure A.2 shows the normalized airfoil circulation $\Gamma/(\pi cU)$ as a function of the reduced time $2tU/c$ in comparison with the results from Weidenfeld and Manela [91]. Close agreement of the simulation results was observed with minor deviations in the regions of minimum and maximum circulation. The permeable airfoil experienced reduced loads compared to the solid reference case since pressure differences were partly balanced. Reduction of the loads was most pronounced around the circulation peaks. The vertical dashed line in Figure A.2 indicates the point in time when the convected vortex passed the TE. Around this point, the steepest gradients in the airfoil circulation were observed and unsteady pressure effects are assumed to be dominant according to Eq. A.4. This stresses the importance of modeling the vortex shedding process correctly. Furthermore, it indicates that simulation results are sensitive to permeability variations in the TE region.

An instantaneous pressure distribution around the airfoil is plotted in Figure A.4 together with a visualization of the wake structure. The influence of the convected vortex on the shed wake vortices is visible and agrees with the simulation results of Weidenfeld and Manela [91]. A suction peak close to the airfoil tip was present due to effective angles of attack different from 0°.

It is assumed that deviations from the results of Weidenfeld and Manela [91] arose from numerical differences between the schemes. The different representation of the bound vortices (continuous distribution vs. lumped vortex elements) and the unknown vortex core modeling in the work of Weidenfeld and Manela [91] are regarded as the major differences. A reduction of the time step below $\Delta t = 5 \times 10^{-3}$ s did not strongly influence the airfoil circulation obtained in the present simulation.

In order to determine the effects of porous TEs on unsteady airfoil loads, the previous simulation setup was slightly modified. Up to $x/c = 0.8$, the airfoil surface was non-permeable. The permeability parameter for the porous TE was calculated from the resistivity of the P800 metal foam with an assumed thickness of 1 cm which resulted in $\kappa = 15.9 \times 10^{-3}$. The decrease of TE thickness was simulated by linearly changing the TE permeability according to $h(x) = (x - 0.8c)/(0.2c) + 1$. Simulating the true TE, which approaches zero thickness, was not possible due to numerical instabilities.

Figure A.3 depicts the achievable reduction of airfoil loads due to permeable TEs. The heated TE was simulated by assuming a fluid temperature increase of $\Delta T = 100\,°\mathrm{C}$ resulting in a new permeability parameter of $\kappa = 13.4 \times 10^{-3}$ according to Eq. 3.6. The simulation results imply that heating does not influence the airfoil loading considerably.

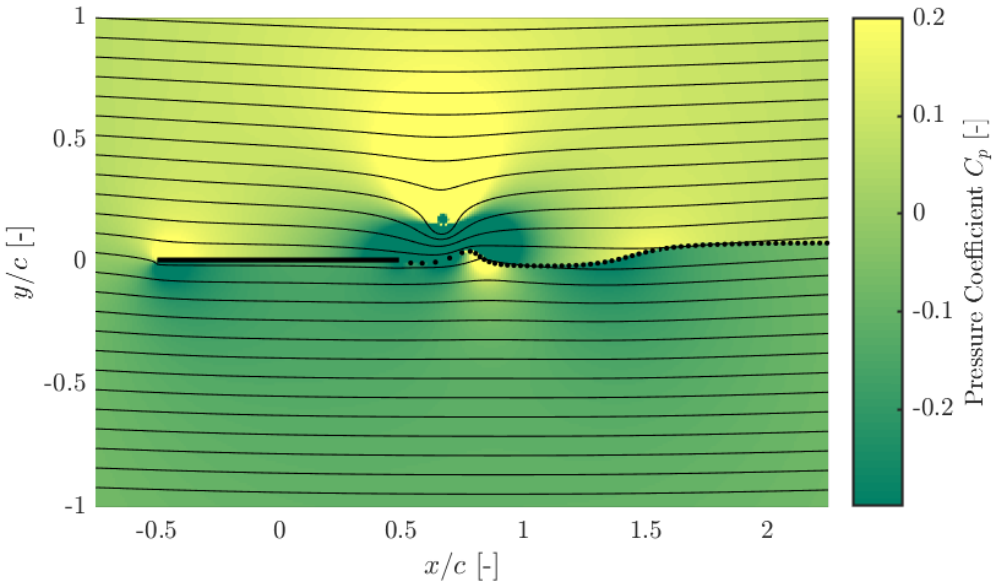

Figure A.4: Pressure distributions and streamlines in the vicinity of a partly porous airfoil. The convected vortex position is downstream of the TE and black dots indicate the position of shed wake vortices.

A.1. Far-Field Solution

Weidenfeld and Manela [91] derived an expression for the far-field acoustic pressure based on the theory of vortex sound. They restricted their analysis to interactions between vorticity in the flow field and a compact airfoil surface. The description of the unsteady flow field mentioned above served as source term for the far-field solution. For partially porous airfoils, three contributions to the acoustic pressure were identified. Beside the influence of convected and wake vortices, the fluctuating seepage flow perpendicular to the airfoil surface was considered in the superposition of source terms. The contribution of the latter was adapted from the work of Ffowcs Williams [93] on acoustics of turbulent flow near perforated liners. He provided an expression for acoustic pressure resulting from flow which is forced through small apertures. This noise source becomes less efficient when the permeable surface is regarded as acoustically transparent, i.e. when the aperture diameters are large or when the frequency is low.

Implementation of the far-field pressure calculation showed that the seepage noise contribution of TEs with high permeabilities becomes large and outweighs positive effects from reduced loading. This does not

Parameter	Simulation	Weidenfeld and Manela [91]
Flow speed U	$15\,\mathrm{m\,s^{-1}}$	-
Initial Angle of attack α	0°	0°
Convected vortex strength $\Gamma/(\pi cU)$	0.2	0.2
Time step Δt	$5\times10^{-4}\,\mathrm{s}$	$2.6\times10^{-4}\,\mathrm{s}$
Vortex shedding distance	$U\Delta t$	$U\Delta t$
Vortex core parameter c_{lo}	0.003	-
Initial vortex position $x_0/c, y_0/c$	$[-5, 0.1]$	$[-10, 0.1]$
Permeability distribution $h(x)$	$0.5+0.5\tanh(-4c+8x)$	$0.5+0.5\tanh(-4c+8x)$
Airfoil control points	100	100
Permeability parameter κ	5.4×10^{-3}	5.4×10^{-3}

Table A.1: Important near-field simulation parameters used in this work in comparison with the simulation setup of Weidenfeld and Manela [91].

agree with experiments on TBL-TE noise reduction through porous TEs. Results from the far-field calculations generally agreed with the ones from Weidenfeld and Manela [91]. However, numerical instabilities caused deviating acoustic pressures especially around the point of time when the convected vortex passed the TE. Further investigation into the setup of the numerical scheme and evaluation of the emitted acoustic power is required.

In the context of this thesis on activated porous materials for TBL-TE noise mitigation, the applicability of an analytical model which relates airfoil permeability and emitted noise was evaluated. A numerical scheme was implemented to solve for the near- and far-field characteristics of an airfoil subject to a convected vortex. A comparison with the results from Weidenfeld and Manela [91] was performed in order to validate correct implementation. Concerning the numerical scheme, it was found that the unsteady pressure calculation introduces instabilities if seepage velocities become too high. Furthermore, it was observed that simulation results were sensitive to vortex core modeling. The use of a continuous airfoil circulation distribution instead of a lumped vortex model could improve the robustness of the scheme.

The model which is based on potential flow and the theory of vortex sound is able to predict unsteady loads of partly permeable airfoils induced by convected vortices. With increasing airfoil permeability, the model indicates reduced loads, as expected from theory. For the prediction of TBL-TE noise emitted from airfoils with porous TEs, the applicability of the model has to be questioned. Apart from the simplifications of the airfoil geometry and flow field, the generation mechanism of TBL-TE noise is not well represented. Firstly, the analysis of Weidenfeld and Manela [91] is restricted to compact airfoils which means that the effects of edge scattering are not considered. Moreover, the focus lies on noise from unsteady airfoil loading due to an *incoming* vortex. This model setup represents vortex-airfoil interactions such as they occur for high-turbulence inflow. However, the aeroacoustic experiments in this work focused on edge noise due to turbulent boundary layer pressure fluctuations. The analytical model misses important aspects of TBL-TE noise generation such as the change of pressure fluctuation statistics over the length of the airfoil. It is concluded that the model of Weidenfeld and Manela [91] does not provide reliable predictions of TBL-TE noise reduction through porous TEs. However, it could be applied to study the effects of airfoil permeability on noise originating from blade-vortex interactions.